Spontaneous Symmetry-Breaking in Trilayer Graphene

Felix Winterer

München 2021

Spontaneous Symmetry-Breaking in Trilayer Graphene

Felix Winterer

Dissertation
an der Fakultät für Physik
der Ludwig-Maximilians-Universität
München

vorgelegt von
Felix Winterer
aus Freiburg im Breisgau

München, den 17.02.2021

Erstgutachter: Prof. Dr. Thomas Weitz
Zweitgutachter: Prof. Dr. Alexander Högele
Tag der mündlichen Prüfung: 19.04.2021

Zusammenfassung

Multilagen-Graphen besteht aus mehreren atomar dünnen Schichten von Kohlenstoffatomen und weist eine Vielzahl ungewöhnlicher elektrischer Eigenschaften auf. Unter anderem wurde vorhergesagt, dass abhängig von externen elektrischen und magnetischen Feldern und je nach Lagenfolge der einzelnen Kohlenstofflagen der Grundzustand des Systems in einen korrelierten Zustand übergehen kann, der spontan Symmetrien des Systems bricht. Diese Zustände sind aber typischerweise sehr instabil und können nur in hochreinen Proben mit homogener Lagenfolge sichtbar gemacht werden.

Im ersten Teil dieser Arbeit wurden die elektrischen Eigenschaften dieser korrelierten Zustände sowohl in Dreilagen-Graphen mit Bernal-Lagenfolge (ABA) als auch in Dreilagen-Graphen mit rhomboedrischer (ABC) Lagenfolgen genauer untersucht: In ABA Dreilagen-Graphen ist die Bandstruktur stark von externen elektrischen Feldern abhängig und bildet bei stärker werdenden Feldern mehrere zusätzliche Dirac-Kegel um den zentralen Dirac-Punkt der Bandstruktur aus. In dieser Arbeit wird gezeigt, dass mithilfe elektrischer und magnetischer Felder die Elektron-Elektron Wechselwirkung innerhalb der Dirac-Kegel verstärkt werden kann, bis der Grundzustand kontrolliert in einen korrelierten Zustand übergeht, der die Rotationssymmetrie des Systems spontan bricht. Anders verhält es sich in ABC Dreilagen-Graphen, dessen elektrische Struktur eine starke Berry-Krümmung und chirale Quasiteilchen aufweist. Als Folge davon wurde unter anderem vorhergesagt, dass bei verschwindender Ladungsträgerdichte mehrere spontane Quanten-Hall-Zustände auftreten können, die die chirale Symmetrie des Systems brechen. Messungen der Magnetotransporteigenschaften bei verschiedenen elektrischen und magnetischen Felder lassen ein vielfältiges Phasendiagramm der Quanten-Hall-Zustände erkennen, dass sogar Zustände mit intrinsischem orbitalem magnetischem Moment und Hall-Leitfähigkeit beinhaltet. Diese Erkenntnisse tragen zum tieferen Verständnis der korrelierten Zustände in Multilagen-Graphen und der Wechselwirkung von Ladungsträgern in zweidimensionalen Materialien bei.

Im zweiten Teil der Arbeit wird der Ladungstransport in anorganischen Halogenid-Perowskit Nanodrähten untersucht. Halogenid-Perowskit Materialien haben aufgrund ihrer außergewöhnlichen optoelektronischen Eigenschaften bereits vielfach Anwendung als Basismaterial für Solarzellen und Photodetektoren gefunden. In diesem Teil der Arbeit wird der Ladungstransport in Feldeffekt-Transistoren mit $CsPbBr_3$ Perowskit Nanodrähten in Abhängigkeit der Temperatur untersucht. Es wird gezeigt, dass ohne Beleuchtung der Probe der Ladungstransport

stark von tiefen Fallzuständen dominiert wird und bei niedrigen Temperaturen komplett ausfriert. Wenn die Probe jedoch beleuchtet wird, steigt die Mobilität der Ladungsträger stark an und wird bei niedrigen Temperaturen nur von der Phononenstreuung limitiert. Diese Ergebnisse unterstreichen die Defekt-Toleranz, die häufig mit Perowskit-Materialien in Verbindung gebracht wird und liefern neue Einsichten in die elektrischen Fallenzustände in $CsPbBr_3$ Perowskit-Nanodrähten.

Abstract

In recent years, multilayer graphene, a stack of several atomically thin layers of carbon atoms, has attracted growing interest due to its intriguing electronic properties and exceptional tunability. Depending on its stacking order, multilayer graphene has been predicted to be susceptible to a variety of correlated broken-symmetry ground states that can be accessed and explored upon appropriate tuning of its electronic structure via electrostatic gating and magnetic fields. However, in order to reveal these fragile states, excellent device quality and stacking order homogeneity are prerequisite.

In this thesis, magnetotransport in Bernal-stacked (ABA) trilayer graphene encapsulated in hexagonal boron nitride as well as suspended rhombohedral (ABC) trilayer graphene is investigated. Depending on the stacking order, two families of correlated states that spontaneously break symmetries of the system are observed. In ABA trilayer graphene, external electric fields strongly deform the band structure and lead to the emergence of multiple off-center Dirac points (Dirac gullies). It is demonstrated that electric and magnetic fields can be used as tuning parameters to enhance electron-electron interactions within these Dirac gullies. At appropriate tuning, magnetotransport maps indicate the emergence of a new correlated ground state that spontaneously breaks the rotational symmetry of the system. In contrast, ABC trilayer graphene hosts chiral quasi-particles that exhibit a non-zero Berry phase when encircling one of the valleys of its band structure. It has been shown, that ABC trilayer graphene is susceptible to spontaneous chiral symmetry breaking due to its flat band structure at charge neutrality. Indeed, transport measurements demonstrate the emergence of several spontaneous quantum Hall phases that are driven by a giant Berry curvature. Mapping magnetostransport as a function of electric and magnetic fields reveals a rich phase diagram including states with non-zero orbital momentum and Hall conductivity. The findings of this thesis provide novel insights into the world correlated phases in multilayer graphene and interaction physics in two dimensions.

In a second part of this thesis, charge transport in all-inorganic halide perovskite nanowires is investigated. In recent years, halide perovskites have emerged as promising novel materials for optoelectronic applications due to their large absorption coefficient and exceptional charge carrier lifetime. Yet, although the optical properties have been studied intensely, charge transport mechanisms and the influence of traps still remains elusive. In this thesis, temperature dependent charge transport in $CsPbBr_3$ nanowire field-effect transistors is investigated. It is shown, that charge

transport in the dark is dominated by deep traps and freezes out at low temperatures. However, illuminating the sample increases the mobility several orders of magnitude revealing even phonon-limited transport characteristics. These findings highlight and extend the notion of “defect-tolerance” of perovskite materials and provide novel insights into defect states in $CsPbBr_3$ nanowires.

Table of Contents

1 Introduction

For several decades, two-dimensional (2D) materials were widely believed to be non-existent in nature[1]. Although graphene, a single atomic layer of graphite, has already been theoretically studied for years[2,3], it came as a surprise when K. Novoselov and A. Geim were able to isolate it for the first time in their groundbreaking experiments in 2004[1,4]. Owing to its exceptional electronic and mechanical properties, graphene quickly sparked enormous interest in both fundamental physics and material science. In part, its great success was also due to the novel and surprisingly simple fabrication technique that enabled producing high-quality graphene with nothing more than an adhesive tape and a graphite source[5]. In this so-called mechanical exfoliation method, graphene flakes are obtained by peeling thin graphite fragments with an adhesive tape from a bulk crystal, thinning them down by repeated peeling and transferring them onto a suitable substrate[1]. Astonishingly, among thicker graphite clusters, also atomically thin graphene flakes can be found and visualized by simple optical microscopy[1]. Motivated by the isolation of graphene and adapting the mechanical exfoliation technique, a whole variety of 2D materials including superconductors[6,7], semiconductors[7] and ferromagnets[8,9] have been discovered since. In addition, versatile methods to transfer and stack individual 2D materials on top of each other allowing to engineer novel complex materials with hand-tailored properties have been developed[10,11].

Yet, graphene based systems have still remained highly relevant especially in fundamental research due to their unexcelled charge carrier mobility and excellent tunability[1,5]. This is especially true for multilayer graphene, a stack of several graphene layers, where layer number and stacking order provide additional tuning parameters[12–14]. For instance, multilayer graphene with rhombohedral (ABC) stacking order can host chiral quasi-particles with an arbitrarily flat power-law dispersion[14,15], while Bernal (ABA) stacked multilayer graphene hosts combinations of massless and massive fermions[14,16]. Together with the possibility to tune its electronic structure via electrostatic gating[17], multilayer graphene is a versatile platform to investigate quantum transport phenomena and many-body physics in two dimensions. In particular, multilayer graphene has been predicted to be susceptible to a wide range of novel correlated ground states that spontaneously break one or more of the systems symmetries[18–23].

In general, the description of electronic states in a solid-state system is a quantum many-body problem with a vast amount of degrees of freedom[24]. Most metallic systems, however, can be

described within Landau's Fermi-liquid theory that reduces the complex interacting electron system to an effective essemble of free quasi-particles[24,25]. Yet, when the interaction energy becomes dominant compared to the kinetic energy, this single-particle picture may break down and the Fermi-liquid ground state becomes unstable[24]. As a result, exotic interaction-driven ground states such as ferromagnetic phases or the fractional quantum Hall effect might emerge[24]. In multilayer graphene, several instabilities towards complex correlated states are present and can be explored experimentally. For instance, in rhombohedral multilayer graphene, the kinetic energy close to charge neutrality is quenched substantially due to the flat energy dispersion and interactions are expected to dominate[12,24]. Indeed, several correlated states have been postulated, including a superconducting phase[21,22] and a set of competing gapped quantum Hall states[18,19]. So far, experiments on bilayer and multilayer graphene confirm the presence of a spontaneous gap at charge neutrality[17,26–28], but both the order parameter of the ground state and phase diagram of correlated states still remain elusive. Alternatively, electron-electron interactions can be enhanced in the quantum Hall regime, as the formation of Landau levels likewise quenches the kinetic energy[24]. Here, ABA multilayers are especially suitable to explore correlated stats, since their peculiar band structure offers the unique possibility to additionally tune interaction via electric fields[20,29,30]. It has been predicted, that ABA multilayer graphene is susceptible to nematic states that spontaneously break rotational symmetry[20].

However, the observation of these fragile correlated states is challenging as excellent device quality and the absence of any domain walls are prerequisite[31]. At the same time, dual-gated structures that allow for tuning both charge carrier density and electric field independently are highly advantageous. Experimental efforts to isolate graphene from its environment and reducing the charge homogeneity have led to the development of two promising device architectures. In the first approach, graphene is suspended over the substrate by wet etching[17,32]. Although demonstrating excellent transport characteristics[32], the fragile device architecture strongly limits the accessible voltage range of electrostatic gates. In a second approach, following the idea of stacking 2D materials, graphene is encapsulated in hexagonal boron nitride (hBN)[33,34]. Since hBN has the same crystal structure as graphene with a comparable lattice constant, but is both inert and insulating, encapsulated graphene is extremely flat and essentially free of charge traps[33,35]. Compared to suspended devices, encapsulated samples substantially increase the accessible gate range at the cost of adding considerable screening of Coulomb interactions through the presence of hBN.

In this thesis, low-temperature transport measurements on high-quality suspended and encapsulated trilayer graphene devices with ABA and ABC stacking order are presented. In both device types, the emergence of correlated states that spontaneously break one or more symmetries of the system is demonstrated and their dependence on electric and magnetic field explored. Specifically, in ABC trilayer graphene, several competing spontaneous quantum Hall states emerge, some of which possess a non-zero charge Hall conductivity and orbital magnetic moment even in

the absence of magnetic fields. In ABA trilayer graphene, it is demonstrated that electron-electron interactions can be readily tuned via electric fields leading to the formation of correlated states that spontaneously break the rotational symmetry of the system. These results provide novel insights into the phase diagram of correlated states in multilayer graphene and into the world of interaction physics in two dimensions.

In the second part of the thesis, electrical transport in all-inorganic perovskite nanowires is investigated. All-inorganic halide perovskites are a new class of materials that offer excellent optoelectronic properties including strong optical absorption[36,37] and long charge carrier lifetime[38], while still being comparably cheap and easy to process[39]. In the last years, colloidal methods to efficiently fabricate all-inorganic halide perovskite nanowires have been developed[39–43], showing great promise for application as lasers and photodetectors[44–46]. However, so far, little is known about the transport mechanisms and charge traps inside all-inorganic perovskite materials. In this thesis, a field-effect transistor geometry is employed to investigate temperature-dependent charge transport properties of $CsPbBr_3$ nanowire films. It is shown, that in the absence of illumination, deep traps within the system dominate transport and the mobility freezes out at low temperatures. Surprisingly, when switching on the illumination, the mobility increases by several orders of magnitude and even phonon-limited transport characteristics are visible. These findings highlight the notion of "defect tolerance"[47–51] of perovskite materials and provide guidelines to improve device performance in the future.

The outline of the thesis is as follows: In chapter 2, the theoretical foundations of this thesis are presented. After introducing the basic electronic properties of multilayer graphene, the modifications to electronic states in both the quantum Hall regime and due to electron-electron interactions are discussed. In a last section, the underlying mechanisms and concepts of field-effect transistors and their characteristics are given. In chapter 3, the experimental methods to fabricate and characterize high-quality multilayer graphene devices are discussed. Furthermore, the different setups and techniques to access the electrical transport characteristics of graphene and perovskite devices are presented together with a brief overview of the measurement software developed within this thesis. In chapter 4, theoretical simulations as well as transport measurements on encapsulated multilayer graphene with ABA stacking order are shown. In chapter 5, transport data of suspended dual-gated ABC multilayer graphene devices demonstrating the emergence of several competing symmetry-broken quantum Hall states is presented. The temperature dependent transport measurements on perovskite nanowire films are discussed in chapter 6. Lastly, a short summary and an outlook on future research possibilities is given in chapter 7.

2 Theoretical Foundations

In this chapter, the fundamental concepts and theories that form the basis of this thesis are reviewed. First, a brief introduction to the field of 2D materials as well as their electronic structure is given. Since graphene plays a central role within this thesis, the electronic properties of both monolayer graphene and multilayer graphene are discussed in more detail. In the second section, the quantum Hall effect as one of the most fundamental quantum transport phenomena of two-dimensional electron systems is presented. In the third section, the influence of electron-electron interactions on electronic states and charge transport in graphene is reviewed. Lastly, the basic principles of field-effect transistors and their application for investigating graphene and perovskite samples are discussed.

2.1 Two-Dimensional Materials

In the last decades, 2D materials have emerged as a novel and fascinating class of materials. These materials consist of a single crystal layer only (thus the term "two-dimensional") and have been shown to exhibit unique physical properties due to their unusual dimensionality[1,5,10]. Starting from the first experimental isolation of graphene[4], a one-atom-thick layer of graphite, a whole variety of different 2D materials[6–9] have been discovered since. Within this thesis, two of the most important 2D materials are highlighted: few-layer graphene and hBN. On the one hand, graphene is a semi-metal material that, since its discovery in 2004[4], has consistently been on the forefront of the field of 2D materials. Its mechanical strength[52], exceptional electric conductivity[32,34] and unique electronic spectrum[1] make it a versatile material for a whole range of applications such as in flexible electronics or high-frequency transistors[5]. Combining several layers of graphene strongly increases the number of tuning parameters and makes multilayer graphene a promising system to investigate novel quantum transport properties[18,20]. On the other hand, hBN is an insulating isomorph of graphene that is relatively inert and free of surface charge traps[33]. Encapsulating graphene in hBN layers has proven to be an efficient way to create ultra-clean graphene devices with an excellent charge carrier mobility[33,34]. In general, hBN is broadly used to protect 2D material stacks from the environment while, at the same time, acting as a gate dielectric in a field-effect transistor geometry (see section 2.2.4). In the following, the atomic structure and electronic properties of monolayer graphene and multilayer graphene as well as hBN are discussed in more detail.

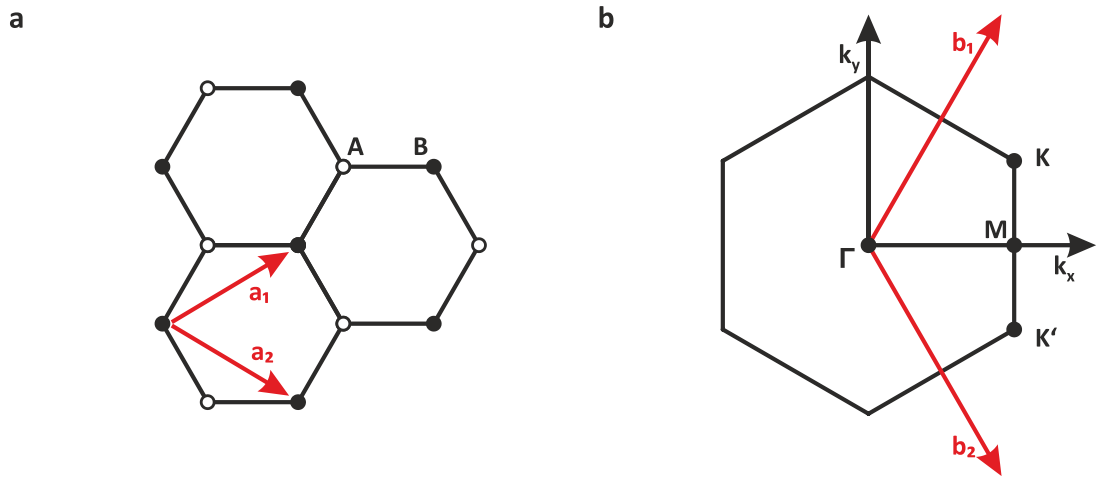

Figure 2.1 Lattice Structure of Graphene: *(a) The hexagonal lattice of graphene with two atoms per unit cell. The unit cell vectors are represented by a_1 and a_2. Atoms of sublattice A are shown in white and atoms of sublattice B in black. (b) The reciprocal lattice of graphene and the reciprocal lattice vectors b_1 and b_2 together with the position of the high-symmetry points K and K' points (and Γ, M).*

2.1.1 Monolayer Graphene

Monolayer graphene consists of a single layer of carbon atoms, that are arranged in a honeycomb lattice[1,53,54] (see Figure 2.1a). The planar structure of graphene is stemming from the sp^2 hybridization of one s and two p orbitals of the carbon atoms, which leads to a strong planar covalent σ-bond between nearest neighbor carbon atoms[53,54]. The remaining electrons occupy the p_z orbital perpendicular to the carbon plane and form π-bonds[53,54]. In general, the σ-bonds are responsible for the stability of graphene[52], whereas the π-bonds host a delocalized electron system giving rise to the characteristic electronic properties of graphene[53,54]. In order to calculate the band structure, it is worth noting, that the honeycomb lattice structure of graphene can also be seen as a triangular lattice with two atoms per unit cell[53,54]. Consequently, the Graphene lattice decomposes into two inequivalent sublattices A and B (see Figure 2.1a). The lattice vectors of graphene can be written as[53,54]

$$\boldsymbol{a}_1 = \frac{a}{2}(3, \sqrt{3}), \quad \boldsymbol{a}_2 = \frac{a}{2}(3, -\sqrt{3}) \tag{2.1}$$

where $a \approx 1.42$ Å is the carbon-carbon distance in the honeycomb lattice. The resulting Brillouin zone of the graphene lattice is shown in Figure 2.1b. The high-symmetry points K and K' are of particular importance for the band structure of graphene and correspond to the following positions

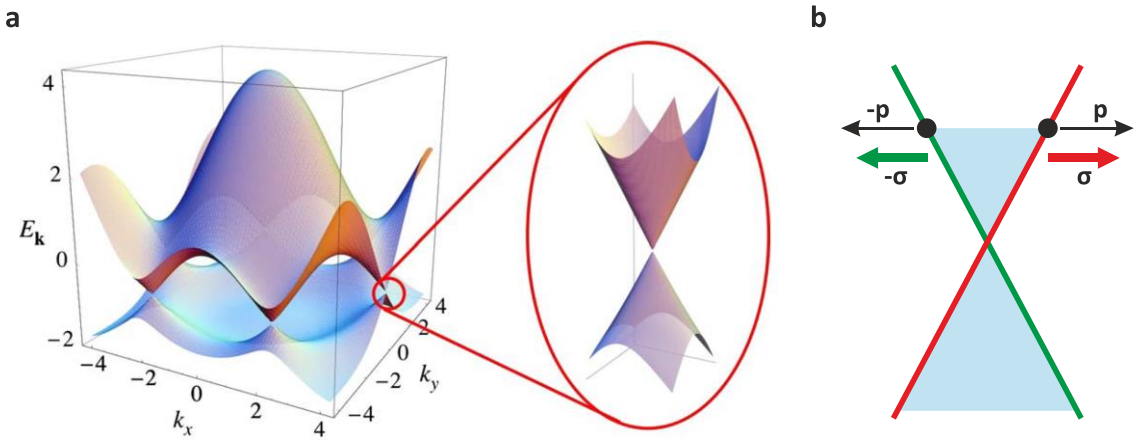

Figure 2.2 Band Structure of Graphene and Pseudo-Spin: *(a) Band structure of graphene as derived from the tight-binding model for γ_0 = 2.7 meV and γ_0' = 0.5 meV. The conduction and valence bands of graphene touch at the K and K' points forming linear low-energy bands (see zoom-in). Reprinted from Ref [53]. (b) Schematic representation of the linear band structure of graphene together with the pseudo-spin of quasi-particles in graphene. The black arrow indicates the direction of the quasi-particle momentum and the red (green) arrow the direction of the quasi-spin. All states along the red and green branch of the spectrum have the same pseudospin direction. The Fermi-level is indicated in blue. Adapted from Ref [57].*

in the reciprocal lattice[53,54]:

$$\boldsymbol{K} = \left(\frac{2\pi}{3a}, \frac{2\pi}{3\sqrt{3}a}\right), \quad \boldsymbol{K'} = \left(\frac{2\pi}{3a}, -\frac{2\pi}{3\sqrt{3}a}\right) \tag{2.2}$$

When taking both nearest-neighbor and next-nearest-neighbor hopping into account, the tight-binding Hamiltonian has the following form[2,53,54]

$$H = -\gamma_0 \sum_{\langle i,j\rangle,\sigma} \left(a_{\sigma,i}^{\dagger} b_{\sigma,j} + H.c.\right) - \gamma_0' \sum_{\langle i,j\rangle,\sigma} \left(a_{\sigma,i}^{\dagger} a_{\sigma,j} + b_{\sigma,i}^{\dagger} b_{\sigma,j} + H.c.\right), \tag{2.3}$$

where $a_{\sigma,i}$ ($a_{\sigma,i}^{\dagger}$) annihilates (creates) an electron with spin $\sigma = \uparrow, \downarrow$ on site r_i on sublattice A (an equivalent definition is used for sublattice B). Furthermore, γ_0 describes the nearest-neighbor hopping energy and γ_0' the next-nearest-neighbor hopping energy. The energy bands that results from this Hamiltonian have to form[2,53,54]

$$E_{\pm}(\boldsymbol{k}) = \pm\gamma_0\sqrt{3 + f(\boldsymbol{k})} - \gamma_0' f(\boldsymbol{k}), \tag{2.4}$$

with

$$f(\boldsymbol{k}) = 2\cos\left(\sqrt{3}k_{\mathrm{y}}\mathrm{a}\right) + 4\cos\left(\frac{\sqrt{3}}{2}k_{\mathrm{y}}\mathrm{a}\right)\cos\left(\frac{3}{2}k_{\mathrm{x}}\mathrm{a}\right). \tag{2.5}$$

Here, $\pm$ refers to the conduction and valence band respectively. When next-nearest neighbor hopping is present and $\gamma_0' \neq 0$, the electron-hole symmetry is broken. The band structure of graphene for non-zero γ_0' is shown in Figure 2.2a. Notably, the band structure is gapless with valence and conduction bands touching at the K and K' points (cf. Figure 2.1a and Equation (2.2))[53,54]. The low energy regime in the vicinity of these points hosts most of the peculiar physics of graphene[1,53,54]. Expanding the Hamiltonian in equation (2.3) up to first order for small wave numbers $\boldsymbol{q}$ around the K point yields[53–55]

$$H_K = v_{\mathrm{F}}\begin{pmatrix} 0 & \hbar(q_x - iq_y) \\ \hbar(q_x + iq_y) & 0 \end{pmatrix} \tag{2.6}$$

with the Fermi velocity $v_{\mathrm{F}} = 3a\gamma_0/2$. The Hamiltonian describing particles close to the K' can be derived in a similar way yielding $H_{K'} = H_K^T$. Note, that in the low-energy regime, the electronic states are composed of two components belonging to the two different sublattices of graphene. This has been accounted for by using a two-component wave function with one component for sublattice A and one component for sublattice B[1,18,19,53,54,56,57]. The energy eigenvalues of this Hamiltonian give rise to conical bands with a linear dispersion[53–55]

$$E_{\pm}(\boldsymbol{q}) \approx \pm v_{\mathrm{F}}\hbar q, \tag{2.7}$$

with ± referring to the conduction and valence band respectively. The low energy bands are shown in the zoom-in in Figure 2.2a. Rewriting this Hamiltonian by using a vector of Pauli matrices $\boldsymbol{\sigma} = (\sigma_x, \sigma_y)$ with

$$\sigma_x = \begin{pmatrix} 0 & 1 \\ 1 & 0 \end{pmatrix}, \quad \sigma_y = \begin{pmatrix} 0 & -i \\ i & 0 \end{pmatrix}, \quad \sigma_z = \begin{pmatrix} 1 & 0 \\ 0 & -1 \end{pmatrix} \tag{2.8}$$

and the quasi-momentum $\boldsymbol{p} = \hbar\boldsymbol{q}$, gives[53–55]

$$H_K = v_{\mathrm{F}}\boldsymbol{\sigma}\cdot\boldsymbol{p} = -i\hbar v_{\mathrm{F}}\boldsymbol{\sigma}\cdot\nabla. \tag{2.9}$$

Thus, quasi-particles in graphene are described by a massless Dirac-like Hamiltonian[58] with the speed of light being replaced by the Fermi velocity $v_{\mathrm{F}} \approx 10^6$ m s^{-1}. Due to this analogy, the K and K' points are often called *Dirac points*[1]. The eigenfunctions in momentum space corresponding to this

low-energy Hamiltonian are given by[54]

$$\psi_{\pm}^{K} = \frac{1}{\sqrt{2}}\begin{pmatrix} e^{-i\phi/2} \\ \pm e^{i\phi/2} \end{pmatrix} \qquad \psi_{\pm}^{K'} = \frac{1}{\sqrt{2}}\begin{pmatrix} e^{i\phi/2} \\ \pm e^{-i\phi/2} \end{pmatrix}, \tag{2.10}$$

where ϕ refers to the polar angle of the quasi-momentum with $\boldsymbol{p} = p(\cos\phi, \sin\phi)$ and ± again refers to the conduction and valence band respectively. At this point, it is worth pointing out various important properties of the Hamiltonian and the wave functions:

Pseudo-Spin: As mentioned earlier, the wave functions have two components corresponding to the two sublattices of graphene. In fact, the wave function can be seen as two-component spinors where the sublattice index (referring to sublattice A and B) plays the role of a spin[1,18,19,56,57]. In this analogy, "spin up" refers to finding a quasi-particle in sublattice A, while "spin down" refers to finding a quasi-particle in sublattice B. In the following, this property of the wave function will be referred to as *pseudo-spin*[1,53,54].

Valleys: In graphene, the low-energy spectrum has two inequivalent points of particular importance, namely the K and K' points[1,53,54]. As shown before, quasi-particles close to these two *valleys* can be described by two different Hamiltonians and wave functions[53,54]. However, the wave functions at these two valleys are closely related via time-reversal symmetry[53,54]. Thus, quasi-particles in graphene possess an additional degree-of-freedom, often referred to as valley degree-of-freedom.

Chirality: In contrast to typical solid-state systems, electron and hole states in graphene are deeply interconnected[1,57]. For every electron with energy E propagating in one direction, there is also a hole state with energy $-E$ propagating in the opposite direction[1,18,57]. This is a direct consequence of the close link between the pseudo-spin direction and the direction of the quasi-momentum: The pseudo-spin of an electron is always parallel, while the pseudo-spin of a hole is always antiparallel to the momentum[1,53,57]. This is also indicated in Figure 2.2b, where quasi-particles on different branches of the b. This symmetry is often referred to as chiral symmetry and quasi-particles obeying this symmetry are called *chiral*[1,53,57].

Berry Phase: When going along a circular path in momentum space around the K or K' point rotating ϕ by 2π, the wave function changes sign indicating a phase change of π (cf. equation (2.10))[53,54]. This is very characteristic of spinor wave functions and is often referred to as the *Berry phase*[59,60]. In general, the Berry phase is the phase a wave function picks up when going along a closed loop in parameter space[59,61]. The Berry phase can also be written as the integral of a field (often called the Berry curvature) over the surface contained in the closed loop[61]. Intuitively speaking, the Berry curvature can be seen as a built-in magnetic field and the Berry phase as the phase a particle would acquire when going around a loop enclosing a magnetic flux[61]. It is worth emphasizing, that the Berry curvature is an intrinsic property of the band structure and significantly alters the motion of electrons in a crystal[61]. For instance, this becomes relevant, when the system is subject to an

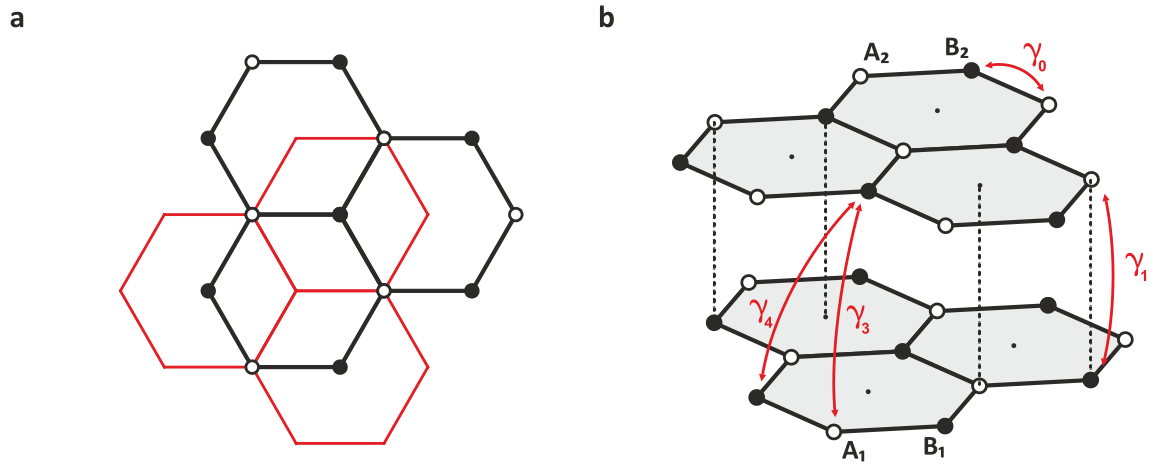

Figure 2.3 Lattice Structure of Bilayer Graphene: *(a) Relative position of the two graphene lattices of bilayer graphene. (b) Relative position of the two graphene lattices of bilayer graphene from a side view. Atoms in sublattices A_i and B_i with i = {1,2} being the layer index are indicated in white and black respectively. Red arrows indicate the hopping parameters γ_i.*

external perpendicular magnetic field. Under the influence of the external field, electrons will start to move in cyclotron orbits and thus acquire a Berry phase[1,56,62]. As a results, the characteristics of the quantum Hall effect in graphene will be different compared to electron systems without a Berry phase[1,56,62]. This will be discussed in more detail in the section 2.2.

2.1.2 Bilayer Graphene

Bilayer graphene consists of two individual layers of graphene that are stacked on top of each other[53,54]. In the most energetically stable stacking configuration, the two layers are shifted with respect to each other such that one atom of the top layer sits directly above the center of the honeycomb of the bottom layer (see Figure 2.3a,b)[53,54]. This stacking configuration is often called AB stacking, referring to the different positions of the individual layers[55]. When deriving the tight-binding model of bilayer graphene, not only intralayer, but also interlayer hopping parameters have to be taken into account. The definitions of the lowest order hopping parameters, adopting the nomenclature from the Slonczewski-Weiss-McClure model for graphite[63–65], are shown in Figure 2.3b. The most important hopping parameters are the intralayer coupling $\gamma_0 \approx 3.2$ eV[63] analogous to the monolayer case, and the nearest neighbor inter-layer coupling $\gamma_1 \approx 0.39$ eV[63] between atoms of sublattice B_1 and A_2 that sit directly on top of each other (cf. Figure 2.3). The next-nearest neighbor inter-layer couplings γ_3 and γ_4 connect sublattices of the different species (e.g. A_1 to B_2) and same species (e.g A_1 to A_2) respectively[53–55]. As in graphene, the electronic properties at low energies are well-captured by taking only nearest neighbor couplings into account[14,54]. Thus, γ_3 and γ_4 will be neglected for now, but reintroduced later. First, bilayer graphene has the same symmetry

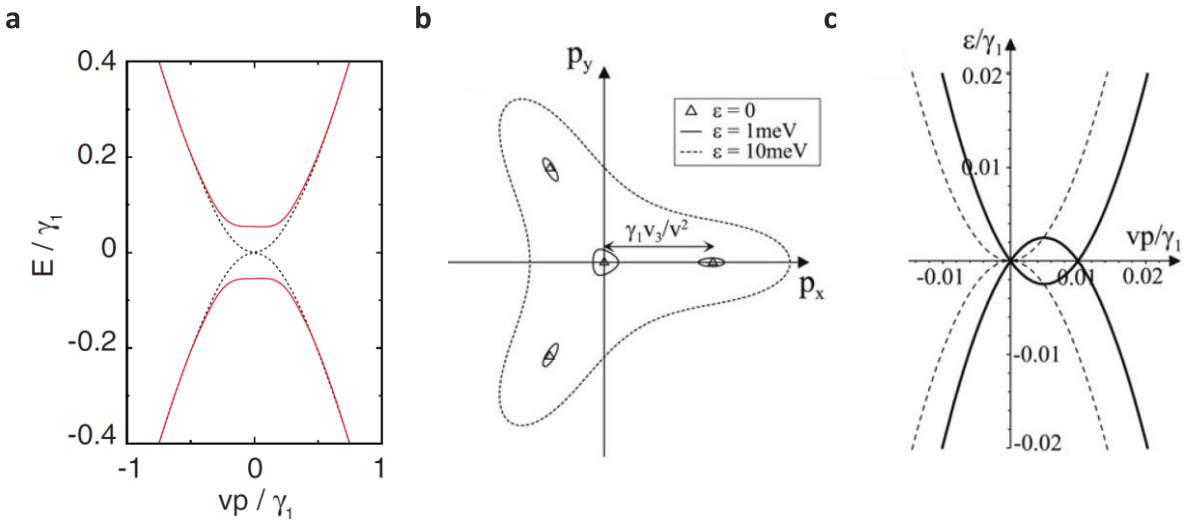

Figure 2.4 Band Structure of Bilayer Graphene: *(a) Low energy band structure of bilayer graphene at the K point taking only nearest neighbor hopping into account. The band structure at zero electric field is shown as a dotted line. The band opening at a non-zero electric field is shown in red. Reprinted from Ref [14]. (b,c) Trigonal warped Fermi-surfaces at various energies at the K point. The trigonal warping term γ_3 splits the single band touching point into one center and three off-center band touching points. Reprinted from Ref [66].*

as monolayer graphene (cf. Figure 2.1b)[53,54]. The wave functions describing bilayer quasi-particles, however, consist not only of two but four components, one for each of the sublattices A_i and B_i with layer index $i = \{1,2\}$[53,54]. In the low-energy approximation, this can be further simplified by noting, that the interlayer coupling γ_1 essentially dimerizes the sublattices B_1 and A_2 and substantially shifts their energy bands by $\pm\gamma_1$ away from the Fermi energy[54,55]. Dropping these high energy states, the Hamiltonian for small momentum $\boldsymbol{q}$ around the K point reads[1,54,56]

$$H_K = \frac{\hbar^2}{2m}\begin{pmatrix} 0 & (q_x - iq_y)^2 \\ (q_x + iq_y)^2 & 0 \end{pmatrix}, \tag{2.11}$$

where the effective mass m is given by $m = \gamma_1/(2v_F^2)$. Again, a similar Hamiltonian can be derived for the K' point. The eigenvalues of this Hamiltonian give rise to quadratic bands[53,54]

$$E_\pm(\boldsymbol{q}) = \pm\frac{\hbar^2 q^2}{2m} = \pm\frac{p^2}{2m}, \tag{2.12}$$

with the quasi-momentum $\boldsymbol{p} = \hbar\boldsymbol{q}$ and ± referring to the conduction and valence band respectively. Figure 2.4a shows the low-energy band structure of bilayer graphene. Again, similar to monolayer graphene, bilayer graphene has no bandgap and the conduction and valence band touch at the K

and K' points. The corresponding eigenfunctions of the Hamiltonian are given by

$$\psi_{\pm}^{K} = \frac{1}{\sqrt{2}}\begin{pmatrix} e^{-i\phi} \\ \pm e^{i\phi} \end{pmatrix} \tag{2.13}$$

Again, ϕ refers to the polar angle of the quasi-momentum with $\boldsymbol{p} = p(\cos\phi\,, \sin\phi)$ and ± refers to the conduction and valence band respectively. Comparing these results to the monolayer case yields some close similarities. Quasi-particles in bilayer graphene also have a pseudo-spin. However, in contrast to monolayer graphene, the pseudo-spin refers to sublattices A_1 and B_2 on the bottom and top layer respectively[53,54]. Likewise, quasi-particles in bilayer graphene are chiral[1,53–56]. To emphasize this analogy, it is worth rewriting the Hamiltonian similar to the monolayer case as follows[18,55,56]

$$H_K = \frac{\hbar^2}{2m}\begin{pmatrix} 0 & (p_x - ip_y)^2 \\ (p_x + ip_y)^2 & 0 \end{pmatrix} = \frac{\hbar^2 p^2}{2m}\boldsymbol{\sigma}\cdot\boldsymbol{n}(\phi) \tag{2.14}$$

where $\boldsymbol{n} = (\cos 2\phi\,, \sin 2\phi)$ and $\boldsymbol{\sigma} = (\sigma_x, \sigma_y)$ is a vector of Pauli matrices (cf. equation (2.10)). In the context of bilayer graphene, chirality means that the pseudo-spin of the bilayer wave function is always parallel (antiparallel) to the axis $\boldsymbol{n}$ for electrons (holes)[55,56]. When going along a closed path around the K point, the wave function of bilayer graphene acquires a Berry phase of 2π[55,56]. Although this phase is indistinguishable from zero, it does, nevertheless, influence the quantum Hall effect in bilayer graphene significantly[1,55,56]. Note, that the Hamiltonian and the wave functions corresponding to the K' point have not be shown explicitly, but are related by time reversal symmetry to the Hamiltonian and wave functions at the K point[53,55]. Notably, quasiparticles at the K' point acquire a Berry phase of -2π[55].

Despite these similarities between the low-energy Hamiltonian of monolayer and bilayer graphene, there is also a crucial difference between them. As the wave function of bilayer graphene has components associated with different layers, one can break inversion symmetry (and likewise chiral symmetry) explicitly by applying an electric field. This introduces a potential difference between states on the top and bottom layer and a band gap between conduction and valence band opens. In a low-energy approximation, the modified Hamiltonian using the notation from equation (2.14). reads[14]

$$H = \frac{p^2}{2m}\boldsymbol{\sigma}\cdot\boldsymbol{n} + \frac{\Delta}{2}\sigma_z = \frac{p^2}{2m}\left[\cos(2\phi)\,\sigma_x + \sin(2\phi)\,\sigma_y\right] + \frac{\Delta}{2}\sigma_z \tag{2.15}$$

where Δ is the potential difference between bottom and top layer and the σ_i the Pauli matrices (cf.

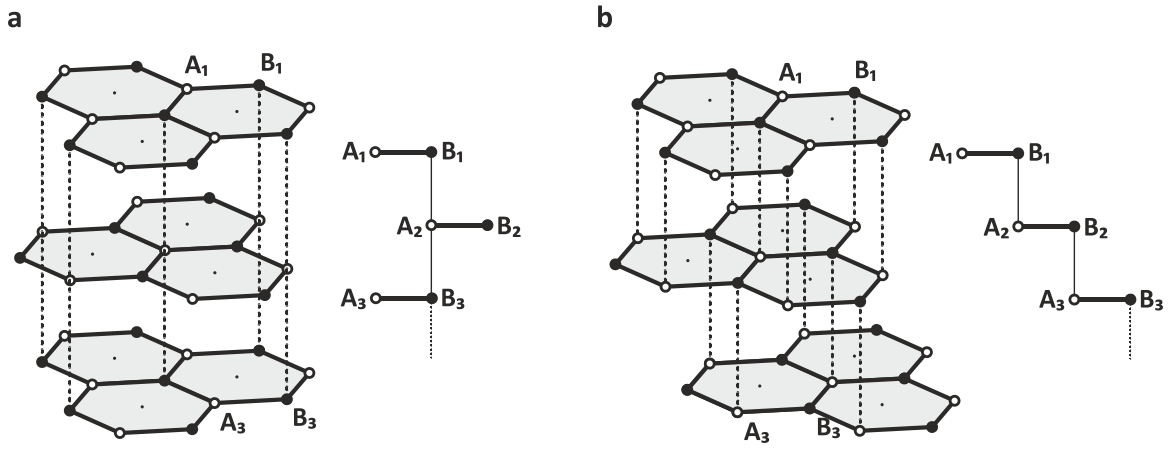

Figure 2.5 Stacking order of Multilayer Graphene: *(a) Position of atoms in the Bernal (ABA) stacking configuration. Atoms of sublattice B_1 sit directly above atoms of sublattice A_2 and B_3. (b) Position of atoms in the rhombohedral (ABC) stacking configuration. Atoms of sublattice B_i sit directly above atoms of sublattice A_{i+1}.*

equation (2.8)). The eigenenergies of this Hamiltonian are then given by

$$E_{\pm}(\boldsymbol{p}) = \pm\sqrt{(p^2/2m)^2 + (\Delta/2)^2} \tag{2.16}$$

where ± refers to the conduction and valence band respectively. The resulting band structure is shown in Figure 2.4a. At this point, it is worth coming back to the higher order hopping parameters γ_3 and γ_4. Reintroducing higher order hopping parameters into the Hamiltonian leads to structural modifications to the band structure[55,66]. The hopping parameter γ_3 ≈ 0.32 eV[63] introduces an energy term proportional to $\cos 3\phi$[66]. This leads to so-called trigonal warping that deforms the Fermi-surface at the K and K' points into a "triangular" shape (see Figure 2.4b,c)[15,55,63,66]. The coupling γ_4 ≈ 0.04 eV[63] is much weaker, but introduces a asymmetry between conduction and valence bands (not shown in Figure 2.4)[63].

2.1.3 Multilayer Graphene

The term multilayer graphene comprises all graphene stacks with more than two layers. Similar to bilayer graphene, consecutive layers in multilayer graphene are stacked in such a way, that one atom of the first plane sits directly above the center of the honeycomb of the second layer[14,53,67]. Although other configurations are possible due to the weak inter-lattice van-der-Waal forces, this is the most common stacking type in nature[14,53,67]. In bilayer, as discussed before, only one natural stacking order is available[53]. When adding a third layer, however, there are two possible stacking configurations of the third layer available: On the one hand, the atoms of the third layer can sit

directly above the atoms of the first layer[14,53,67]. This stacking order is called *Bernal* stacking or *ABA* stacking, where the notation ABA refers the fact, that the first and third layer are at the same position[14,53,67]. In the second configuration, the third layer sits in a position that is different from both the first and second layer[14,53,67]. This configuration is often referred to as *rhombohedral* stacking or *ABC* stacking[14,53,67]. Figure 2.5 shows an illustration of the two stacking orders. It is also worth noting, that there are no other inequivalent positions a new layer can be placed in[53]. When increasing the number of layers, the natural continuation of these sequences are ABABAB for Bernal and ABCABC for rhombohedral stacking[14,53]. In nature, Bernal stacking is the most thermodynamically stable stacking order with only some fraction of natural graphite having the rhombohedral stacking order[3,14,53]. Besides, also other mixed stacking orders (e.g. ABCBA) are possible[53,67], but are not be discussed within the scope of this thesis.

The band structure of multilayer graphene is significantly more complex than the band structure of mono- and bilayer graphene and depends both on the layer number and the stacking order[3,14,53,67,68]. On the one hand, ABC multilayer graphene can be seen as an extension to monolayer and bilayer graphene inheriting many of their properties[18]. The low-energy states live on the two outermost layers and will host chiral quasiparticles with a Berry phase $N\pi$ with N being the layer number[14,15,18]. As in bilayer, a non-zero external electric field opens up a band gap between valence and conduction band[14,62]. On the other hand, ABA multilayer graphene behaves like a superposition of individual bilayer bands (together with an extra monolayer band for odd layer numbers)[16,69–71]. An external electric field does not open a band gap, instead the potential asymmetry causes band overlapping[14]. The band structure of both ABC and ABA multilayer graphene will be discussed in more detail in the following.

ABC Stacking Order

As mentioned before, ABC multilayer graphene is the natural extension to monolayer and bilayer graphene. The derivation of the low-energy band structure of ABC multilayer graphene closely resembles the bilayer case and generalizes the approach to variable layer number N. The wave functions describing quasi-particles in ABC multilayer graphene have $2N$ components, one component for each layer and sublattice A_i and B_i[14]. However, similar to bilayer graphene, the inter-layer coupling γ_1 dimerizes neighboring sublattice sites B_i and A_{i+1} (see Figure 2.5a,b) and drives them away from the Fermi energy[15,64,72,73]. As a result, in a low-energy approximation neglecting all higher order hopping parameters, the wave function reduces to two components (referred to as pseudo-spin[18,56,62]) associated with the remaining outermost surface sublattice sites A_1 and B_N[14,72,74] while all bulk states are gapped out with an energy gap of approximately $3\pi\gamma_1/N$[74]. Thus, the low-energy electronic states of ABC multilayer graphene are well localized on the surface layers[14,72,74].

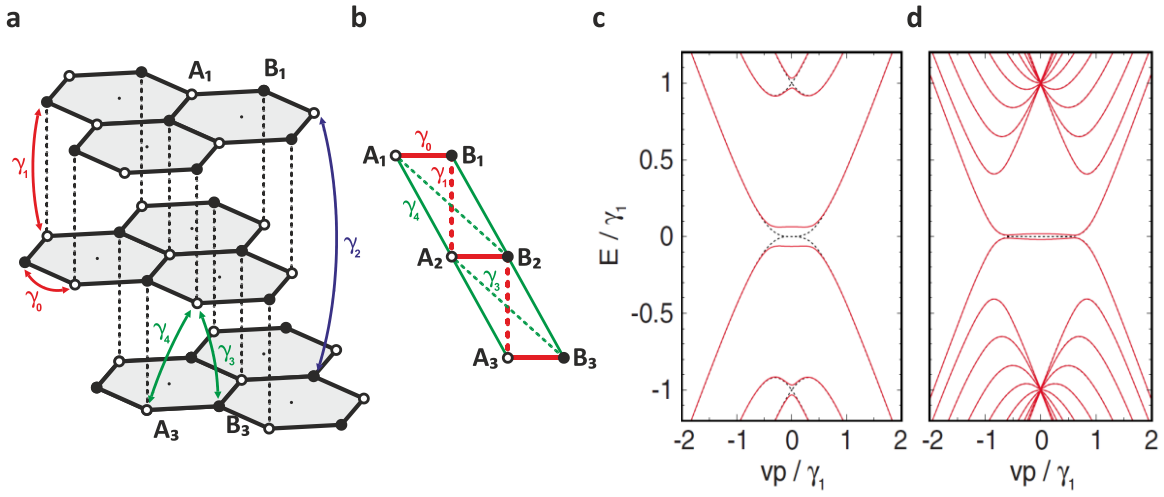

Figure 2.6 Hopping Parameters and Band Structure of ABC Multilayer Graphene: *(a,b) Illustration of the position of atoms as well as the hopping parameters γ_i of ABC multilayer graphene. (c,d) Band structure of ABC multilayer graphene for layer numbers N = 3 (c) and N = 10 (d) in the vicinity of the K and K' points with (red) and without (black) perpendicular external electric field. With increasing layer number, the low-energy bands become more flat and the bulk states advance closer to zero energy. Increasing the electric field opens a bandgap in the low-energy bands. Reprinted from Ref [14].*

Expanding the Hamiltonian for small momenta $\boldsymbol{p} = p(\cos\phi, \sin\phi)$ around the K point yields[14,18]

$$H_K = \frac{(v_\mathrm{F})^N}{(\gamma_1)^{N-1}} \begin{pmatrix} 0 & (p_x - ip_y)^N \\ (p_x + ip_y)^N & 0 \end{pmatrix} = \frac{(v_\mathrm{F}p)^N}{(\gamma_1)^{N-1}} \boldsymbol{\sigma} \cdot \boldsymbol{n}(\phi). \tag{2.17}$$

Where $\boldsymbol{n} = (\cos N\phi, \sin N\phi)$ and $\boldsymbol{\sigma} = (\sigma_x, \sigma_y)$ is a vector composed of Pauli matrices (cf. equation (2.8)) acting on the two-component spinor wave functions. Notably, this Hamiltonian also reproduces the Hamiltonians of monolayer (N = 1) and bilayer (N = 2) graphene, highlighting the close connection between them. Quasi-particles governed by a Hamiltonian of this general form are called chiral with a chirality equal to the layer number N[15,18,19,62,75]. In this context, chirality means that the pseudo-spin of the wave functions is always parallel (antiparallel) to the axis $\boldsymbol{n}$ for electrons (holes)[55,56]. It can be shown that quasi-particles with chirality N acquire a Berry phase of $\pm N\pi$ when going along a closed path around the K or K' point respectively[15,18,26,56,72,75]. The energy eigenvalues of the Hamiltonian in equation (2.17) are given by

$$E_\pm(\boldsymbol{p}) = \pm \frac{(v_\mathrm{F})^N}{(\gamma_1)^{N-1}} p^N \tag{2.18}$$

where ± refers to the conduction and valence band respectively[14]. Thus, the low-energy bands

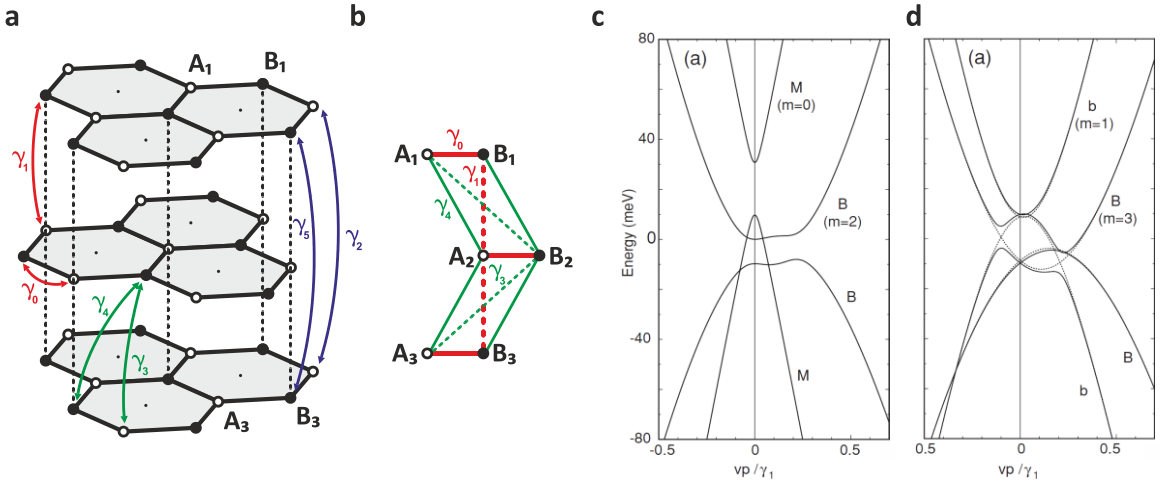

Figure 2.7 Hopping Parameters and Band Structure of ABA Multilayer Graphene: *(a,b) Illustration of the position of atoms as well as the hopping parameters γ_i of ABA multilayer graphene. (c,d) Band structure of ABA multilayer graphene for layer numbers N = 3 (c) and N = 4 (d) in the vicinity of the K and K' points. For trilayer graphene (c), the band structure originates from a superposition of a monolayer (M) and bilayer (B) band. For tetralayer graphene (d), the band structure consists of two bilayer bands (b and B). Reprinted from Ref [16].*

become more and more flat with increasing layer number N[12,15,26,72,76–78]. Figure 2.6c,d shows the band structure for two different layer numbers illustrating the increase in flatness of the dispersion. As a consequence, the density of states at charge neutrality diverges with $E^{(2-N)/N}$ for layer numbers $N > 2$[62,75,78]. This is in contrast to monolayer (N = 1) and bilayer (N = 2) graphene, where the density of state vanishes and remains finite at charge neutrality respectively. However, like in bilayer graphene, chiral symmetry can also be explicitly broken by applying an electric field[16,62]. Since the wave function is localized on the top and bottom layers, an electric field introduces a potential difference Δ and opens a band gap[16,62]. The resulting Hamiltonian then reads[16]

$$H = \frac{(v_F p)^N}{(\gamma_1)^{N-1}}\left[\cos(N\phi)\,\sigma_x + \sin(N\phi)\,\sigma_y\right] + \frac{\Delta}{2}\sigma_z \tag{2.19}$$

with energy eigenvalues[16]

$$E_{\pm}(\boldsymbol{p}) = \pm\sqrt{\frac{(v_F p)^{2N}}{(\gamma_1)^{2N-2}} + \left(\frac{\Delta}{2}\right)^2} \tag{2.20}$$

where ± refers to the conduction and valence band respectively. Other than that, the chiral symmetry is very robust with respect to higher order hopping contributions that add further terms in σ_x and σ_y to the Hamiltonian[18,62]. For example, the trigonal warping term γ_3 (see also section

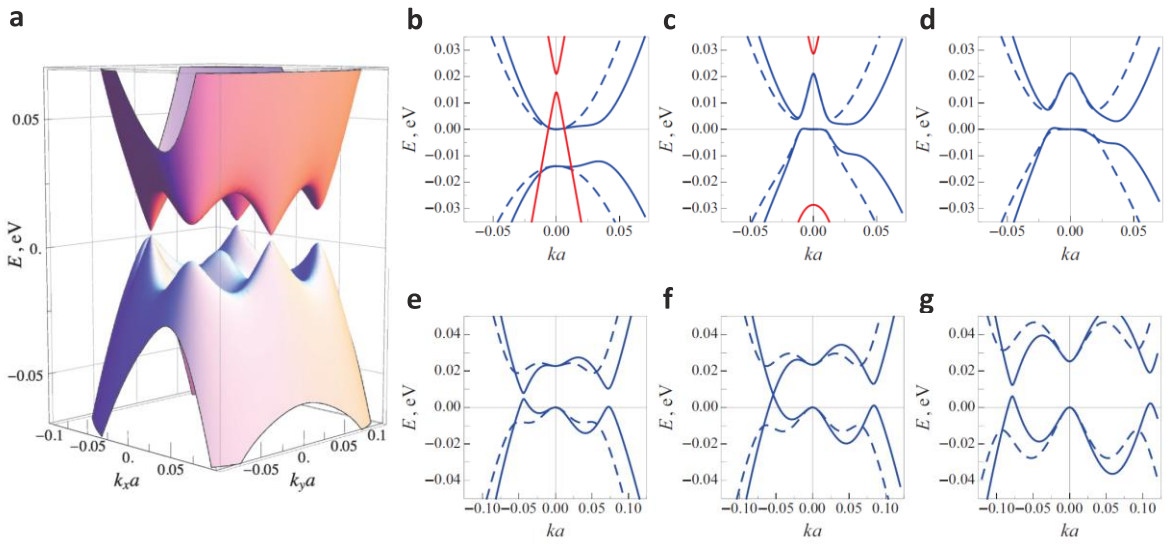

Figure 2.8 Band Structure of ABA Multilayer Graphene in an External Electric Field: *(a) Three-dimensional illustration of the position of the six Dirac gullies together with the central Dirac point for Δ_1 = 0.2 eV. (b-g) Evolution of the band structure of trilayer graphene in the vicinity of the K_+ point with increasing potential difference Δ_1 = 0.0 eV (b), 0.025 eV (c), 0.05 eV (d), 0.15 eV (e), 0.18 eV (f) and 0.25 eV (g). Solid (dashed) lines correspond to k parallel to the x-axis (y-axis). Blue and red lines correspond the to bilayer and monolayer band respectively. Reprinted from Ref [29].*

2.1.2 and Figure 2.4) deforms the band structure and leads to the formation of additional off-center band touching points depending on the number of layers[15]. In this case, the Berry phase is distributed over the off-center Dirac points while keeping the total Berry phase of $\pm N\pi$ unchanged[15].

ABA Stacking Order

In contrast to the ABC stacking order, the atomic structure of ABA multilayer graphene does not give rise to a γ_1 dimer chain that gaps out all bulk states. Instead, in a first approximation, the band structure can be decomposed into a superposition of bilayer bands for even layer numbers and a superposition of bilayer bands and a single monolayer band for odd layer numbers[14,16,53,67,70,79]. Due to this monolayer band, the electrical properties of multilayer graphene with even and odd layer number are distinctly different. In fact, multilayer graphene of arbitrary stacking order can be decomposed into such as a superposition of chiral building blocks[80]. It is also worth noting, that even layer numbers exhibit inversion symmetry, but odd layer numbers are only mirror-symmetric with respect to the central layer[16]. This first approximation can be refined by introducing higher order hopping terms leading to the Slonczewski-Weiss-McClure model of graphite[16,20,29,30,63–65]. Here, not only the intralayer coupling γ_0 and next-layer couplings γ_1, γ_3 and γ_4 as discussed in the bilayer case are taken into account (see section 2.1.2), but also next-nearest layer couplings γ_2 and

γ_5[16,20,29,30,53,63–65]. The definition of these coupling parameters is illustrated in Figure 2.7a. In addition, an energy difference δ between lattice sites involved in the γ_1 couling and sites not involved is introduced[30,53,63]. The band structure of trilayer and four-layer graphene in the absence of an external field is shown in Figure 2.7c,d. Although the band structure takes into account higher order terms, the monolayer-like and bilayer-like bands are nevertheless clearly discernable. When applying an external perpendicular electric field, the monolayer-like and bilayer-like bands start to hybridize[20,29,30]. Like in ABC multilayer graphene, an external electric field introduces a potential difference Δ_1 between the top and bottom layer of the graphene multilayer. However, the potential difference opens a negligible band gap in the range of a few meV only[20,29,30]. More prominently, the interplay between Δ_1 and the trigonal warping term γ_3 leads to a strong deformation of the band structure and the emergence of a new set of six additional pronounced Dirac points ("Dirac gullies") in the vicinity of each K point[20,29]. These six gullies can be divided into two sets of three gullies interconnected by C_3 rotation symmetry[20,29]. Figure 2.8a shows the band structure in the vicinity of the K point at finite potential difference Δ_1. The evolution of the band structure with increasing potential difference Δ_1 is shown exemplarly for trilayer graphene in Figure 2.8b-g. With increasing Δ_1, the monolayer-like bands start to shift to higher (lower) energies for electrons (holes)[29]. At the same time, the Dirac gullies become more and more prominent and shift to higher momenta[20,29]. This splitting of the band structure into Dirac gullies has further important consequences. If Δ_1 is fixed at a non-zero value, sweeping the chemical potential μ can lead to discontinuous changes of the Fermi surface topology[20], a so-called Lifshitz transition[20,81]. Such Lifshitz transitions are accompanied by a van Hove singularity with a logarithmically diverging density of states[20].

2.1.4 Hexagonal Boron Nitride

In order to reveal the intrinsic electronic properties of graphene, an inert environment free of charge impurities is prerequisite. The commonly used SiO_2 substrates for graphene, however, are known to have a substantial amount of surface traps and charge impurities that leads to unwanted charge disorder and doping in the graphene flake[33]. One strategy to prepare graphene samples with ultra-low charge disorder is suspending them over the SiO_2 substrate[32]. As a result, when using ultra-high vacuum, the influence of the environment on graphene can be minimized[32]. This technique, however, also suffers from some disadvantages. For example, the electric fields and charge carrier densities achievable in such a geometry are very limited due to the fragile nature of the suspended structure[33]. Another approach is to use hexagonal boron nitride as a substrate dielectric. Hexagonal boron nitride (hBN) is an insulating two-dimensional material that has the same hexagonal lattice structure as graphene[33,35]. In the hBN lattice, however, boron atoms occupy the sublattice A while nitrogen atoms occupy the sublattice B[33,35]. Since boron and nitrogen have different on-site energies, the band gap is very large (Δ = 5.97 eV) and hBN is essentially an insulator[33,35]. At the same time, the lattice mismatch with graphene is only 1.7 %[33,35]. Due to the strong ionic in-plane bonds,

hBN is also expected to be inert and free of dangling bonds or surface charge traps[33,35]. It has been shown, that graphene devices on hBN show an orders of magnitude higher mobility than on conventional SiO_2 substrates[33]. Furthermore, charge disorder in graphene was shown to be significantly lower when using hBN as a substrate[35,82]. Completely encapsulating graphene in hBN layers yields even higher mobilities close to what has been achieved in suspended samples[34].

2.1.5 Graphite

When increasing the layer number of multilayer graphene, the band structure starts to lose its two-dimensional characteristic and becomes bulk-like[83,84]. In the infinite-layer limit, graphite is a semi-metal with a small band overlap[63]. For example, for ABA multilayer graphene the transition to graphite-like behavior occurs approximately at layer numbers of $N \approx 10$ according the theoretical studies[84]. In multilayer ABC, the energy gap of bulk states becomes smaller when increasing N, until transport is essentially three-dimensional[83]. However, signatures of two-dimensional surface states (see section 2.1.3) have been observed in devices up to thicknesses of several tens of layers[72]. With its high conductivity, graphite is an attractive option as a gate electrode in combination with hBN as dielectric[35]. It has been shown, that in graphene-hBN-graphite stacks, charge impurities were even further screened than in a configuration without graphite[35]. As a result, charge fluctuations in graphene are greatly suppressed in the presence of a graphite screening layer[35]. In addition, using graphite as contact material to contact graphene has also proven to yield exceptionally low contact resistances[85].

2.2 Quantum Hall Effect

In 1930 L. Landau realized that if a 2D electron system is subject to a strong perpendicular magnetic field, electrons are forced onto quantized cyclotron orbits[86]. However, to observe this quantized motion, high-mobility samples where charge carriers are tightly confined in one dimension, but mobile in the remaining two dimensions, as well as low temperatures were prerequisite[87]. Many decades later, in 1980, K. von Klitzing was able to overcome these challenges and demonstrated the quantized Hall effect as a direct consequence of the cyclotron motion of charge carriers[88]. This first demonstration of the quantum Hall effect (QHE) is one of the most fundamental discoveries in modern solid-state physics and has since then opened up a whole variety of new research topics[87]. Traditionally, 2D electron gases were realized by using either high-quality metal-oxide field-effect transistors or semiconductor heterostructures[87]. 2D materials, however, inherently support two-dimensional electron systems and are, therefore, a novel and versatile system to explore quantum Hall physics[89]. In the following, the quantum Hall effect is introduced and quantum Hall physics in graphene is discussed in detail.

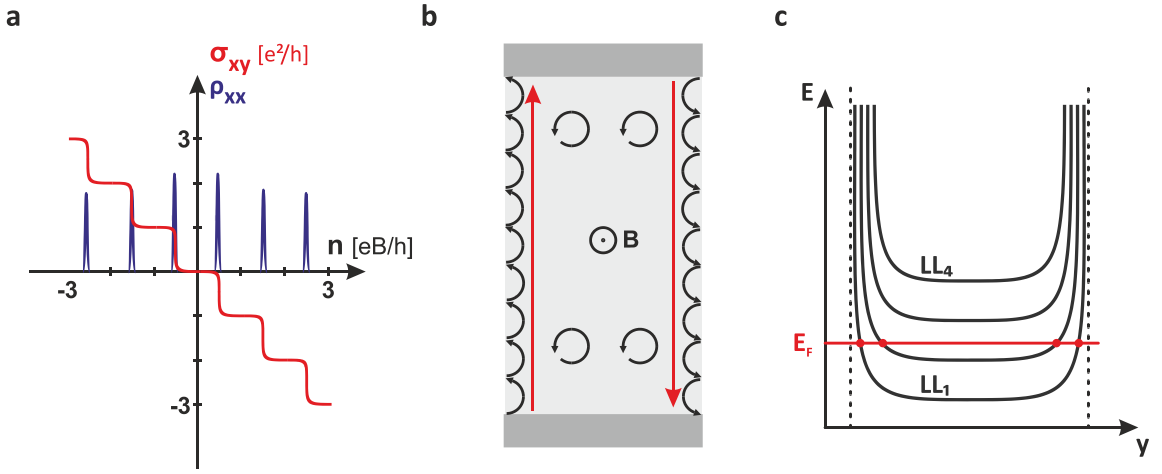

Figure 2.9 Quantum Hall Effect: *(a) Schematical transversal conductance (red) and longitudinal resistance (blue) as a function of the charge carrier density n in the quantum Hall regime. (b) Schematic illustration of the emergence of edge channels in graphene. In the center of the sample (light gray), charge carriers move in cyclotron orbits. Close to the edge of the sample, charge carriers are reflected and form a pair of directional edge channels connecting the two electrical contacts (dark gray). (c) The formation of edge channel from an energetic point of view. Close to the edge of the sample (dotted lines), the energy of the Landau levels increase. If the Fermi-energy E_F is located between two Landau level, edge channels at the crossing points between Fermi energy and Landau levels form.*

2.2.1 Classical Hall Effect

In 1879, E.H. Hall discovered that in a conductor subject to a magnetic field, a voltage transverse to the electric current and perpendicular to the magnetic field builds up[90]. This effect can be understood classically in terms of the Lorentz force acting on the charge carriers moving through the conductor[91]. It can be shown, that the transverse (Hall) voltage V_{H} and the corresponding transverse conductance σ_{xy} are given by[91]

$$V_{\mathrm{H}} = \frac{IB}{nde} \quad \text{and} \quad \sigma_{xy} = \frac{I}{V_{\mathrm{H}}} = \frac{nde}{B}, \tag{2.21}$$

where n is the charge carrier density, d the thickness of the conductor (in direction of the magnetic field), B the magnetic field, e the elementary charge and I the current through the conductor. Here, the notation with xy indicates that the voltage accumulates in transverse y direction, while the current flows in x direction. Thus, the Hall conductance σ_{xy} is proportional to the charge carrier density and inversely proportional to the magnetic field. The resistance ρ_{xx} along the channel, however, remains constant regardless of the magnetic field.

2.2.2 Two-Dimensional Electron Gas

In the limit of a 2D electron gas and low temperatures, the conductance σ_{xy} becomes quantized[91]. For example, when measuring σ_{xy} as a function of the charge carrier density, quantized conductance plateaus at integer multiples of e^2/h can be observed (see Figure 2.9a)[91]. At the same time, the longitudinal resistance ρ_{xx} vanishes at the conductance plateaus but exhibits spikes when the conductance increases to the next plateau (see Figure 2.9a). This behavior cannot be explained within the framework of the classical Hall effect. In order to understand these phenomena, consider a gas of free electrons in the xy plane with a perpendicular magnetic field in z direction. The Hamiltonian for this system is given by[86,91]

$$H = \frac{(p_x - eA_x)^2}{2m} + \frac{(p_y - eA_y)^2}{2m} + E_0, \tag{2.22}$$

where $\boldsymbol{A} = (0, -Bx, 0)$ is the vector potential with $\boldsymbol{B} = \nabla \times \boldsymbol{A}$ and E_0 is a momentum-independent energy contribution from the confinement in z direction. The magnetic field component forces the electrons to move in quantized cyclotron orbits within the xy-plane. As a result, the energy continuum of a free electron gas condenses into quantized energy levels, the so-called Landau levels, associated with these cyclotron orbits[87,88,91]. The Landau levels are given by[87,88,91]

$$E_N = E_0 + \left(N + \frac{1}{2}\right)\hbar\omega_C, \qquad N = 0, 1, 2, \ldots \tag{2.23}$$

with the cyclotron frequency $\omega_C = eB/m$. These Landau levels are degenerate with a degeneracy of $n_{LL} = eB/h$ each[87,88,91]. The Hall conductance at the N-th Landau Level can then be calculated using the formula for the Hall resistance in the classical case. Plugging in the degeneracy of the Landau levels yields[87,88,91]

$$\sigma_{xy} = \frac{nde}{B} = \frac{n_{LL}Ne}{B} = \frac{e^2}{h}N, \qquad N = 0, 1, 2, \ldots \tag{2.24}$$

This correctly reproduces the conductance values of the plateaus in Figure 2.9a, but does explain neither the step-like shape of σ_{xy} nor the resistance spikes of ρ_{xx}. Consider a rectangular sample hosting the 2D electron gas as shown in Figure 2.9b. As mentioned before, charge carriers are moving in quantized cyclotron orbits with a frequency ω_C inside the sample[91]. However, charge carriers can only perform undisturbed cyclotron orbits in the center of the sample (cf. Figure 2.9b). Close to the edges, their motion is limited by the sample boundary. As a result, charge carriers are reflected multiple times at the sample boundary and form a pair of edge channels in opposite directions (see Figure 2.9b). In fact, each of these pairs of edge channel contributes a conductance

quantum e^2/h to the Hall conductance[91]. Furthermore, since no back-scattering pathways are available, the longitudinal resistance ρ_{xx} of the edge channels vanishes.[91] This can also be seen from an energetic point of view as shown in Figure 2.9c: Due to the repeated reflections, the energy of the Landau levels are essentially bend upwards in energy the closer the states are to the sample boundary[91]. If the Fermi energy lies between two Landau levels, edge channels at the energy levels crossing the Fermi energy emerge[91]. In this framework, also the steps in σ_{xy} in Figure 2.9a can be explained. When the Fermi energy passes through a bulk Landau level, the conductance σ_{xy} jumps by one conductance quantum due to the formation of an additional pair of edge channels. Since the states close to the Fermi energy provide scattering pathways, the longitudinal resistance ρ_{xx} exhibits spikes[91]. However, if the Fermi energy is in-between two Landau levels, the number of edge channel stays constant[91]. Thus, the conductance σ_{xy} exhibits a plateau and the resistance ρ_{xx} vanishes[91]. Throughout this discussion, degeneracies of the electron gas, such as spin, have been neglected. Reintroducing a number of generic degeneracies g increases the degeneracy of each Landau level g-fold and leads to steps of ge^2/h in the Hall conductance. Furthermore, within this thesis, measurements are typically two-terminal measurements that can measure neither σ_{xy} nor ρ_{xx} directly. Instead, the two-terminal conductance $\sigma_{2\mathrm{T}}$ measures a combination of the two given by[92]

$$\sigma_{2T} = \sqrt{\sigma_{xx}^2 + \sigma_{xy}^2} \tag{2.25}$$

Thus, the two-terminal conductance still exhibits the same plateaus as σ_{xy}. It is also worth noting, that equation (2.25) is only valid for square samples and generally depends on the aspect ratio of the sample[92,93]. For higher and lower aspect ratios, plateaus are increasingly distorted and the quantum Hall effect is obscured[92,93].

2.2.3 Monolayer and Bilayer Graphene

So far, only a gas of free electrons has been considered. In graphene, however, charge carriers are chiral as discussed in section 2.1.1. The chiral nature of charge carriers and the corresponding Berry phase of π leads to an unusual sequence of conductance plateaus of the quantum Hall effect, the unconventional quantum Hall effect[58,89,94]. Similar to the free-electron case discussed in section 2.2.2, the sequence of Landau levels can be calculated by replacing $\boldsymbol{p} \rightarrow \boldsymbol{p} - e\boldsymbol{A}$ in the Hamiltonian of graphene (cf. section 2.1.1) and calculating the energy eigenvalues[95]. The Landau levels for monolayer graphene are given by

$$E_N^{(1L)} = \sqrt{2\hbar v_F^2 eB} \cdot \sqrt{N}, \qquad N = 0, 1, 2, \ldots \tag{2.26}$$

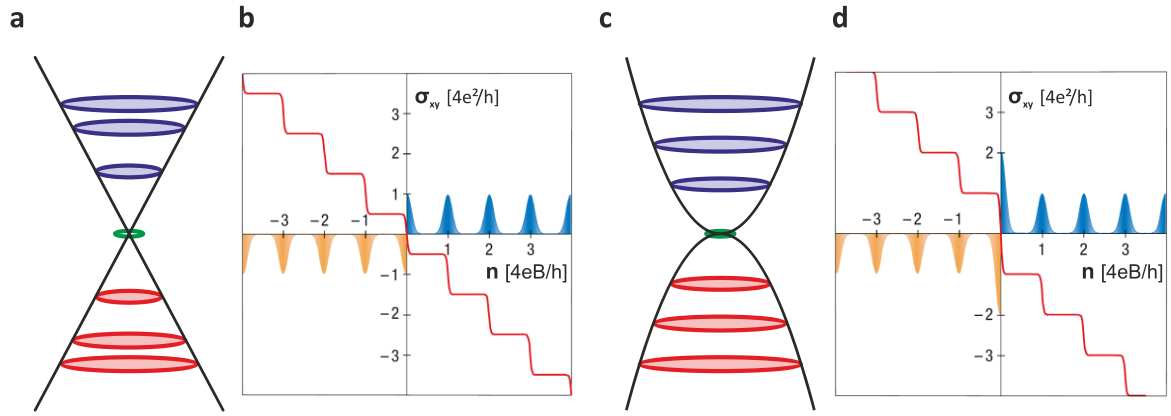

Figure 2.10 Quantum Hall Effect in Graphene: *(a) Schematic low energy dispersion of graphene together with the Landau levels with spacing $\Delta E = \sqrt{N}$ (b) Conductance σ_{xy} with respect to the charge carrier density. The density of states of the sequence of Landau levels are shown in blue and yellow for electrons and holes respectively. (c) Schematic low energy dispersion of graphene together with the Landau levels with spacing $\Delta E = \sqrt{N(N-1)}$. (d) Conductance σ_{xy} with respect to the charge carrier density. The density of states of the sequence of Landau levels are shown in blue and yellow for electrons and holes respectively. Adapted from Refs [56,96].*

Notably, unlike in the conventional quantum Hall effect, graphene has a zero-energy Landau level[95]. Since graphene has both spin and valley degrees-of-freedom, each of these Landau levels is fourfold degenerate. Like in the conventional case for a fourfold degenerate free electron gas, quantum Hall plateaus are separated by steps of $4e^2/h$ in monolayer graphene[1,95]. However, the first plateaus are shifted to $\pm 2e^2/h$ unlike in the conventional Hall effect[1,95]. The sequence of Landau levels and the conductance plateaus of monolayer graphene are shown schematically in Figure 2.10a,b. Bilayer graphene also hosts chiral quasiparticles, but with a Berry phase of 2π (cf. section 2.1.2). However, even though a phase of 2π is indistinguishable from zero, the Berry phase greatly modifies sequence of Landau levels[1,56]. In bilayer graphene, the Landau levels are given by[55,95,96]

$$E_N^{(2L)} = \frac{e\hbar B}{m} \cdot \sqrt{N(N-1)}, \qquad N = 0, 1, 2, \ldots \tag{2.27}$$

Here, the zero energy Landau levels has an additional twofold orbital degeneracy, since both $N = 0$ and $N = 1$ yield the same energy[55,56,95]. Thus, the quantum Hall plateaus in bilayer graphene are again separated by $4e^2/h$[55,56]. In contrast to monolayer graphene, however, the first plateaus are shifted to $\pm 4e^2/h$[55,56]. The sequence of Landau levels is shown schematically in Figure 2.10c,d.

2.2.4 Multilayer Graphene

As already discussed in section 2.1.3, the band structure of multilayer graphene depends strongly

on the stacking order. Consequently, the quantum Hall effect in multilayer graphene is stacking order dependent as well. First, the quantum Hall effect in ABC multilayer graphene is very much analogous to monolayer and bilayer graphene. Since quasi-particles are chiral with a chirality equal to the layer number N, they acquire a Berry phase of $\pm N\pi$ when going along a closed path[15,18,26,56,72,75]. As a consequence, zero-energy Landau level will have additional orbital degeneracies giving rise to an overall $4N$ degeneracy[56,62]. As a result, the first conductance plateaus will occur at $\pm 2Ne^2/h$[62,75]. All higher energy plateaus will be separated by $4e^2/h$ analogous to monolayer and bilayer graphene[12,75].

Surprisingly, in a first approximation the situation is the same for multilayer graphene with ABA stacking. As discussed before, multilayer graphene with ABA stacking order can be approximated as a superposition of bilayer bands together with an extra monolayer band for odd layer numbers[16,69–71]. Since monolayer has a 4-fold and bilayer an 8-fold degenerate zero energy Landau level, ABA multilayer graphene as a combination of the two has a $4N$ degenerate zero energy Landau level[16,71,80,97]. Consequently, the first conductance plateau will occur at $\pm 2Ne^2/h$ similar the ABC multilayer graphene[16,71,80,97]. All higher energy conductance plateaus inherit the $4e^2/h$ steps size from mono and bilayer graphene[16,71,80,97]. In fact, the same is true for multilayer graphene with arbitrary stacking order, as the band structure can always be decomposed into chiral building blocks (see also section 2.1.3)[80]. Including higher order hopping parameters lifts the degeneracy of the zeroth Landau level and leads to a complex landscape of Landau level crossings and anti-crossing originating from the monolayer and bilayer bands[71,97–99]. Additionally, as discussed in section 2.1.3, applying a perpendicular electric field, gives rise to emergence of Dirac gully triplets. As a result, the Landau level spectrum is expected to show a three-fold degeneracy at high electric fields in addition to the spin and valley degeneracy[20,100,101].

2.3 Electron-Electron Interactions

So far, the properties of graphene have only been discussed within a single-particle framework that completely neglects electron-electron interactions. Although this approximation is very successful in most situations, the single-particle picture may break down once the kinetic energy of electrons becomes comparable to the Coulomb interaction energy[24]. In this case, electron-electron interactions can no longer be neglected and may significantly alter the ground state of the system[24,102]. Indeed, by appropriately tuning the Fermi-energy as well as electric and magnetic fields, the ration between Coulomb interaction energy and kinetic energy can be tuned rendering several instabilities of the single-particle ground state experimentally accessible. In the following, the influence of interactions on the many-body ground state of multilayer graphene of either stacking order is discussed in detail.

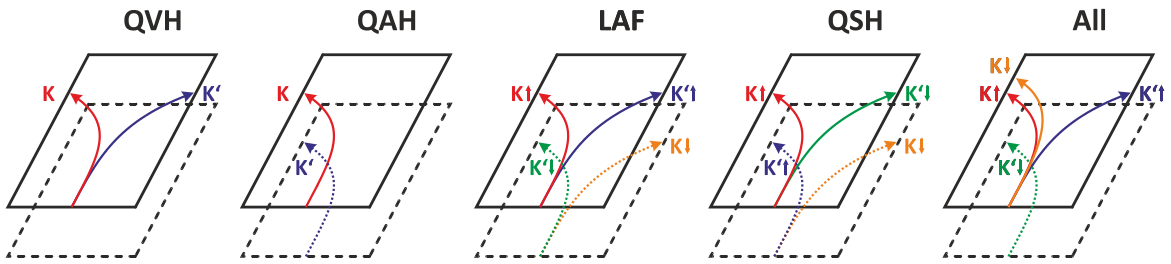

Figure 2.11 Broken-Symmetry Quantum Hall States: *Illustration of the quantum valley Hall (QVH) state, the quantum anomalous Hall state (QAH), the layer antiferromagnetic state (LAF), the quantum spin Hall state (QSH) and the "All" state. The top (bottom) layer planes are indicated by the solid (dotted) rhomboids and the spin-valley dependent Hall conductivities are indicated by the arrows pointing to either side of the rhomboids. The QAH state, for instance, has no net layer polarization, but exhibits a net charge Hall conductivity since the Hall conductivity contributions of both valleys add up. The QVH state, however, has a net layer polarization since all states are localized on the top layer, but remains insulating as the Hall conductivity contributions cancel out. Adapted from Ref [18].*

2.3.1 ABC Multilayer Graphene

It has been predicted that ABC multilayer graphene is particularly susceptible to interaction physics due to its flat low-energy band structure that strongly quenches the kinetic energy[18,26,103]. Given the power law dispersion that flattens with increasing layer number N (cf. section 2.1.3), the ratio r_S between Coulomb energy and kinetic energy scales approximately as[12,24]

$$r_S \propto n^{-(N-1)/2} \tag{2.28}$$

For monolayer graphene ($N = 1$), this parameters remains finite and interaction effects are independent of the charge carrier density n. For bilayer and multilayer graphene, however, the interaction parameter diverges close to charge neutrality and electron-electron interactions become dominant. As shown in section 2.1.3, quasi particles in ABC multilayer graphene are chiral with a pseudo-spin chirality equal to the layer number and acquire a Berry phase of $\pm N\pi$ when encircling the K or K' valley respectively. In general, interaction effects at charge neutrality can be captured by introducing a correction term into the single-particle Hamiltonian[18,28]

$$H = \frac{(v_F p)^N}{(\gamma_1)^{N-1}}\left[\cos(N\phi)\,\sigma_x + \sin(N\phi)\,\sigma_y\right] - \boldsymbol{\Delta}\cdot\boldsymbol{\sigma} \tag{2.29}$$

Here, $\boldsymbol{\sigma} = (\sigma_x,\sigma_y,\sigma_z)$ is a vector composed of Pauli matrices (cf. equation (2.8)) acting on the two-component spinor wave functions (see section 2.1.3). Depending on the orientation of the order

parameter $\boldsymbol{\Delta}$, different predicted symmetry breaking mechanisms can be described within this Hamiltonian. For instance, it has been predicted that $\boldsymbol{\Delta}$ is oriented along the x-y plane giving rise to gapless nematic states with broken rotational symmetry[23,28]. Yet, experiments[26–28] and perturbative renormalization group analysis[18,19,78] strongly suggest that $\boldsymbol{\Delta}$ aligns along the z-axis breaking chiral symmetry and likewise inversion symmetry. Similar to explicit chiral-symmetry breaking by applying an electric field (cf. equation (2.19)), spontaneous chiral-symmetry breaking opens up a gap in the electronic spectrum giving rise to a giant Berry curvature in the vicinity to the band minima[18]. Depending on the sign of Δ_z with respect to valley and spin, a family of five competing broken-symmetry states as summarized in Figure 2.11 have been predicted: The quantum valley Hall (QVH) state, the quantum anomalous Hall state (QAH), the layer antiferromagnetic state (LAF), the quantum spin Hall state (QSH) and the "All" state[18,19]. As they can be distinguished by their valley, spin and charge Hall conductivities that arise from the non-trivial Berry curvature, they are often referred to as spontaneous quantum Hall states[18]. Notably, the QVH and the "All" state exhibit a non-zero net layer polarization. Furthermore, the QAH and the "All" exhibit a non-zero orbital magnetic moment as well as a net (charge) Hall conductivity even in the absence of magnetic fields (cf. Figure 2.11). These properties are especially useful from an experimental point of view, as specific states can be favored by tuning the electric and magnetic fields[17,18]. For example, with increasing electric field, states that exhibit a net layer polarization, such as the quantum valley Hall states, are strongly favored[18]. So far, both the LAF phase and the QVH phase could be identified both in bilayer[28,104] and multilayer graphene[26,72,103,105]. However, the full phase diagram remains unknown with first indication of the presence of the QAH and the "All" state in bilayer graphene[27,106].

2.3.2 ABA Multilayer Graphene

As shown in section 2.1.3, the electronic structure of ABA multilayer graphene can be decomposed into $N/2$ bilayer-like bands for even layer numbers N with an additional monolayer-like band for odd layer numbers. Since the bilayer-like bands are essentially a limiting case of the previously discussed ABC multilayer graphene, interaction-induced chiral symmetry breaking is expected to open a band-gap in the electronic spectrum close to charge neutrality[69,79]. In monolayer graphene, however, interactions are weak and the spontaneous gap was shown to be either smaller than 0.1 meV or completely absent[107]. As a result, ABA multilayer graphene exhibits a peculiar even-odd effect: For even layer numbers, the band structure is gapped out due to the spontaneous gaps in all bilayer bands[69,79]. For odd layer numbers, however, the monolayer band closes this gap and obscures the spontaneous symmetry-breaking[69].

Nevertheless, ABA multilayer graphene also offers an alternative pathway to tune interaction physics via electric fields. As shown in section 2.1.3, strong electric fields lead to the emergence of two sets of three off-center Dirac gullies that are interconnected via C_3 rotational symmetry. As a result, upon applying a weak magnetic field, threefold quasi-degenerate Landau levels triplets

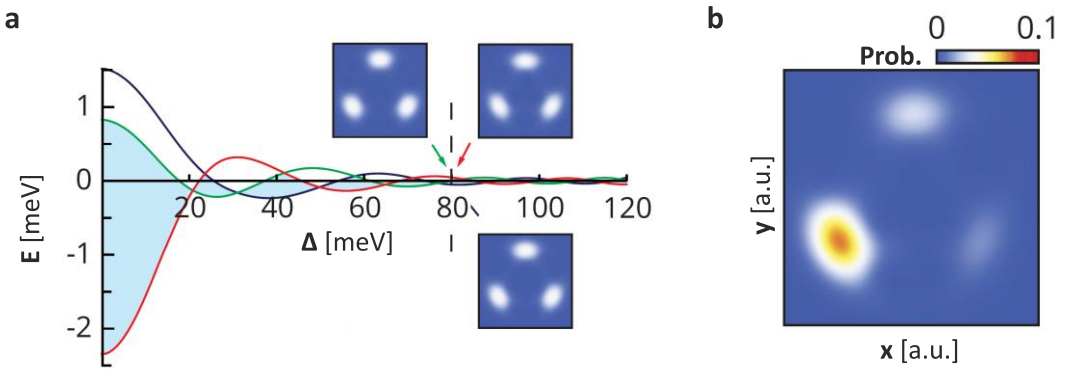

Figure 2.12 Spontaneous Gully-Polarized Nematic State: *(a) Energy evolution of the three Landau levels (red, green and blue) that make up the gully triplet state. The insets show the real-space probability distribution of the individual triplet wave functions close to the K point. When increasing the interlayer potential Δ by applying an electric field, the energy bandwidth of the triplet states decreases. The wave functions of the triplet states obey C_3 symmetry and are gully coherent. (b) Real-space probability distribution of the many-body Hartree-Fock ground state that spontaneously breaks C_3 symmetry. Adapted from Ref [101].*

associated with the Dirac gullies emerge (cf. section 2.2.4). When increasing the electric field, the Dirac gullies move further apart in momentum space and the triplet Landau levels become more and more degenerate[20]. Figure 2.12a shows the energy levels comprising an exemplary Landau level triplet and their evolution in electric field. In the absence of interactions, the triplet wave functions preserve C_3 rotational symmetry and are gully coherent (see inset in Figure 2.12a)[20]. However, increasing the electric field strongly quenches the kinetic energy (i.e. the bandwidth of the triplet state) until Coulomb energy dominates and interaction are expected to prevail[20,101]. Indeed, variational Hartree-Fock analysis indicates, that above a critical electric field, C_3 symmetry is spontaneously broken yielding a gully polarized nematic ground state as illustrated in Figure 2.12b[20]. First capacitance measurements have confirmed the spontaneous symmetry breaking by probing the lifted triplet state degeneracy, but the transport properties of these states remain unknown[101].

2.4 Field-Effect Transistors

Starting from the first demonstration of conductance modulation in a thin film by W. Shockley[108] in 1948, field-effect transistors (FETs) have found widespread use in both research and industry[109–111]. Out of the great variety of field-effect transistor types, the thin-film transistor is of particular importance for research applications and will be focused on in this section[109]. One of the great advantages of thin-film FETs is their low requirements for the active transistor material[109]. Besides semiconducting materials, the active layer can also be made out of semi-metals or even biological tissues[109]. This makes FETs a powerful tool to investigate charge carrier density and electric field

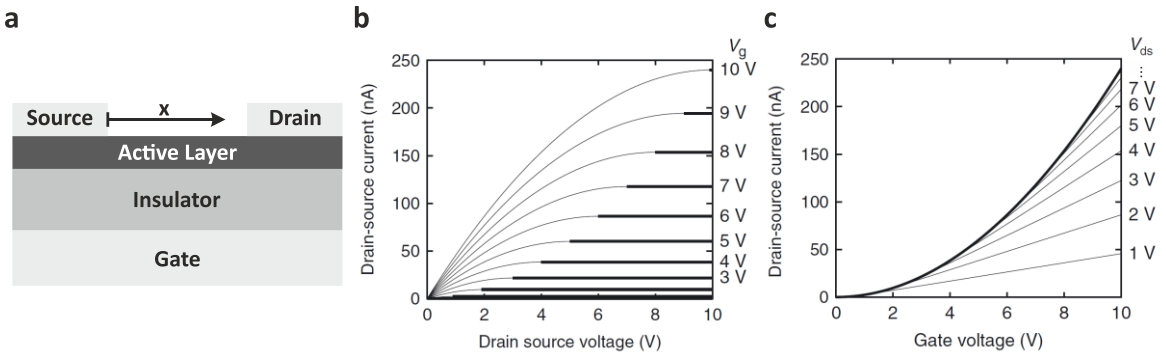

Figure 2.13 Field Effect Transistors: *(a) Schematic of a thin-film field-effect transistor. The active layer with source and drain contacts is separated from the gate electrode by an insulating dielectric material. (b) Output curves of an ideal transistor, where thick lines and thin lines indicate the saturation and the linear regime respectively. (b) Transfer curves of an ideal transistor, where thick lines and thin lines indicate the saturation and the linear regime respectively. In (b,c) the threshold voltage V_{th} is set to zero, and the electron and hole mobility are given by $\mu_n = 3 \times 10^{-4}\ cm^2\ V^{-1}\ s^{-1}$ and $\mu_h = 0\ cm^2\ V^{-1}\ s^{-1}$ respectively. Reprinted from Ref [109].*

dependent transport properties of a wide range of materials. In the following, the working principle and characteristics of FETs will be presented and their application for investigating quantum transport in graphene will be discussed.

2.4.1 Semiconductor Field-Effect Transistors

The (thin-film) FET consists of an active layer (e.g. a semiconductor) with source and drain contacts, which is separated from a gate electrode by an insulating gate dielectric (see Figure 2.13a)[109]. In a first simplification, the active layer can be treated as quasi-2D and the FET as a parallel plate capacitor with the gate electrode and the active layer playing the roles of the capacitor plates. Applying a voltage bias V_{DS} between drain and source electrodes will introduce a position dependent voltage $V(x)$ inside the active layer, where x measures along the channel from source to drain (see Figure 2.13a). For pure materials (no traps or doping), the free charge carrier density $n(x)$ accumulated in the channel is given by[109]

$$n(x) = C(V(x) - V_{\mathrm{G}})/e \tag{2.30}$$

where V_{G} is the voltage between gate and source, C the gate capacitance per unit area and e the elementary charge. In real devices, however, the gate voltage needs to fill all charge traps first, before any free charge carriers can be induced. Thus, the gate voltage is effectively shifted by an empirical threshold voltage $V_{\mathrm{G}} \rightarrow V_{\mathrm{G}} - V_{\mathrm{th}}$[109,112]. With equation (2.30) the current through the device

can be written as[109]

$$I(V_{\mathrm{G}}, V_{\mathrm{DS}}) = -en(x)\mu W \frac{\mathrm{d}V(x)}{\mathrm{d}x} \tag{2.31}$$

where μ is the charge carrier mobility and W the width of the channel. In general, the charge carrier mobility μ can be different for electrons and holes. Solving this differential equation yields the ideal characteristics of a FET as summarized by the output and the transfer curves (see Figure 2.13b,c)[109]. Within the FET characteristics, there are two regimes: the *linear region* for $V_{\mathrm{DS}} < V_{\mathrm{G}} - V_{\mathrm{th}}$ and the *saturation region* at $V_{\mathrm{DS}} > V_{\mathrm{G}} - V_{\mathrm{th}}$ (cf. Figure 2.13b,c)[109,111,112]. In these regimes, the solution to equation (2.31) is given by[111]

$$I_{\mathrm{D}}^{\mathrm{sat}} = \mu C \frac{W}{2L}(V_{\mathrm{G}} - V_{\mathrm{th}})^2 \qquad \mu_{\mathrm{sat}} = \frac{1}{C}\frac{2L}{W}\left(\frac{\partial\sqrt{I_{\mathrm{D}}}}{\partial V_{\mathrm{G}}}\right)^2 \tag{2.32}$$

$$I_{\mathrm{D}}^{\mathrm{lin}} = \mu C \frac{W}{L}\left[(V_{\mathrm{G}} - V_{\mathrm{th}})V_{\mathrm{DS}} - \frac{1}{2}V_{\mathrm{DS}}^2\right] \qquad \mu_{\mathrm{lin}} = \frac{1}{CV_{\mathrm{DS}}}\frac{L}{W}\frac{\partial I_{\mathrm{D}}}{\partial V_{\mathrm{G}}} \tag{2.33}$$

where L is the length of the channel and μ_{sat} (μ_{lin}) is the mobility calculated in the saturation (linear) region. Of particular interest when investigating semiconducting materials is also the density and depth of charge traps[113]. Within the FET framework, the density of deep traps N_{DT} far away from the Fermi-energy of the active material and the density of shallow traps N_{ST} close to the Fermi-energy can be estimated using[113]

$$N_{\mathrm{ST}} = \left(\frac{C}{ek_{\mathrm{B}}}\right)\frac{\mathrm{d}V_{\mathrm{th}}}{\mathrm{d}T} \tag{2.34}$$

$$N_{\mathrm{DT}} = \left(\frac{C}{e}\right)\left(\frac{eS}{k_{\mathrm{B}}T\ln 10} - 1\right) \qquad \text{with} \quad S = \frac{\mathrm{d}V_{\mathrm{G}}}{\mathrm{d}(\log I_{\mathrm{D}})} \tag{2.35}$$

Here, T is the temperature and S the subthreshold swing.

2.4.2 Dual-Gate Graphene Field-Effect Transistors

Besides the traditional semiconductor FETs, the FET geometry can also be used to investigate transport properties in graphene. When using single gate devices, both charge carrier density and electric field are tuned at the same time. Although the electric field component can be neglected for most materials, it has significant influence on charge transport in multilayer graphene as it introduces a potential difference between bottom and top layer (cf. section 2.1.3). Thus, it is

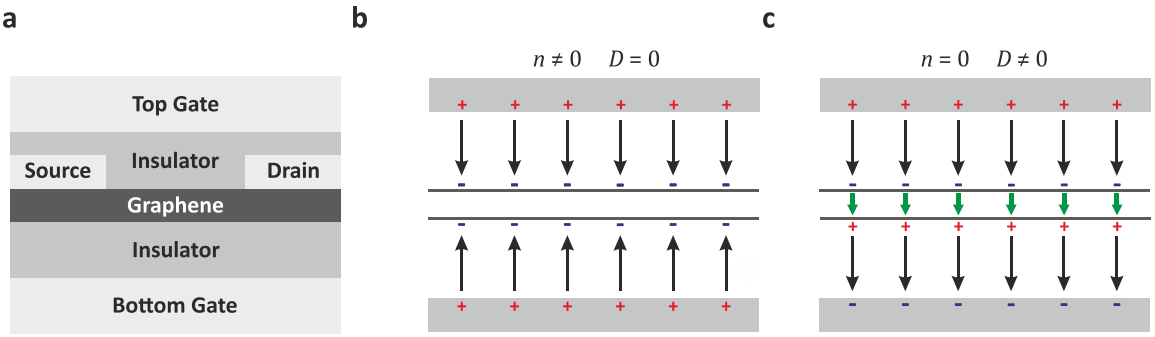

Figure 2.14 Dual-Gate Field Effect Transistors: *(a) Schematic of a dual-gate graphene field-effect transistor. Graphene is separated from both the top and bottom gate by two insulating dielectric layers. (b,c) Illustration of the electric field and charge carrier density that are induced in a (exemplary) bilayer graphene device (two dark lines) by two different configurations of bottom gate and top gate voltages. (b) For $V_T = V_B$ (and equal bottom and top gate capacitances) a non-zero charge carrier density is induced in the system, but no electric field. (c) For $V_T = -V_B$, the total charge carrier density is zero, but the electric field is non-zero.*

advantageous to disentangle the two components and tune charge carrier density and electric field independently. This can be done by using a dual-gate structure as shown in Figure 2.14a. In this case, the charge carrier density n can be decomposed into contributions from both the top gate voltage V_T and the bottom gate voltage V_B (similar to equation (2.30))[95,100].

$$n = (n_\mathrm{T} + n_\mathrm{B}) = \frac{(C_\mathrm{T}V_\mathrm{T} + C_\mathrm{B}V_\mathrm{B})}{e} = \frac{C_\mathrm{B}}{e}(\alpha V_\mathrm{T} + V_\mathrm{B}), \tag{2.36}$$

where C_T and C_B are the capacitances per unit area from the top gate and bottom gate respectively and $\alpha = C_\mathrm{T}/C_\mathrm{B}$ is the ratio between these two. The electric field D perpendicular to the graphene layer is given by the mean value of the electric field at the bottom and top gate electrode yielding[95,100]

$$D = \frac{1}{2}(D_\mathrm{T} + D_\mathrm{B}) = \frac{C_\mathrm{B}}{2\varepsilon_0}(\alpha V_\mathrm{T} - V_\mathrm{B}) \tag{2.37}$$

Figure 2.14 illustrates these relations for two different configurations of V_T and V_B. At this point, it is worth noting, that equations (2.36) and (2.37) are linearly independent and, thus, arbitrary combinations of n and D can be set by an appropriate choice of V_T and V_B. Inverting equations (2.36)

and (2.37) yields

$$V_{\mathrm{B}} = \frac{1}{2C_{\mathrm{B}}}(en - 2\varepsilon_0 D) + V_{\mathrm{B},0} \qquad V_{\mathrm{T}} = \frac{1}{2\alpha C_{\mathrm{B}}}(en + 2\varepsilon_0 D) + V_{\mathrm{T},0} \tag{2.38}$$

Here, in analogy to the introduction of the threshold voltage, $V_{\mathrm{B},0}$ and $V_{\mathrm{T},0}$ have been introduced to correct for charge traps screening the gate field.

3 Experimental Methods

In this chapter, the main fabrication and measurement techniques that are employed throughout this thesis are presented. During the course of this thesis, great focus was laid on adopting and optimizing several state-of-the-art fabrication and measurement techniques. Furthermore, a modular measurement software to perform electrical measurements with several different measurement devices has been developed. The chapter is organized as follows: First, the general procedure for fabricating high-quality 2D material devices is given. Second, the relevant methods for characterizing structural and optical properties of 2D materials are presented. Third, the measurement setups used for investigating the electrical transport properties of 2D materials and perovskites are discussed. In a last step, the brief overview over the measurement software developed during the course of this thesis is given.

3.1 Sample Fabrication

Within this thesis, two different sample geometries were fabricated (see Figure 3.1). First, suspended graphene multilayer devices with a silicon bottom gate and a gold top gate. Second, multilayer graphene devices encapsulated in hBN with both graphite contacts and graphite dual gates. The procedure employed to produce these two device types is different, but relied on several common fabrication techniques. In the following, all relevant fabrication steps are presented and the corresponding process parameters are given.

3.1.1 Wafer Preparation

For suspended devices, degenerately p-doped Si wafers with a 300 nm SiO_2 top layer were used as substrate. The doping level was selected in order to ensure low gate resistivities even at temperatures close to absolute zero. The thickness of the SiO_2 layer was chosen to enhance visibility of graphene and hBN in an optical microscope[1]. Prior to exfoliation, the substrates were cleaned in an acetone bath and a subsequent isopropanol bath for 3 min each. After blow-drying with dry air, they were plasma cleaned (PICO Plasma Cleaner, Diener) for 5 min at 50 W in 10 sccm O_2. For encapsulated devices, graphene and hBN samples that comprise the final stack were prepared on slightly doped Si substrates with a 300 nm SiO_2 top layer. Here, the focus was laid on ensuring that the flakes could be readily picked up from the substrates during the flake transfer step. Thus, prior

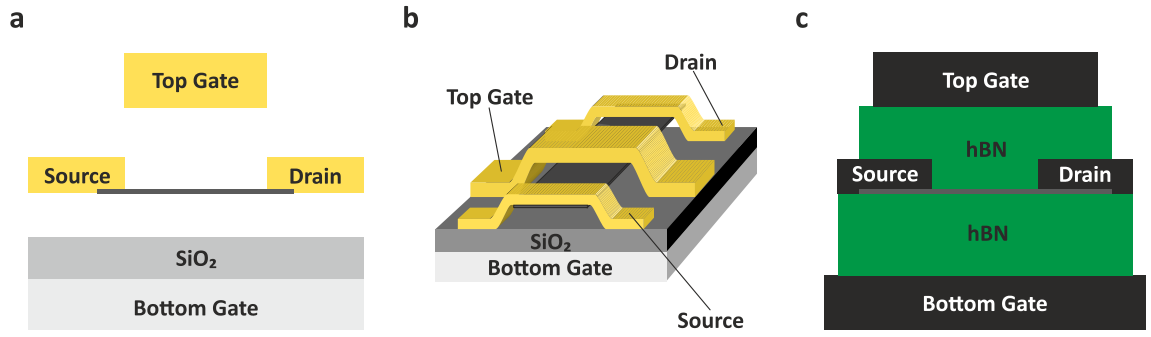

Figure 3.1 Graphene Device Structure: *(a,b) Line cut along the graphene axis (a) and 3D view (b) of a dual-gated graphene device with silicon bottom gate and a gold top gate. (c) Encapsulated graphene device with graphite contacts and graphite bottom and top gate.*

to exfoliation, the substrates were cleaned in Piranha acid for at least 20 min and etched in 5 % hydrofluoric acid (HF) for less than 10 s removing approximately 1 – 10 nm of SiO_2. This enhances the hydrophobicity of the substrate and was found to increase the yield of flake pick-up. After picking up all flakes of the stack, the stack was laid down onto a new substrate. This substrate was prepared similar to the suspended samples in order to enhance adhesion between the stack and the substrate.

3.1.2 Exfoliation

Throughout this thesis, few-layer graphene and hBN were obtained via mechanical exfoliation from bulk. This technique, although being very simple and cheap, has proven to yield high-quality flakes with excellent electrical properties[1]. For few-layer graphene, highly oriented pyrolytic graphite and natural graphite was used as bulk materials. Both materials display comparable characteristics, with the highly oriented pyrolytic graphite yielding smaller and natural graphite larger flakes. For exfoliation, a thin layer of graphite was peeled off the bulk graphite with an adhesive tape (Magic Tape, Scotch). By repeated peeling with scotch tape, the graphite on the tape was thinned down until only few layers of graphite remain. Directly prior to exfoliation, the substrates (see section 3.1.1) were preheated to 100 – 120 °C for several minutes. The scotch tape with the graphite was pressed onto the substrate for 10 – 30 s and then carefully removed. Few-layer hBN was exfoliated from crystals obtained from K. Watanabe and T. Taniguchi (National Institute for Materials Science, Tsukuba, Japan). The exfoliation of hBN is completely analogous to graphite. However, instead of scotch tape, blue Nitto tape (SWT20+, Nitto) was used. Furthermore, in order to increase the yield, hBN crystals were crushed into smaller grains prior to exfoliation. After exfoliation, promising flakes on the graphene or hBN wafers were located using optical microscopy and further analyzed with

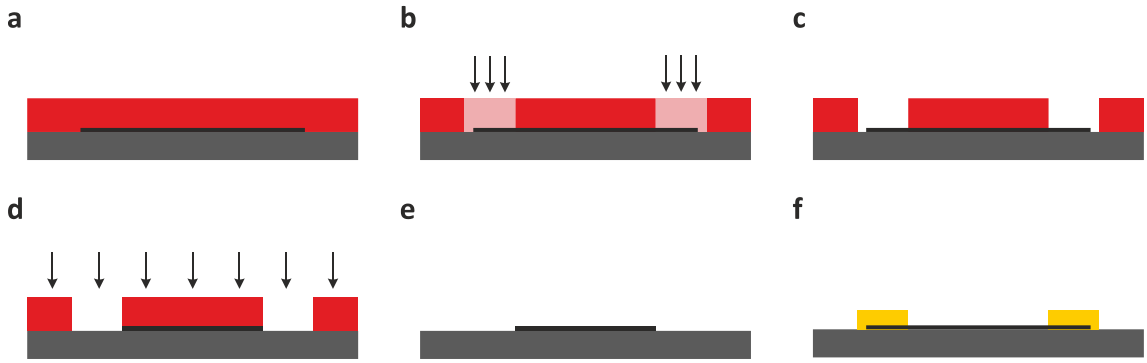

Figure 3.2 Electron Beam Lithography: *(a) First, the PMMA resist (red) is spin coated onto the substrate (grey) with the graphene or hBN flake (black) on top. (b) The regions that are supposed to be etched are exposed with an electron beam. (c) Immersing the sample in the developer dissolves the previously exposed areas. (d) The exposed graphene (or hBN) is etched in the ICP-RIE while the remaining graphene is masked by the resist. (e) In a final step, the resist is dissolved and lifted off. (f) Variation of (e) if metals were deposited in step (d) instead of etching.*

Raman spectroscopy, atomic force microscopy and scanning near-field optical microscopy (see section 3.2).

3.1.3 Structuring

In order to improve the overall homogeneity and cleanliness of the samples, it is often inevitable to remove undesired regions of the flake or stack. For example, if stacking order is important, it is highly advantageous to cut out the areas of the sample with homogeneous stacking order, since domain walls between stacking domains are very likely to move unpredictably during processing[114]. Furthermore, to enhance the stability of suspended graphene structures, it is advisable to structure graphene into ribbons of 1 – 2 µm width. Within this thesis, two methods for patterning graphene (and hBN) were used: reactive ion etching and scanning probe lithography. First, reactive ion etching is a very versatile method to etch materials of arbitrary thickness by bombarding them with reactive high-energy ions. In combination with electron beam lithography, it can be employed for nanostructuring of both graphene and hBN or combinations of them. Figure 3.2 shows a schematic overview of a typical reactive ion etching workflow. First, a 4.5 wt.% solution of the positive-resist polymethylmethacrylat (PMMA) 950 k dissolved in anisole (AR-P 672.045, Allresist) was spin coated onto the sample at 800 rpm for 1 s and then at 4000 rpm for 30 s. After spin coating, the resist was soft-baked at 150 °C for 3 min. Contacts were patterned via electron beam lithography at 10 kV with a dose of 110 µ C cm^{-2} and 170 µ C cm^{-2} for the 10 µm and 60 µm apertures respectively. The structures were developed in a 1:3 solution of methylisobutylketon (MIBK) in isopropanol for 2 min. After development, the samples were rinsed with isopropanol and blow-dried with dry air. Then the

structures were etched via inductively coupled plasma reactive-ion etching (ICP-RIE, Plasmalab System 100, Oxford Instruments). By using appropriate parameters and gas mixtures, the etching selectivity between graphene and hBN can be maximized. For selectively etching graphene, a flow of 10 sccm O_2 and a pressure of 10 mTorr with an ICP power of 70 W and a RF power of 144 W was used. This yielded an etching rate of 9 nm min^{-1}. For etching hBN, a flow of 10 sccm SF_6 together with 5 sccm Ar and a pressure of 10 mTorr with an ICP power of 70 W and a RF power of 50 W was used. Here, the etching rate was approximately 40 nm min^{-1}. In order to lift-off the remaining PMMA mask, the sample was submersed in acetone. Afterwards, the sample was soaked in N-Ethyl-2-pyrrolidone (NEP) at 60 °C for several hours to remove most PMMA residues and rinsed with acetone and isopropanol.

Although reactive ion etching is very effective and straightforward, inevitable PMMA residues strongly hamper subsequent flake transfer. Thus, reactive ion etching is not suitable to pattern graphene flakes that are set for encapsulation in hBN. Scanning probe lithography is an alternative state-of-the-art method for patterning thin materials that completely avoids device contamination[115]. In principle, it is based on a standard contact mode atomic force microscope (see section 3.2.3 for more details) with a metal tip[115]. By applying a high-frequency AC voltage bias between tip and substrate, the underlying material can be locally etched with nanometer resolution via anodic oxidation[115]. Moving the tip along a line or a predefined pattern allows for precise structuring of the underlying material[115]. Within this thesis, a gold tip and a constant contact-mode force of 100 – 150 nN and a scanning speed of 2 µm s^{-1} was used (see also section 3.2.3). The best etching results were achieved with an AC voltage bias of 10 V and a frequency of 40 kHz.

3.1.4 Flake Transfer

In order to fabricate encapsulated graphene devices, a technique to consistently pick up hBN or graphene flakes and transfer them to another substrate is imperative. In cooperation with S. Palmer, S. Wakolbinger, R. Schelwald, M. Dembecki and A. M. Seiler, a transfer technique that avoids interlayer contamination was adapted from P. J. Zomer[116] and D. G. Purdie[117]. In this method, flakes are transferred by means of a stamp that consists of a block of polydimethylsiloxane (PDMS) and a film of polycarbonate (PC). To build the stamp, PDMS was prepared using a commercially available kit (Sylgard 184, Dowsil) with a mass ratio of 10.5:1 between base and curing agent. After preparation, PDMS films with a thickness of approximately 2 mm were cast and dried in vacuum for 24 h in order to remove bubbles. PC films with a thickness of approximately 10 – 20 µm were prepared using a film application machine (ZAA 2300, Zehntner) with an 8 wt.% solution of PC (Poly(Bisphenol A carbonate), Sigma-Aldrich) in chloroform. Here, the total height of the blade (ZUA 2000, Zehntner) was set to 1675 µm and the speed to 6 mm s^{-1}. Afterwards, the PC films were dried for at least 1 h in air. Having prepared all components, a block of 2 × 2 mm of PDMS was cut out of the PDMS film and placed onto a precleaned glass slide. A window slightly larger than the PDMS

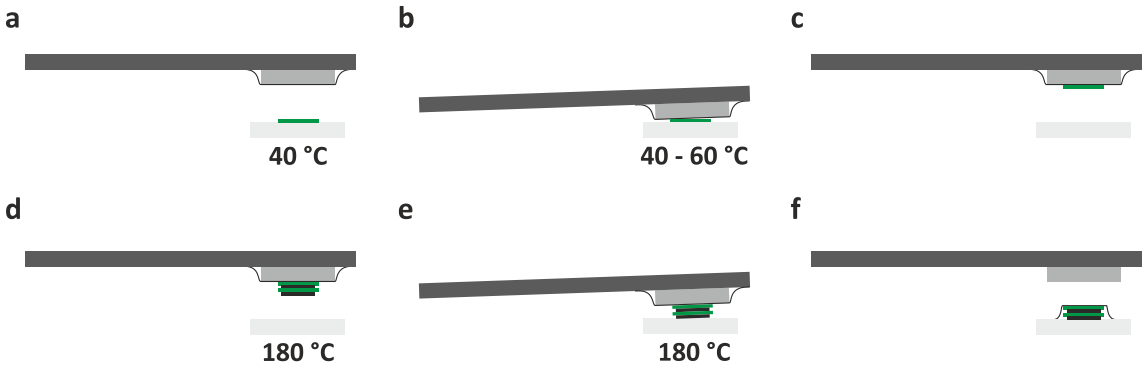

Figure 3.3 Flake Transfer: *(a) First, a hBN flake forming the basis of the stack has to be picked up. The hBN flake was positioned directly below the stamp and the substrate was heated to 40 °C. (b) In order to pick up the hBN flake, the stamp was slowly brought into contact with the substrate. Then the temperature was ramped to 60 °C and back down to 40 °C to bring the PC in contact with the flake during heating and delaminate it from the substrate upon cooling. (c) After pick-up, the stamp with the hBN flake was retracted. (d) Once all desired flakes had been picked up using the technique shown in (a-c), the substrate was heated to 180 °C. (e) The stack was laid down by slowly bringing the stamp and the stack into contact with the substrate. (f) The PC was melted together with the stack onto the substrate and the stamp was retracted.*

block was cut into a double-sided adhesive tape and placed onto the glass slide, such that the PDMS block sat inside the window of the adhesive tape. The PC film was picked up with another tape (again with a window slightly larger than the PDMS block) and placed on top of the PDMS block. The process of building a stack of encapsulated graphene is shown schematically in Figure 3.3. First, the top hBN flake was picked up. This was done by heating the sample stage to 40 °C and bringing the stamp into contact with the substrate. By heating the sample stage over the course of 20 min to 60 °C, the contact area between stamp and substrate increases and brings the hBN in contact with the stamp. Cooling down the stage back to 40 °C slowly retracts the stamp and delaminates the hBN from the substrate. It is worth noting, that these elevated temperatures are chosen in order to increase the adhesion of hBN to PC relative to SiO_2[117]. This process was repeated in order to pick up graphite contacts, the multilayer graphene flake, the bottom hBN flake and, lastly, the bottom graphite gate. In this process, the strong adhesion of graphene to hBN facilitates the delamination of flakes from the SiO_2. Except the first hBN flake, contact between the stamp and subsequent layers of the stack is minimized greatly reducing interlayer contamination. Once all flakes had been stacked onto each other, a clean substrate was prepared and heated to 180 °C above glass transition temperature of PC (T_G ≈ 150 °C[117,118]). Then, the stamp was tilted by a few degrees and brought into contact with the substrate. By slowly advancing the contact front, trapped interlayer contaminants can be pushed out yielding large, blister-free areas. At 180 °C, the PC primarily adheres to the SiO_2

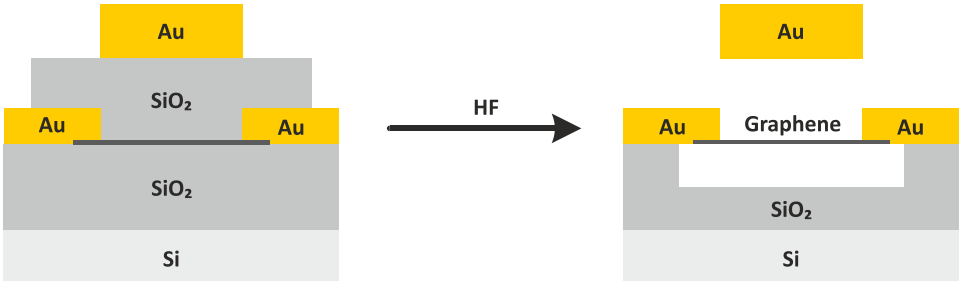

Figure 3.4 Suspending Dual-Gated Graphene Devices: *(a) Graphene on a Si/SiO_2 substrate with gold contacts together with an additional SiO_2 spacer and the gold top gate before etching. (b) Etching the structure with HF completely removes the SiO_2 spacer due to its low quality and isotropically etches parts of the SiO_2 of the substrate. Regions masked by the contacts remain protected, while regions directly below graphene are etched uniformly.*

instead of the PDMS. Thus, after 30 mins, the stamp can slowly be peeled away leaving the stamp together with the PC melted onto the substrate. In a last step, the PC was removed by soaking the sample in chloroform for at least 1 h. Thereafter, the stack was annealed in a vacuum chamber at a pressure of less than 1×10^{-8} mbar and 200 °C for 12 h to reduce the amount of bubbles further. The top gate was added by repeating this process: First, an hBN and, subsequently, a graphite flake were picked up. Then, both flakes were melted onto the already prepared stack. Finally, the PC was removed with chloroform and the stack was annealed again.

3.1.5 Contacting

In order to electrically contact the graphene flake, contact lines and pads were defined via standard electron beam lithography and metals were deposited. In encapsulated samples, electrical contact to the graphene flake was established via graphite contacts. Thus, only the graphite contacts and the two gates were contacted rather than the graphene flake itself. In suspended samples, however, the graphene flakes were contacted directly. The contacts were fabricated similar to the recipe presented in section 3.1.3. After defining the electrical contacts via electron beam lithography and developing the resist, metals were deposited in an electron-beam physical vapor deposition chamber (electron-beam PVD) at pressures of less than 5×10^{-7} mbar (see also Figure 3.2f). First, a 5 nm adhesion layer of chromium at a rate of 0.1 – 0.3 Å s^{-1} was evaporated. Second, a layer of gold at a rate of 0.8 – 1.4 Å s^{-1} was deposited. The thickness of the gold was chosen according to the application, but ranged between 50 nm and 150 nm. For suspended samples, the contact areas had been cleaned for 1 min in a UV/Ozone cleaner (UV Ozone Cleaner, Ossila) prior to metal evaporation in order to improve the contact resistance[119–121].

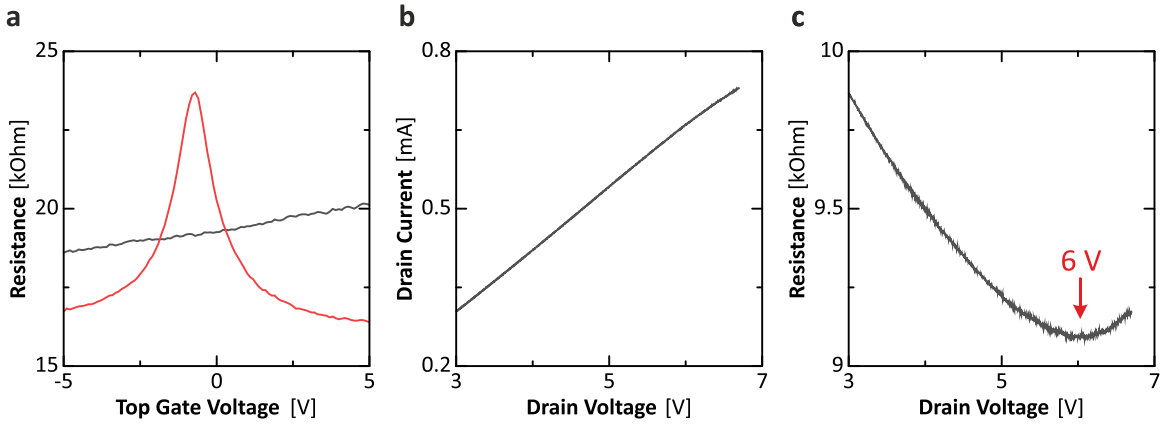

Figure 3.5 Current Annealing: *(a) Two-point resistance (including the line resistance of the cryostat) as function of the top gate voltage before (black) and after (red) current annealing. After current annealing, the resistance peak associated with the charge neutrality point of multilayer graphene is clearly visible. (b,c) Drain current and resistance of the final drain voltage ramp during the current annealing procedure. The drain voltage was ramped up to 0.7 V above the onset of the resistance increase at approximately 6 V (red arrow). The curve in (a) was measured directly after this ramp.*

3.1.6 Suspending and Wet Etching

In order to suspend graphene devices, a method developed by K.I. Bolotin[32] and extended by R.T. Weitz[17] was adapted. This method uses the fact, that HF based buffered oxide etch (BOE) etches SiO_2, but leaves graphene as well as gold and chromium unetched. Thus, submersing a fully processed graphene device in HF uniformly and isotropically removes the SiO_2 including at the area below the graphene flake (regions masked by contacts the remain unetched)[32]. The uniform etching below the graphene flake is rather surprising, but can be explained by a raping propagation of the HF along the graphene/SiO_2 interface[32]. As a result, the graphene flake is suspended between its metallic contacts. In order to fabricate dual gate devices, first a spacer of SiO_2 (see Figure 3.4a) was defined using electron beam lithography. The process was analogous to the recipe in section 3.1.3. However, instead of using one layer of resist, two layers and a development time of 3:30 min were used. Then, 140 nm of SiO_2 was evaporated via electron-beam PVD at a rate of 8 – 20 Å s^{-1}. In a next step, gate contacts with 5 nm of chromium and 160 nm of gold were defined in a similar way (see Figure 3.4a). In order to suspend graphene, the structure was submersed in BOE 1:7 for 100 s which removes approximately 150 nm of the SiO_2 substrate. The SiO_2 spacer that had been evaporated previously, however, was etched almost instantly due to its inferior quality. In order to prevent collapse during drying, the devices were transferred into an ethanol bath and dried in a critical point dryer (K850, Quorum Technologies). The resulting structure is shown in Figure 3.4b.

3.1.7 Bonding

Before measuring the electrical properties at cryogenic temperatures, the samples were mounted onto a sample holder with silver conductive paint. The contact pads were connected to the sample holder pins with gold wires using a wedge bonder (MEI 1204W, Marpet Enterprises).

3.1.8 Current Annealing

Suspended graphene devices typically have a substantial amount of contaminants and residues on the graphene surface that greatly reduce the quality of the device. Current annealing is an easy but yet very effective method to remove these contaminants in-situ by forcing a large current through the graphene device[122,123]. Due to dissipation, the high current density is accompanied by strong heating that removes the absorbed contaminations[122,123]. Figure 3.5a shows an exemplary measurement illustrating the increase in device quality during annealing. Within this thesis, current annealing was implemented as follows. The drain voltage across the graphene was ramped in consecutive runs to higher and higher values. Between each ramp, the quality of the device was monitored via gate sweeps. At some voltage, the drain current starts to saturate and the overall device resistance starts to increase (see Figure 3.5b,c). The best results were achieved, when annealing up to drain voltages approximately 0.7 – 1.5 V above the onset of the resistance increase.

3.2 Microscopy and Spectroscopy

In order to find suitable and high-quality multilayer graphene flakes as well as to characterize their structural properties, various microscopy and spectroscopy methods were employed within this thesis. First, multilayer graphene flakes were located and their layer number was determined using optical microscopy. In order to verify the number of layers and to determine the stacking order, Raman spectra were taken. The amount of dirt on the flakes or the presence of folds and wrinkles was determined via atomic force microscopy (AFM). Lastly, to visualize stacking order domains within the flake with nanometer resolution, scattering scanning near-field optical microscopy (s-SNOM) was employed. In the following, these methods are presented in more detail.

3.2.1 Optical Microscopy

After exfoliation, optical microscopy was used to locate promising flakes and determine their size, homogeneity and number of layers. Compared to other methods, optical microscopy has the advantage of being simple and efficient in mapping out an entire wafer in a reasonable amount of time. In addition, it provides a first measure of the layer thickness. Despite being only one atom thick, monolayer graphene absorbs a significant fraction of 2.3 % of the incident white light[124]. The absorbance of graphene is a direct consequence of its exotic electronic properties and is solely defined by the fine structure constant[124]. Furthermore, the absorbance of a graphene flake scales

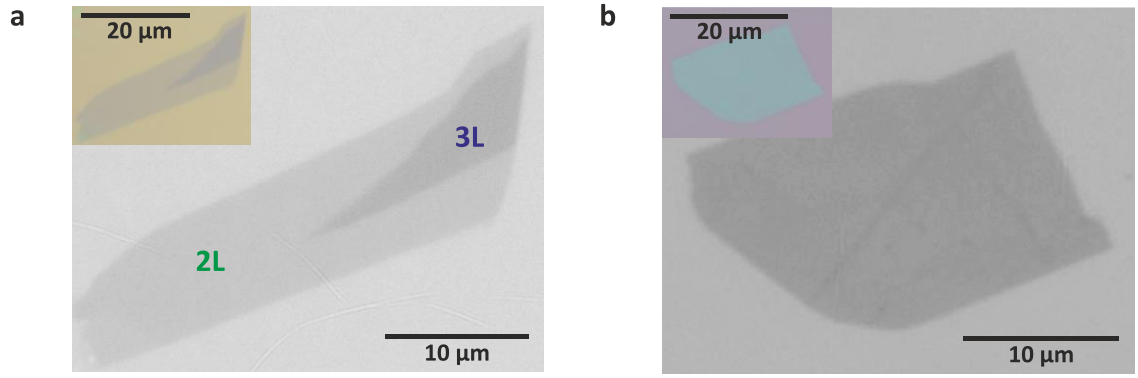

Figure 3.6 Optical Microscopy: *(a) Graphene flake on a Si/SiO_2 substrate with both bilayer (2L) and trilayer (3L) regions. The background-corrected grayscale image was calculated using the green channel only. The original full-color image is shown in the inset. (b) hBN flake on a Si/SiO_2 substrate. The background-corrected grayscale image was calculated from the red channel. The original image without the band-pass filter is shown in the inset.*

approximately linear with layer thickness[125]. The contrast in an optical microscope, however, is not only determined by the opacity of multilayer graphene, but also by the thickness of the SiO_2 and by the wavelength of the incident light[1,125,126]. For example, multilayer graphene with up to five layers is well distinguishable on a substrate with a SiO_2 thickness of 300 nm and white light illumination, but almost indiscernible on wafers with 200 nm SiO_2[125]. An example of an optical image and the optical contrast of graphene is shown in Figure 3.6a. In order to determine the layer number, the optical contrast C of the green channel is used as it yields the best results. In this context, the optical contrast is defined as

$$C = 1 - \frac{I_{\mathrm{G}}}{I_{\mathrm{BG}}}, \tag{3.1}$$

where I_{G} and I_{BG} are the intensities of the graphene flake and the background respectively. Within this thesis, a program to correct for a polynomial background (stemming from inhomogeneities in illumination intensity) and to determine the contrast of graphene flakes was developed. This allowed for fast image processing and provided a robust and consistent way to obtain graphene contrast values. The experimentally determined optical contrast values for graphene multilayers up to five layers are summarized in Table 3.1. However, due to the high standard deviation of the contrast values, the layer number has always been verified with Raman spectroscopy (see section 3.2.2). In contrast to graphene, the layer number of hBN flakes on a 300 nm SiO_2 substrate was best discernible when using a band-pass filter with λ = 650 ± 20 nm (see Figure 3.6b). However, the optical contrast only provided a rough estimate of the layer number and the AFM was used to determine the thickness of the hBN flakes (see section 3.2.3). For all contrast measurements, a 100x

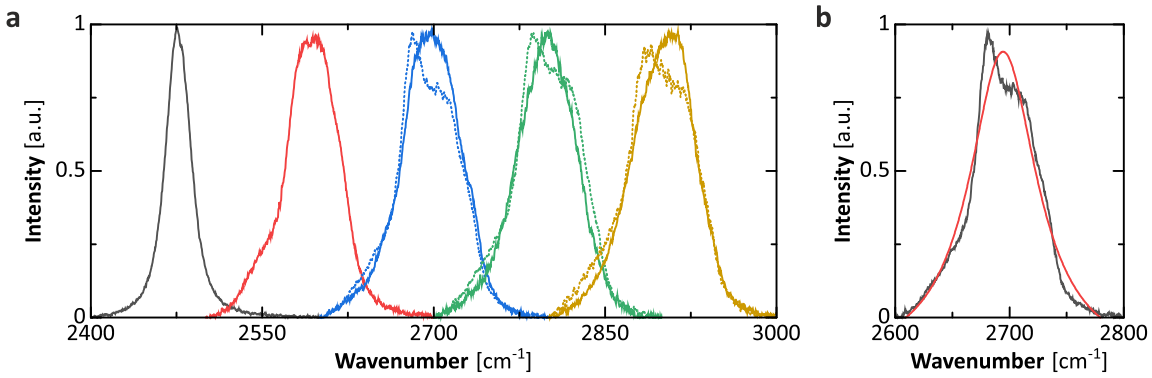

Figure 3.7 Raman Spectroscopy: *(a) Raman spectra of graphene with layer numbers of one (black) up to five (yellow). The spectra are normalized and offset by $\Delta\nu$ = 100 cm^{-1} from the trilayer spectrum for clarity. For more than two layers, the spectra corresponding to ABA and ABC stacking order are shown as solid and dotted lines respectively. (b) Raman spectra of ABC trilayer graphene (black) together with a Lorentzian fit (red) that allows to determine the FWHM.*

Measurement	Stacking	1L	2L	3L	4L	5L
Optical Contrast [%]	*Both*	2.6 ± 1.0	5.8 ± 1.5	8.7 ± 1.5	11.9 ± 1.5	15.9 ± 2.0
FWHM 2D Peak	*ABA*	26.5 ± 1.2	45.9 ± 1.2	49.3 ± 1.1	50.9 ± 0.9	53.0 ± 0.6
	ABC			54.6 ± 2.4	57.5 ± 1.9	58.0 ± 1.3

Table 3.1 Graphene Layer Number and Stacking Order Determination: *Experimental calibration data of both the optical contrast of the green channel and the FWHM of the 2D Raman peak from monolayer to tetralayer graphene.*

objective (LD EC Epiplan-Neofluar 100x, Zeiss) has been used.

3.2.2 Raman Spectroscopy

After selecting promising multilayer graphene candidates via optical microscopy, Raman spectroscopy was used to verify the number of layers as well as to determine and map the stacking order of the flake. For this purpose, the 2D Raman mode of multilayer graphene is especially suitable as its shape is very sensitive to stacking order and layer number[127]. The 2D peak originates from a second-order Raman process that involves two transverse optical phonons[127–129]. The line shape of the 2D peak is determined by the relative contributions of different scattering paths involving both conduction and valence bands[127,129]. Thus, it is sensitive to the band structure of the material at the given excitation energy[127,129]. As the band structure exhibits strong dependence on both layer number and stacking order (cf. section 2.1.3), the line shape of the 2D peak is a powerful tool to

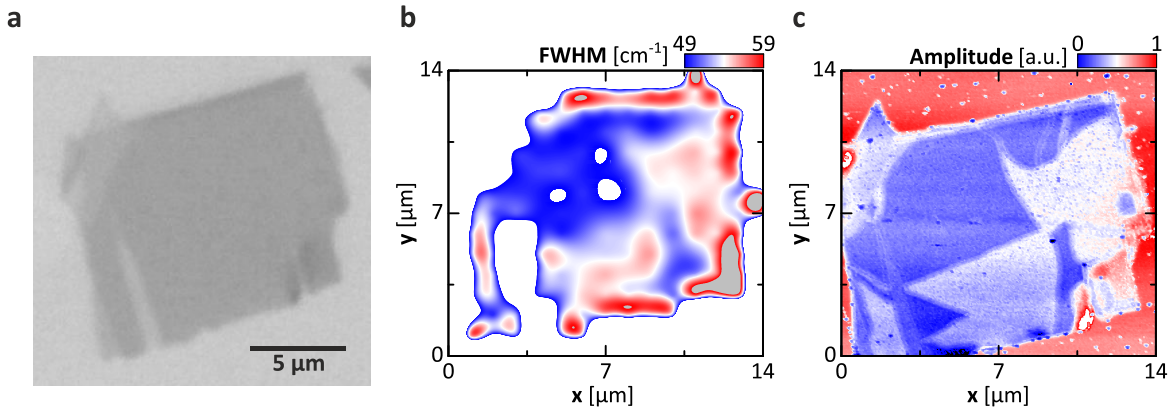

Figure 3.8 s-SNOM and Raman Maps of Trilayer Graphene: *(a) Background-corrected grayscale image of a trilayer graphene flake. (b) Raman map of the flake shown in (a) with the color indicating the FWHM. Higher values correspond to areas with ABC stacking order, lower to ABA stacking order. (c) Map of the SNOM scattering intensity of the flake shown in (a). Correlating the stacking order domains with the Raman map in (b) yields that blue domains correspond to ABA and white/red domains to ABC stacking order.*

assess the structural properties of graphene[13,127,130]. However, it is worth noting, that other factors such as strain or doping can influence the line shape of the 2D peak as well, but are expected to be much weaker[131–133]. To reduce complexity, fitting a single Lorentzian to the 2D peak and extracting the FWHM was shown to provide a facile and effective measure of the layer number and stacking order[130]. This also allows for generating maps of the stacking order by scanning the flake and extracting the FWHM of the 2D peak at each position. Unfortunately, the resolution is limited by the spot size of the laser of approximately 1 µm. Within this thesis, an excitation wavelength of 532 nm (Thorus 532, Laser Quantum) was used. The laser was focused onto the sample using a microscope with a 100x objective (MPlanFL N 100, Olympus) and spectra were recorded using a spectrometer (Spectrometer iHR550, Horiba Scientific) with a 1800 lines per mm grating. Calibration spectra of the 2D peak that were obtained for graphene flakes with up to five layers are shown in Figure 3.7. The spectra are in good agreement with the data presented in literature[127]. Furthermore, the corresponding FWHM values are given in Table 3.1. A Raman map of a trilayer graphene flake together with the optical image flake is shown exemplarily in Figure 3.8a,b. For hBN, however, obtaining the layer number via Raman spectroscopy is much more difficult as very low wave numbers in the range of 50 cm^{-1} have to be resolved and only layer numbers below ten are well distinguishable[134]. Since hBN flakes used for stamping typically have more than 10 nm thickness with several tens of layers, Raman spectroscopy is not suitable for hBN thickness determination. Instead, within this thesis, the thickness of hBN flakes is determined via AFM.

3.2.3 Atomic Force Microscopy

In order to obtain information about the homogeneity of promising flakes, the surface of the flakes was scanned with an atomic force microscope (AFM). For flakes to exhibit excellent electronic properties, the absence of folds and surface contamination is prerequisite. The latter is especially important when encapsulating graphene, as surface contaminants can be trapped between layers and influence charge transport unfavorably. In addition, the AFM was used to determine the thickness of hBN flakes, as optical methods do not provide a good measure for the layer number. It is also worth noting, that measuring the thickness of flakes only has nanometer precision due to the surface roughness of SiO_2 and is only feasible for hBN flakes. For graphene, on the other hand, this precision is unsatisfactory and the method does not yield consistent and reliable results[135]. Within this thesis, all AFM (Dimension 3100 and Dimension Icon, Bruker) measurements were done in tapping mode, where a tip oscillating at a constant frequency is brought into close proximity with the sample. Due to interactions with the surface, topography changes in the sample lead to a shift of the resonance frequency and, thus, of the amplitude of the tip. With a feedback loop, the vertical position of the tip is adjusted such that amplitude remains constant. Tracking the vertical position directly yields a topography map of the sample. As discussed earlier, the AFM was also used together with a metallic tip for graphene structuring (cf. section 3.1.3). In this scanning probe lithography method, the AFM was operated in the constant-force contact mode. Here, a non-oscillating tip is brought into very close proximity with the sample until the tip experiences a substantial repulsive force. When scanning the sample, the vertical position of the tip is set such that this force (as measured by the cantilever deflection) stays constant. Again, tracking the vertical position of the tip allows for extracting the topography of the sample.

3.2.4 Scattering Scanning Near-Field Optical Microscopy

To reveal the stacking order dependent electric properties of multilayer graphene, it is essential to be able to resolve the stacking domains down to nanometer scale. Raman spectroscopy, however, is limited by the spot size of the laser and is, thus, not able to detect stacking domains smaller than micrometer scale (cf. section 3.2.2). Scattering scanning near-field optical microscopy (s-SNOM), on the other hand, is able to probe local optical properties down to the nanometer regime well below the Abbe limit[114,136,137]. In principle, a s-SNOM is a tapping mode AFM with a metallic tip that serves as a nano-antenna. [136,138]. Shining an infrared laser onto this nano-antenna tip leads to a strong enhancement of the electric field between tip and underlying material making the system very sensitive to the local optical properties[136,138]. These local near-field properties are encoded in the back scattered infra-red light and can be read out in the far field[136,138]. Since the two stacking orders have distinctly different band structures, this allows to distinguish stacking domains by their relative scattering amplitudes[114,136,137]. Correlating domains with weak and strong scattering amplitudes with

a Raman map yields a nanometer resolution map of stacking domains[114,136,137]. Furthermore, electronic stacking faults that are not detectable with an AFM can be visualized with the s-SNOM[139,140]. At domain walls, surface plasmons are reflected and lead to interference fringes in the s-SNOM image[139,140]. All measurements within this thesis were performed with an experimental setup based on a commercially available s-SNOM setup (neaSNOM, neaspec). The wavelength of the infrared laser was 10.5 µm (CO_2 Laser Merit G, Access Laser Company) and the scattering amplitude was demodulated at the third harmonic of the tapping frequency. An examplary s-SNOM image together with an optical image and a Raman map is shown in Figure 3.8a-c. The domains in the Raman and s-SNOM map correspond very well, connecting low scattering amplitudes to ABA and high scattering amplitudes to ABC stacking domains. This example also illustrates the gain of several orders of magnitude in resolution compared to a Raman map.

3.3 Electrical Characterization

After sample characterization and fabrication, electrical transport properties of the multilayer graphene devices were investigated. All measurements on graphene shown within this thesis were two-terminal measurements. A first measure of the quality of the flakes was obtained with the room-temperature probe station. After preselecting promising flakes or contact pairs, the sample was transferred into the cryostat for measurements at temperature close to absolute zero. Besides graphene, also electrical characterization measurements on perovskite were conducted within this thesis. All temperature dependent measurements on perovskites were performed in a vacuum probe state station setup.

3.3.1 Probe Station

In order to assess the room temperature transport properties of graphene devices, samples were investigated in a simple probe station setup. The setup consists of needle probes that can be used to contact the source, drain and gate pads of the devices. The drain and gate voltages were applied and the corresponding currents recorded using source-measure units (SourceMeter 2450, Keithley). The source contact was used as reference potential for both drain and gate voltages and was connected to ground. Depending on the transport characteristic such as a low overall two-terminal resistance or a distinct resistance peak at charge neutrality (cf. Figure 3.5), promising flakes were preselected for cryostat measurements.

3.3.2 Vacuum Probe Station

Temperature dependent measurements on perovskites in a temperature range between 296 K and 7 K were conducted in a vacuum probe station (Probe Station CRX-VF, Lake Shore Cryotronics). Similar to the room-temperature probe station (cf. section 3.3.1), needle probes were used to

contact the drain and source device pads. In order to improve thermal conductivity, samples were glued to a copper plate with silver conductive paint and pressed onto the sample stage with an additional needle. The gate was contacted by placing a needle on the copper plate. Gate and drain voltages were applied and the corresponding currents measured with source-measure units (SourceMeter 2450, Keithley). The sample stage was coupled to a closed-cycle helium refrigerator and the temperature was adjusted using a temperature controller (Cryogenic Temperature Controller 336, Lake Shore Cryotronics).

3.3.3 Cryostat

During the course of this thesis, a cryogen-free dilution refrigerator measurement system (Dilution Refrigerator BF-LD250, Bluefors) was set up in order to measure electrical transport properties at temperatures as low as 7 mK. Additionally, the system is fitted with a superconducting magnet that is able to reach magnetic fields of up to 14 T. The cryostat consists of several temperature stages from room temperature down to the lowest temperature stage, the mixing plate. To transfer heat from the lowest to the highest temperatures stage, the cryostat is equipped with two closed-cycle cooling systems, namely a ^{4}He pulse-tube refrigerator system and a ^{4}He / ^{3}He dilution refrigerator system. The pulse-tube refrigerator is a closed-cycle system that uses ^{4}He at a pressure of some hundred mbar as refrigerant. It is able to provide cooling power down to approximately 3 K, the boiling temperature of the low-pressure ^{4}He gas. Starting from this temperature stage, the dilution refrigerator provides additional cooling to the mixing plate that can ultimately reach temperatures as low as 7 mK[141]. The working principle of the dilution unit is based on a peculiar property of mixtures between the two isotopes of helium, ^{4}He and ^{3}He. At zero temperature, instead of forming two separate pure phases, the amount of ^{3}He in the ^{4}He phase does not drop to zero and remains finite[141]. By pumping on this *diluted phase*, ^{3}He atoms evaporate and more atoms from the ^{3}He-rich phase (pure ^{3}He at zero temperature) have to be transferred to the diluted phase[141]. This process costs energy and, thus, provides cooling power down to the millikelvin regime[141]. Achieving these low temperatures, however, poses several challenges on designing electrical wiring inside the cryostat. Most importantly, wires connecting the measurement devices to the sample at base temperature introduce significant heating and need to be thermalized properly. This is achieved by several filter stages (self-made as part of this thesis) and thermalization stages (provided by Bluefors). Out of the 24 lines to the sample, four lines are equipped with stronger filters and are used as gate wires. The remaining lines provide medium filtering and are suitable for contacting the graphene devices. Furthermore, the lines are grouped into twisted pairs to minimize electromagnetic noise. An overview over the wiring is shown in Figure 3.9a and the design parameters of the filters are given in Table 3.2. First, just before going into the cryostat, a π-filter together with an RC-filter (only gate wires) prevents all high-frequency noise from entering the cryostat. Inside the cryostat, wires are thermalized at every temperature stage using bobbins

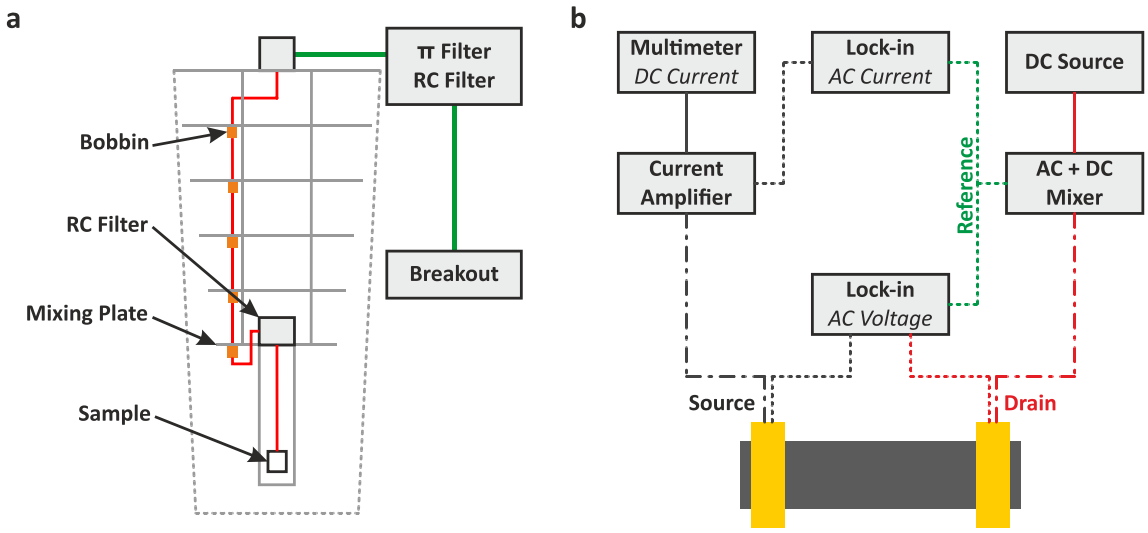

Figure 3.9 Cryostat Wiring and Lock-in Measurements: *(a) Wiring of the cryostat. From the breakout box, the wires (green) go through a π-filter and a RC filter before entering the cryostat (gray dotted area). Inside the cryostat, the wires are grouped in twisted pairs (red) and thermalized at every temperature stage (gray lines) with a bobbin (orange). At the mixing plate, the wires pass another RC filter before going to the sample. (b) Quasi four-point lock-in measurement connection scheme. Solid lines and dotted lines correspond to DC and AC components of the current respectively.*

Line Type	π-Filter	RC Filter warm			RC Filter cold		
	C [nF]	*R [kΩ]*	*C [nF]*	*f [Hz]*	*R [kΩ]*	*C [nF]*	*f [Hz]*
Gate	5.5	180	100	9	220	150	5
Source Drain	1.5	-	-	-	2.32	0.47	145960

Table 3.2 Filter Parameters: *Filter parameters for gate wires and source/drain wires.*

(provided by Bluefors). At the mixing plate, another self-made low-pass RC filter stage designed to maximize thermalization is added. The filter consist of a thin polyimide (Kapton) film glued onto a copper plate that is thermally anchored to the mixing plate. Long copper lines together with the shunt capacitance of the RC filter to the copper plate ensure good thermalization. The gate voltages were applied and gate currents measured with source-measure units (SourceMeter 2450, Keithley). The electric transport properties with respect to the gate voltages and magnetic field were measured with a standard lock-in technique (see Figure 3.9b). First, a self-made AC/DC mixer inductively modulated the AC reference signal of the lock-ins onto a DC bias (SMU GS610, Yokogawa). By using two different resistances for the AC and DC component, the voltages were converted to an arbitrary combination of AC and DC currents and applied to the drain contact. At

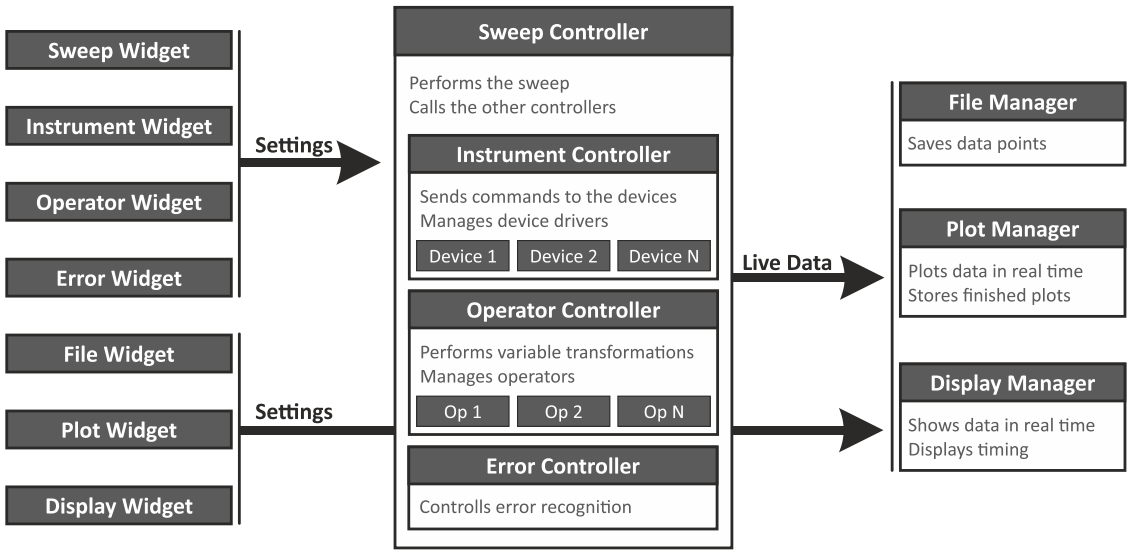

Figure 3.10 SuperFunAnalyzer Overview

the source contact, the current was amplified by a current amplifier (Model 1211, DL Instruments) and measured using a lock-in (Lock-in SR830, Stanford Research Systems) and a multimeter (Multimeter 34461A, Keysight). At the same time, the voltage drop over the device was measured by an additional lock-in (Lock-in SR865, Stanford Research Systems) using a quasi-four-terminal measuring geometry. Together with the current measurement, this allowed for calculating the differential resistance or conductance of the device.

3.4 Measurement Software

During the course of this thesis, the *SuperFunAnalyzer* (SFA), a software to perform arbitrary electrical measurements was developed. By use of a self-designed graphical user interface (GUI), the user can manage various measurement devices, set up sweeps of, for example, the gate voltage or the magnetic field, and define variable transformations such as $V_T, V_B \rightarrow D, n$ (cf. section 2.4.2). During measurements, the obtained data points are processed as well as displayed and plotted in real time. In the following, the structure of the software and its components are discussed in brief. An organigram of the structure of the SFA in shown in Figure 3.10. First, the software runs in two threads namely the sweep thread and the GUI thread. This separation was chosen in order to minimize timing errors during a measurement due to GUI calculations. Furthermore, it prevents the GUI from freezing during lengthy measurements. In principle, the SFA is divided into several separate core modules: The sweep controller, the instrument controller, the operator controller and the error controller are responsible for performing sweeps and device communication. The file manager, the plot manager and the display manager process the measured data in real time and

display as well as store the data points. Each of these core modules has a corresponding GUI widget associated with it that allows the user to control the behavior of the modules. For example, the instrument widget provide controls for the user to add instruments and modify their settings. In the following, the core modules and their function are explained in more detail. The sweep controller lives in the sweep thread and is the central module that manages the entire measurement. It takes the sweep variables (e.g. the drain voltage or the gate voltage) as user input and computes a list with all steps of the sweep. Going through the steps of the sweep, it employs the instrument controller to set device source values and read the measurement data. Furthermore, it uses the operator controller to perform variable transformations. Lastly, it hands the status and error messages acquired by the instrument controller to the error manager to check for errors. The live data is handed directly to the plot manager, the file manager and the display manager. The instrument controller lives in the sweep thread and is responsible for the entire instrument communication. For every instrument, a device specific driver file translates the abstract commands used in the SFA (such as “measure()”) to the instrument specific command (such as “SNAP? 2,3”). During the sweep, the instrument controller sends commands and receives status messages and measurement data from the measurement devices. The operator controller manages all user-defined variables. For example, the user may want to sweep the electric field D and the charge carrier density n instead of the top gate voltage V_T and bottom gate voltage V_B (see section 2.4.2). Alternatively, for example, if one is interested in not only plotting the drain current I_D, but also the resistance $R = V_D/I_D$, the variable R can be added as a new measurement variable. During the sweep, the operator controller transforms D and n back to V_T and V_B and calculates R for each data point. The error controller handles the status messages received from the devices, aborts the measurement if the device report critical errors, and displays an error message for the user. The remaining modules are rather self-explanatory: The plot manager plots data points and saves these plots, the display manager shows the current value of user selected variables, and the file manager writes data points to a .txt file. All of these three modules receive process and display data points in real time.

4 Spontaneous Gully Polarization in ABA Trilayer Graphene

Bernal-stacked multilayer graphene is a versatile platform to explore quantum transport phenomena and interaction physics due to its exceptional tunability via electrostatic gating. In particular, its band structure can be readily tuned to exhibit several off-center Dirac points (so-called Dirac gullies) in each valley by applying a perpendicular electric field. In this study, the formation of Dirac gullies and the interaction-induced breakdown of gully coherence is explored via magnetotransport measurements on high-quality Bernal-stacked (ABA) trilayer graphene encapsulated in hBN and equipped with both graphite gates and contacts. In the absence of a magnetic field, multiple Lifshitz transitions as function of electric field and charge carrier density indicating the formation of Dirac gullies are identified. In the quantum Hall regime and high electric fields, the emergence of Dirac gullies is evident as an increase in Landau level degeneracy. When tuning both electric and magnetic fields, electron-electron interactions can be controllably enhanced until the gully degeneracy is eventually lifted. The arising correlated ground state is consistent with a previously predicted nematic phase that spontaneously breaks the rotational gully symmetry.

The results presented in this chapter are currently being prepared for publication. The theoretical framework and the simulations presented within this chapter were provided by A. Ghazaryan and M. Serbyn (Institute of Science and Technology Austria, Austria). The graphene heterostructure was assembled and contacts were fabricated by A. M. Seiler, the scattering scanning near-field optical microscopy measurememts were provided by F. R. Geisenhof. All characterization and transport measurements as well as data analysis was done as part of this thesis.

4.1 Introduction

Since the advent of two-dimensional materials, graphene has attracted widespread attention due to its unusual electronic spectrum hosting massless Dirac fermions[1,58]. When increasing the number of graphene layers, stacking order as an additional degree-of-freedom allows for realizing superpositions of massive and massless Dirac fermions as well as chiral quasi-particles with cubic or higher power dispersions[12,14]. Additionally, the band structure of multilayer graphene can be tuned in-situ by applying electric fields[29,30]. This renders it possible to both access topology transformations

of the Fermi surface (Lifshitz transitions[81]) and to explore interaction physics solely via electrostatic gating[98]. However, excellent sample quality is necessary for observing these fragile electronic phenomena since charge disorder is expected to obscure their electronic signatures. In this study, magnetotransport measurements on high-quality Bernal-stacked trilayer graphene (b-TLG) encapsulated in hexagonal boron nitride with dual graphite gates and graphite contacts are reported. In the absence of an electric field, the band structure of b-TLG decomposes into a monolayer-like and a bilayer-like band[16]. An external perpendicular electric field introduces a potential difference Δ_1 between bottom and top layer. As a result, the two bands hybridize, driving the monolayer band to high energy and significantly deforming the low-energy bilayer band[20,29,30]. The interplay between trigonal warping arising from the skewed interlayer hopping term γ_3 and the electric field leads to the emergence of two additional sets of three off-center Dirac points related via C_3 symmetry, often referred to as Dirac gullies[20,29]. It has been predicted, that upon tuning electric and magnetic fields, electron-electron interactions within the Dirac gullies can be significantly enhanced and a new nematic ground state emerges, that spontaneously breaks the rotational gully symmetry[20]. This correlated state is highly reminiscent of nematic states observed in Bi[142] and predicted in SnTe[143] crystal surfaces, yet with additional tunability. Recently, quantum capacitance measurements on b-TLG devices have indicated the presence of a correlated ground state at high electric fields[101]. However, transport measurements exploring these correlated states are still lacking and it remains unclear, whether interactions merely produce short range ordering or percolating phases[142]. Likewise, Lifshitz transitions are promising candidates for hosting correlated states and have, for instance, been associated with superconductivity[144,145]. In b-TLG, several Lifshitz transitions driven by the formation of Dirac gullies are within experimental reach, but have not been investigated in transport so far.

4.2 Fabrication and Methods

The sample presented within this chapter has been prepared and identified as described in chapter 3. In brief, trilayer graphene flakes are exfoliated and identified by optical microscopy, Raman spectroscopy and atomic force microscopy (AFM). Additionally, scattering scanning near-field optical microscopy (s-SNOM) is used to ensure homogeneity of the samples and the absence of any domain walls. After identification, a region without domain walls was cut out using electrode-free scanning probe lithography[115]. Hexagonal boron nitride (hBN) and graphite flakes are obtained in the same way and their quality is ensured using optical microscopy and AFM. In order to access charge transport at high electric fields, a trilayer graphene flake is encapsulated in hBN with both graphite bottom and top gates using a dry transfer technique[116,117]. Low-ohmic electrical contact to the flake is established with two additional single-crystal graphite flakes in order to enable the use of a high-quality graphite top gate. In order to improve device homogeneity, the encapsulated

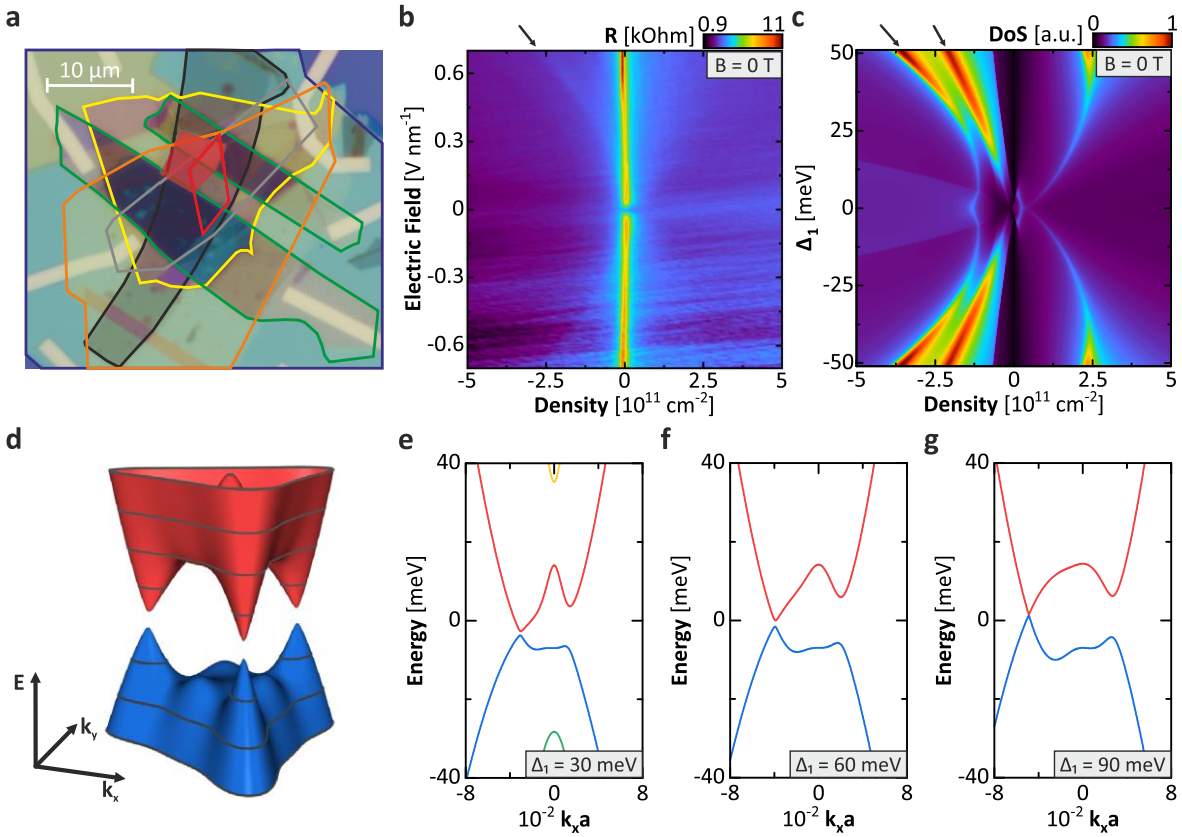

Figure 4.1 Device Geometry and Electronic Properties of Trilayer Graphene: *(a) Microscope image of the sample geometry. The investigated stack consists of the following layers (from bottom to top): bottom graphite gate (black), bottom hBN (blue), trilayer graphene (red), graphite contacts (green), top hBN (orange), top graphite gate (gray) and finally the termination hBN (yellow). The red shaded area has been etched out prior to the measurements. (b) Differential resistance as a function of charge carrier density and electric field in logarithmic color scale. The drift in graphite contact resistance with electric field has been corrected to enhance contrast. The parabola-shaped discontinuity is indicated by the arrow. (c) Simulation of the DOS as a function of charge carrier density and potential difference Δ_1. At parabolic contours, the Fermi surface topology changes (Lifshitz transition) leading to regions with an exceptionally high DOS. The scale of Δ_1 matches the scale of the electric field in (b). (d) Simulated three-dimensional band structure of b-TLG at Δ_1 = 50 meV demonstrating the emergence of Dirac gullies. (e-g) Evolution of the band structure of b-TLG for potential differences 30 meV (e), 60 meV (f) and 90 meV (g). Increasing Δ_1 drives the monolayer bands (green and yellow) to higher fields and leads to an increase in inter-gully distance Δk.*

sample was annealed in a vacuum chamber at 1×10^{-8} mbar at 200 °C for 12 h and unwanted contaminated areas ("bubbles") were etched away using reactive ion etching. A microscope image of the final stack is shown in Figure 4.1a. All measurements are done at cryogenic temperatures of < 10 mK in a dilution refrigerator using standard lock-in measurement technique at an AC frequency

of 78 Hz and currents of ≤ 20 nA. The stacking order is verified by comparing the Landau level crossings in the quantum Hall regime to theory. In fact, the stacking order was found to have transformed from ABC to ABA during the transfer process. By adjusting the bottom gate voltage V_B and the top gate voltage V_T of the graphite gates, both the charge carrier density $n = C_\mathrm{B}(\alpha V_\mathrm{T} + V_\mathrm{B})/e$ and the electric field $D = C_\mathrm{B}(\alpha V_\mathrm{T} - V_\mathrm{B})/2\varepsilon_0$ can be tuned independently (cf. section 2.4.2)[17]. Here, C_B is the capacitance per unit area of the bottom gate, α the ratio of top and bottom gate capacitances $\alpha = C_\mathrm{T}/C_\mathrm{B}$, e the electron charge and ε_0 the permittivity of vacuum. The parameter α was determined by sweeping the bottom gate at several top gate voltages and fitting a line along the conductance minima positions (see section 4.5 for more details). The contact resistance R_C and the bottom gate capacitance were extracted from quantum Hall measurements (see section 4.5).

4.3 Experimental Results

Figure 4.1b shows the differential two-terminal resistance R of a b-TLG device as a function of charge carrier density n and electric field D in the absence of a magnetic field. At zero doping, the resistance increases with increasing electric field indicating the opening of a small band gap. This is consistent with tight-binding calculations predicting the emergence a small band gap of a few meV that saturates within the experimentally accessible electric field range[20,146]. Additionally, the resistance displays faint discontinuities along a parabola-like contours. This is reminiscent of recent quantum capacitance measurements on b-TLG[101] and transport measurements on ABA tetralayer graphene samples[100]. In order to understand the transport features, tight-binding calculations based on the Slonczewski-Weiss-McClure[63–65] model to simulate the band structure of b-TLG have been conducted. Figure 4.1c shows the calculated density of states (DOS) as function of charge carrier density and electric field. In addition, Figure 4.1d shows the band structure of b-TLG with the emergent Dirac gullies at a potential difference of Δ_1 = 50 meV. When increasing the electric field and, thus, the potential difference Δ_1, the Dirac gullies move further apart from each other in momentum space (see Figure 4.1e-g). In fact, simulations show that the inter-gully distance Δk depends approximately linearly on the electric field $\Delta k \sim D$[20]. At low doping and high electric fields, the Fermi surface is composed of three disconnected pockets, whereas at high doping the Fermi surface consists of one single connected surface. In-between, when tuning the charge carrier density, the Fermi surface underdoes multiple discontinuous changes of its topology, so-called Lifshitz transitions[81]. These Lifshitz transition are accompanied by a logarithmically diverging DOS leading to anomalies in the conductance[20,100]. Comparing the conductance map to the predicted DOS yields fair qualitative agreement. Yet, the transport features are much fainter than expected and are suggestive of a much weaker increase in DOS than predicted. In particular, no signatures of correlated states as a consequence of a diverging DOS have been observed in agreement with

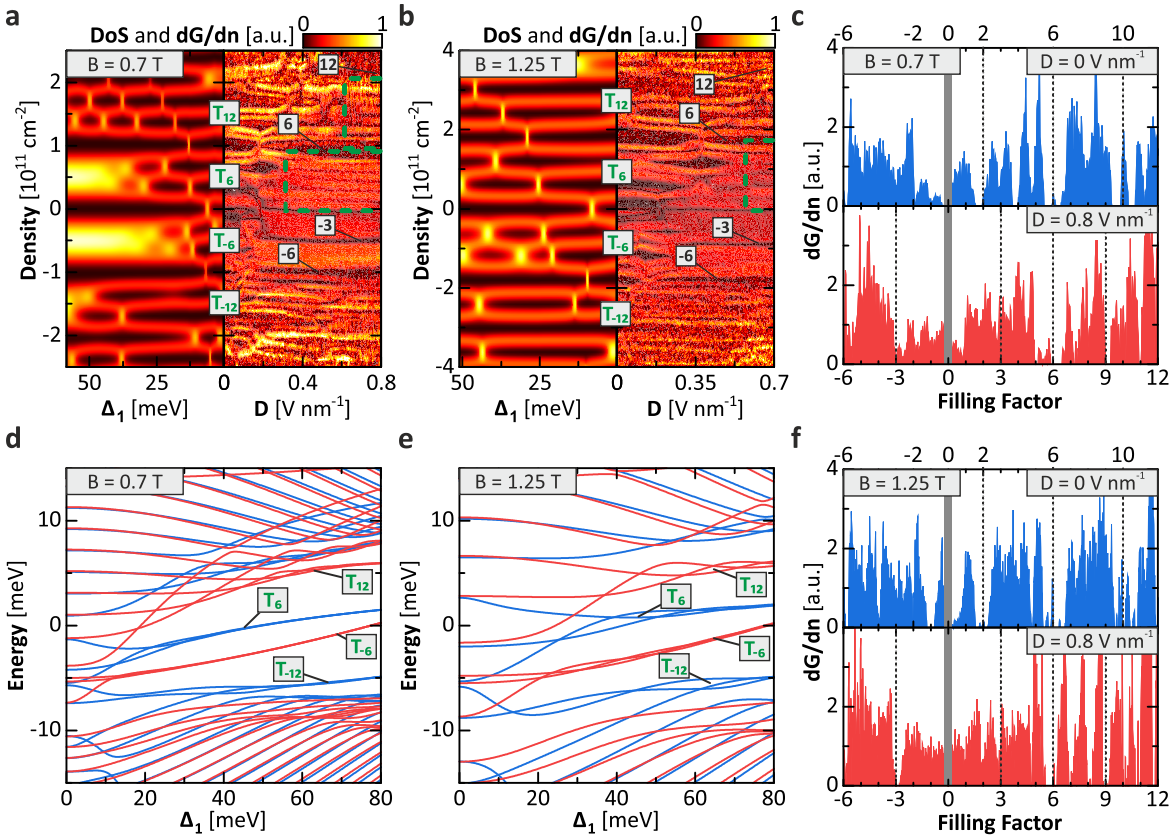

Figure 4.2 Landau Levels in Electric Fields: *(a,b) Simulated DOS (left) and measured derivative of the conductance with respect to the charge carrier density (right) of trilayer graphene as a function of potential difference Δ_1 and electric field D at B = 0.7 T (a) and B = 1.25 T (b). Dark regions correspond to vanishing DOS or derivative of the conductance (i.e. a conductance plateau) respectively. The region of full triplet state splitting is highlighted in green. (c,f) Line cuts along electric fields of D = 0 V/nm (blue) and D = 0.8 V/nm (red) at B = 0.7 T (c) and B = 1.25 T (f). (d,e) Theoretical evolution of spin-degenerate LLs stemming from the K (red) and K' (blue) valley as a function of the potential difference Δ_1 at B = 0.7 T (d) and B = 1.25 T (e). The triplet states are denoted by T_ν according to their associated filling factors ν and are also highlighted in (a,b). The charge neutrality point is located between the T_6 and T_{-6} triplets.*

previous measurements[101].

Beside the signatures of Lifshitz transitions at zero magnetic field, the emergence of Dirac gullies also manifests as an increase in Landau level (LL) degeneracy in the quantum Hall regime. In the absence of an electric field, LLs are spin degenerate and almost valley degenerate except for the zero energy LLs where valley degeneracy is broken[16,71,99]. In the gully regime at high electric fields, the LLs condense into two spin-degenerate triplets for electrons and holes each. These quasi-degenerate triplets are associated with one particular set of C_3-related gullies. The triplet wave functions inherit the C_3 symmetry and consist of a coherent superposition of contributions from all

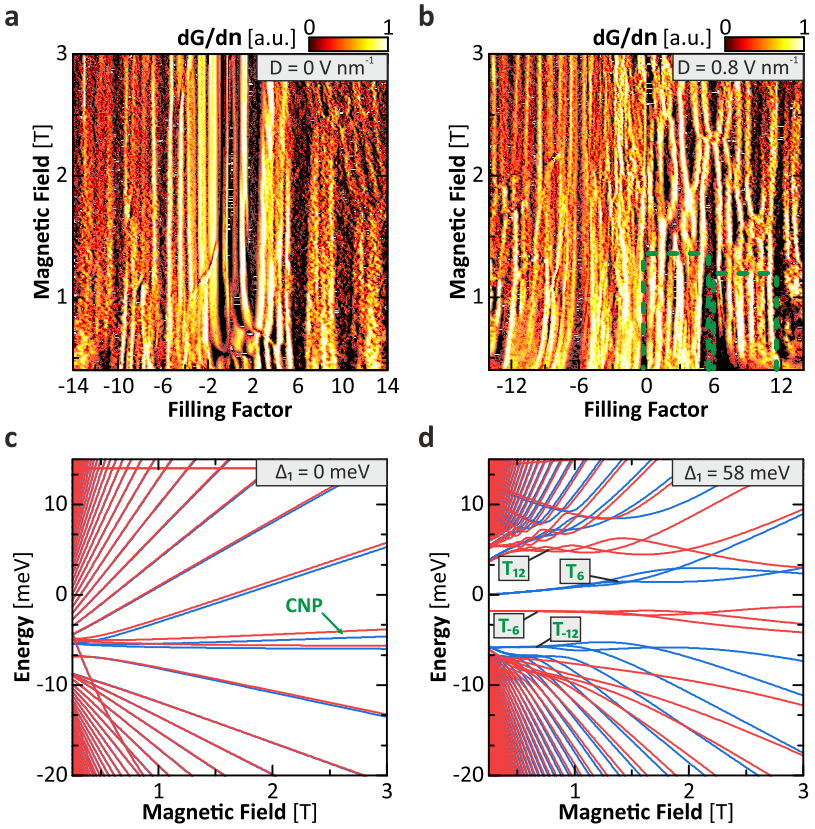

Figure 4.3 Landau Levels in Magnetic Fields: *(a,b) Derivative of the conductance with respect to the filling factor at D = 0 mV nm^{-1} (a) and D = 0.8 V nm^{-1} (b). The region of full triplet state splitting is highlighted in green. (c,d) Simulated evolution of spin-degenerate LLs at potential differences of Δ_1 = 0 meV (c) and Δ_1 = 58 meV (d) stemming from the K (red) and K' (blue) valley as a function of the magnetic field. The values for Δ_1 in (c) and (d) correspond to the electric fields in (a) and (b) respectively. The triplet states are denoted by T_ν according to their associated filling factor ν. The charge neutrality point (CNP) is located between the T_6 and T_{-6} triplets.*

three gullies[20]. Figure 4.2a,b shows measurements of the derivative of the conductance $\mathrm{d}G/\mathrm{d}n$ as a function of charge carrier density n and electric field D for two different magnetic fields of 0.7 T and 1.25 T respectively. Figure 4.2c,f shows high-resolution line cuts at two different electric fields. In order to provide further insights into the magnetotransport measurements, the evolution of LLs with respect to the potential difference Δ_1 and the magnetic field B has been simulated in a single-particle framework. The resulting DOS after artificial broadening of the LLs is shown together with the measurement data in Figure 4.2a,b. The evolution of spin-degenerate LLs with respect to Δ_1 and B are shown in Figure 4.2d,e. The latter nicely illustrates the formation of quasi-degenerate triplets from three intertwining LLs with increasing potential difference Δ_1. For later reference, the LL triplets are denoted by T_ν according to their associated filling factors of ν = ±6 and ν = ±12 as a

consequence of their combined spin and gully degeneracies. In the absence of an electric field, the most prominent conductance plateaus (minima of $\mathrm{d}G/\mathrm{d}n$) appear at filling factors ν = 2, (4), ±6, ±10 in agreement with theory. When increasing the electric field, a complex landscape of LL crossings emerges. Comparing the position of the LL crossings observed experimentally to the single-particle simulation in Figure 4.2a,b shows excellent agreement and unambiguously verifies the stacking order of the b-TLG. Additional measurements at higher charge carrier densities underline this close correspondence further and are presented in the appendix in Figure 4.5. In addition, by matching the positions of prominent LL crossings, Δ_1 can be related to D via an empiric conversion factor γ = 0.073 e/nm assuming a linear relationship $\Delta_1 = \gamma D$. At high electric fields, the condensation into LL triplets becomes apparent from the formation of prominent plateaus at ν = -3, ±6, 9, ±12 (see Figure 4.2c,f). This is consistent with the threefold gully degeneracy of the LL triplets, yet with broken spin degeneracy. Furthermore, the electric field onset of the triplet plateaus correlates positively with the magnetic field. For instance, the onset of the prominent ν = -3 plateau is at $D \approx 170$ mV nm^{-1} for B = 0.7 T compared to $D \approx 260$ mV nm^{-1} for B = 1.25 T. This observation aligns well with the single-particle simulations that predict a significant energy splitting increase of the triplet states for larger magnetic fields and can be understood as follows. At low magnetic fields and high electric fields, inter-gully tunneling is weak and the triplet states are quasi-degenerate[20]. Upon increasing the magnetic field, inter-gully tunneling becomes more and more dominant and the triplet state energy splitting increases until the triplets entirely lose their gully character[20]. This magnetic breakdown occurs when the magnetic length $l_B = \sqrt{\hbar/(eB)}$ with e being elementary charge becomes comparable to the distance Δk between Dirac gullies in k-space ($l_B \Delta k \approx 1$)[20]. Since $\Delta k \sim D$ as discussed earlier and shown in Figure 4.1e-g, both high electric fields and low magnetic fields stabilize gully triplets[20]. Thus, the critical electric field D_C below which gully physics breaks down and the triplet state energy splitting becomes significant depends on the square root of the magnetic field $D_C = \sqrt{B}$[20]. This relation indeed agrees well with the measurement data. In order to investigate the formation of triplet states further, measurements of the differential conductance dG/dv as a function of the filling factor ν and the magnetic field together with the simulated evolution of LLs as a function of magnetic field are shown in Figure 4.3. Further measurements at an intermediate field of D = 0.4 mV nm^{-1} are shown in the appendix in Figure 4.6. In agreement with the observations made before, plateaus associated with gully triplets stabilize at low magnetic fields and high electric fields.

While the aforementioned features of the magnetotransport measurement are consistent with the single-particle simulations, many observations cannot be explained in a non-interacting framework. For instance, in the absence of electric fields, all integer filling factors between $-10 \leq \nu \leq -2$ are already well-resolved at B = 1.25 T, some integer filling factors even well below B = 0.7 T. This electron-electron interaction induced spin and valley degeneracy breaking underlines the excellent

quality of the investigated flake and hints towards a dominant influence of electron-electron interactions within the system[97,98]. Furthermore, in the gully regime at high electric and low magnetic fields, multiple integer plateaus at filling factors -12 ≤ ν ≤ -12 are well resolved. This is especially apparent for the T_6 and T_{12} triplet: Below a critical electric field and above a critical magnetic field, several LL crossings stemming from the intertwining triplet states are visible. When going across the critical field, LL crossings are completely absent and all integer LLs are readily observable (highlighted by the green box in Figure 4.2a,b and Figure 4.3a,b). This indicates that both spin and gully degeneracy are broken. In contrast, the gully degeneracy of the T_{-6} triplet seems to be much more persistent and only spin degeneracy appears to be broken. However, at maximum electric field and B = 0.7 T, first indication of developing integer plateaus of the T_{-6} triplet are evident. Together, these observations strongly hint towards an interaction-induced symmetry-breaking of triplet states. Indeed, in a simplistic picture, increasing the electric field quenches the energy splitting of the individual LLs that comprise the triplet states. Thus, the Coulomb interaction energy $E_C = e^2/(\varepsilon_{\mathrm{hBN}} l_B)$, although being screened by the hBN ($\varepsilon_{\mathrm{hBN}} \approx 6.9$[147]), eventually becomes dominant compared to the kinetic energy and interaction physics is expected to prevail[101]. First indication of a broken triplet degeneracy has also been seen in previous capacitance measurements[101], yet neither its transport properties nor the ordering length scale could not be accessed so far. In order to understand this breakdown of the single-particle picture in more detail, a variational Hartree-Fock analysis to model interaction effects and to reveal the ordering of the ground state of the system has been employed[20]. In the Hartree-Fock analysis, only the lowest energy state (i.e. 1/3 filling of a triplet ignoring spin) was considered. For small electric fields within the gully regime, the Hartree-Fock ground state essentially coincides with the single-particle ground state. The wave function is completely gully coherent and obeys C_3 symmetry. At high electric fields, however, the Hartree-Fock analysis yields that C_3 symmetry is spontaneously broken and the ground state is a nematic gully polarized state[20]. The transition between these two regimes is of first order and takes place at a critical electric field $D_{\mathrm{C}}^{\mathrm{HF}}$. This agrees very well with the measurement results that displays a sudden change in LL degeneracy that is associated with a critical field (green line in Figure 4.2a,b and Figure 4.3a,b). Furthermore, the measurements also show a higher critical field for the T_{12} triplet compared the low energy T_6 triplet in agreement with the Hartree-Fock simulations[20]. However, the absence of broken-symmetry states in the T_{-6} triplet is unexpected, but could also be related to the overall inferior device performance on the hole side of the spectrum. Although these measurements strongly indicate the presence of a nematic phase, further measurements transport anisotropies are needed to verify the symmetry of the correlated ground state.

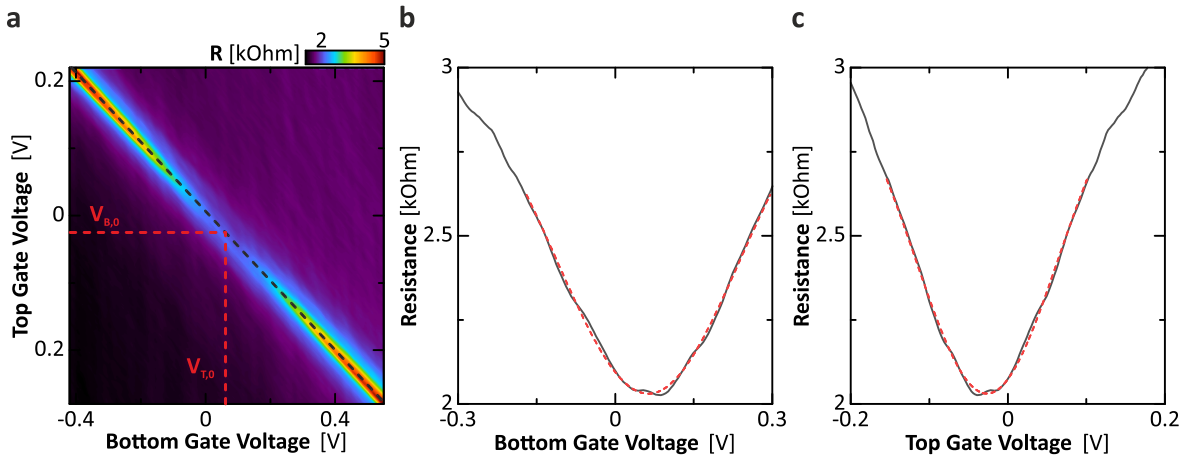

Figure 4.4 Calibration of Charge Carrier Density and Electric Field: *(a) Resistance as a function of the bottom gate and the top gate voltage. On every column of the plot, the resistance peak position is extracted by performing a Gaussian fit. Connecting all peak positions and fitting a line yield the charge neutrality line (dotted black). (b,c) Resistance as a function of bottom gate voltage (b) and top gate voltage (c) measured along the charge neutrality line. By fitting a Gaussian to the resistance minimum of the line profile with respect to the bottom gate and top gate voltage, the offset voltages $V_{B,0}$ and $V_{T,0}$ can be extracted. These offset voltages are also indicated in (a).*

4.4 Conclusion

To sum up, b-TLG has been encapsulated in hBN and equipped with both dual graphite gates and contacts. Upon applying electric fields, the band structure of b-TLG transforms and multiple off-center Dirac gullies emerge at each valley. By electrostatically tuning both the electric field and the Fermi energy, the Lifshitz transitions necessitated by the formation of Dirac gullies is observed in transport. Although being predicted to have a diverging density of states, no signature of correlated states are found. In the quantum Hall regime, the Dirac gullies give rise to the formation of triplet states that modify the sequence of LLs. By tuning electron-electron interactions via electric and magnetic fields, transport measurements demonstrate the emergence of new interaction-driven percolating ground state that breaks the triplet state degeneracy. This correlated state is consistent with Hartree-Fock simulations that predict a gully polarized nematic ground state at high electric fields that spontaneously breaks rotational symmetry.

4.5 Appendix and Supporting Information

In this section, further measurement and calibration data not shown within the discussion in section 4.3 is presented. The additional data supports the presented results and is shown for completeness

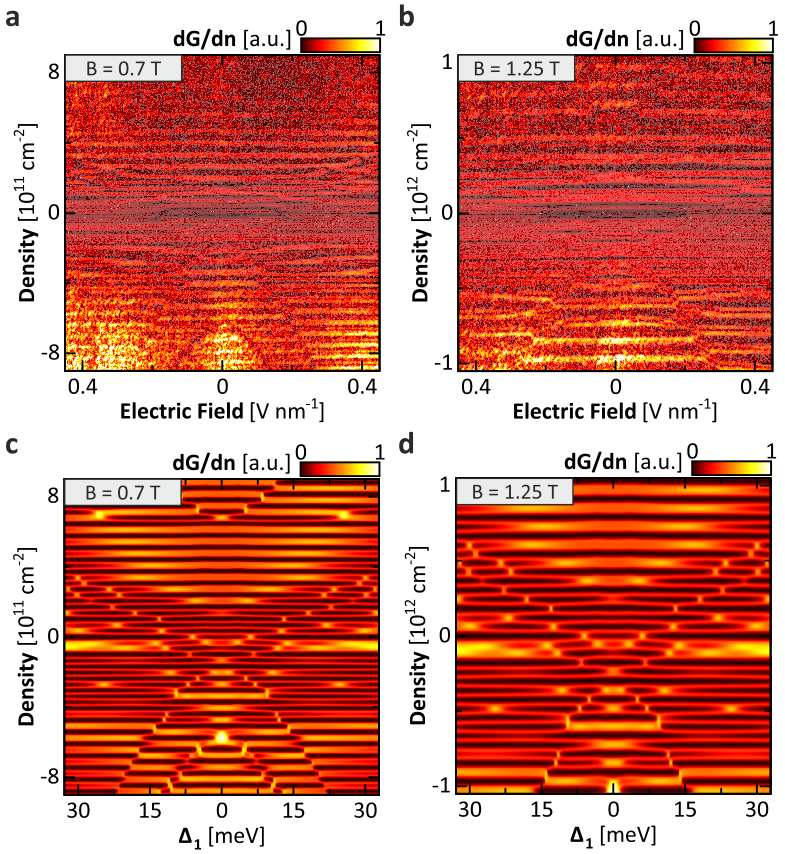

Figure 4.5 Magnetotransport at High Charge Carrier Densities: *(a,b) Derivative of the conductance with respect to the charge carrier density as a function of electric field and charge carrier density at a magnetic field of B = 0.7 T (a) and B = 1.25 T (b). Conductance plateaus are indicated by a vanishing conductance derivative. (c,d) Simulated DOS as a function of charge carrier density and interlayer potential difference at B = 0.7 T (c) and B = 1.25 T (d). The scaling of Δ_1 in (c,d) corresponds to the scaling of D in (a,b).*

and reference.

Calibration of Dual-Gate Transport

In order to transform the top gate voltage V_T and the bottom gate voltages V_B to electric field D and charge carrier density n (see section 4.2 and section 2.4.2), the resistance as a function of the bottom gate voltage is recorded for several different top gate voltages as shown in Figure 4.4a. At every line, the center of the resistance peak is determined via a Gaussian fit. Collecting all peak positions and performing a linear fit directly gives a value for α. This line is essentially the charge neutrality line, and moving along this line translates to changing the electric field only. Since the resistance has a minimum for vanishing electric field, the offsets $V_{B,0}$ and $V_{T,0}$ (cf. section 2.4.2) are determined by measuring the resistance with respect to bottom gate voltage and top gate voltage close to the lowest resistance peak. By fitting another Gaussian to the resistance values along the

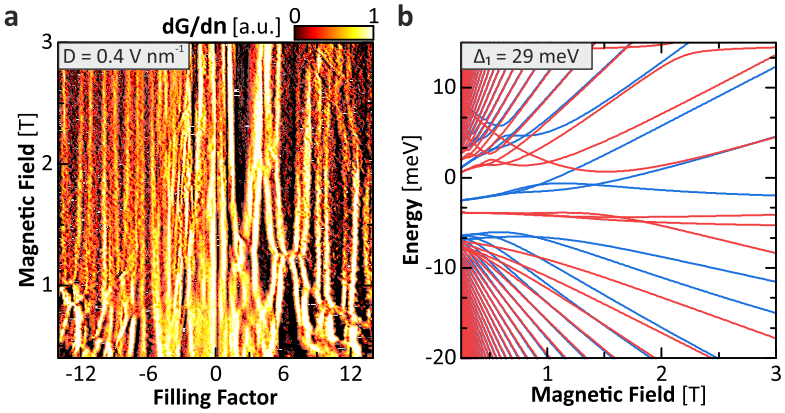

Figure 4.6 Magnetotransport at Intermediate Electric Fields: *(a) Derivative of the conductance with respect to filling factor and the magnetic field at an electric field of D = 400 mV nm^{-1}. Conductance plateaus are indicated by a vanishing conductance derivative. (b) Simulated evolution of spin-degenerate LLs at potential differences of Δ_1 = 29 meV stemming from the K (red) and K' (blue) valley as a function of the magnetic field. The value for Δ_1 corresponds to the electric fields in (a).*

charge neutrality line, the offsets $V_{B,0}$ and $V_{T,0}$ can be determined (see Figure 4.4b,c). The contact resistance and the gate capacitance of the bottom gate C_B are determined using the quantum Hall effect. A rough estimated of C_B is already given by geometrical considerations. Matching the position of conductance plateau to the theoretically expected values of $n = \nu eB/h$ yields the effective C_B. The contact resistance R_C can then be determined by matching the conductance G of the plateaus to the expected values of $G = \nu e^2/h$.

Magnetotransport at High Charge Carrier Densities

Figure 4.5 shows the derivative of the conductance with respect to charge carrier density and electric field for different magnetic fields together with the corresponding single-particle simulations. In the high-density regime, a characteristic sequence of Landau level crossings along parabola-like contours is apparent. From the low charge carrier density measurements (see Figure 4.2a,b), the interlayer potential difference Δ_1 could be related empirically to the electric field via $\Delta_1 = \alpha D$ with α = 0.073 e nm^{-1} assuming a linear relationship (see section 4.3). Using this relation, the experimental data show excellent agreement with single particle simulations further underlining the findings presented in the main text.

Magnetotransport at Intermediate Electric Field

For completeness, the magnetotransport data at intermediate electric field of D = 0.4 mV nm^{-1} together with the corresponding simulated evolution of Landau levels are shown in Figure 4.6. In contrast to the high-field measurements presented in Figure 4.3b, no clear indication of broken-

symmetry states is visible even at low magnetic fields.

5 Competition of Broken-Symmetry States in ABC Trilayer Graphene

Quasi-particles in graphene and its multilayer cousins have been shown to exhibit an unconventional quantum Hall effect due to their non-trivial Berry phase. Even in the absence of an external magnetic field, it has been predicted that interaction-induced symmetry breaking can give rise to several spontaneous quantum Hall states that exhibit non-zero spin, valley or charge Hall conductivities. Due to its diverging density of states at charge neutrality and its large Berry phase, rhombohedral trilayer graphene is especially susceptible to interaction-driven spontaneous symmetry breaking and, thus, a promising platform to explore the world of correlated states in two dimensions. In this chapter, light is shed onto the rich phase diagram of spontaneous broken-symmetry quantum Hall states by tracking their transport signature in suspended dual-gated rhombohedral trilayer graphene devices as a function of electric and magnetic fields. In particular, the presence of quantum Hall states with non-zero conductance is observed down to exceptionally low magnetic fields and their intrinsic orbital magnetic moment is confirmed via hysteresis measurements.

The results presented in this chapter are currently being prepared for publication. The scattering scanning near-field optical microscopy images have been made by F. R. Geisenhof. Furthermore, F. Zhang (University of Texas at Dallas, USA) provided the theoretical framework presented within this chapter. The experimental work as well as the data analysis was done as part of this thesis.

5.1 Introduction

Since the first isolation of bilayer graphene (BLG), continuing advances in device quality have facilitated the observation of a whole variety of fascinating correlated broken-symmetry states[17,27,28,104,106,148,149]. Its natural extension, rhombohedral multilayer graphene, is predicted to be even more susceptible to interaction-induced chiral symmetry breaking due to its flat low-energy bands[15,62,72,76,77] and giant Berry curvature[15,18,19]. Thus, together with the possibility to readily tune its properties with electric and magnetic fields[15], rhombohedral multilayer graphene is a viable platform to explore electron-electron interactions and exotic correlated ground states. So far, five competing spontaneous quantum Hall states as a consequence of the non-trivial Berry curvature have been proposed[18,19,150]. Among these, the quantum anomalous Hall (QAH) state and the “All”

state are particularly interesting as they are predicted to exhibit an intrinsic orbital magnetic moment and a non-zero charge Hall conductivity even in the absence of a magnetic field[18,19,150]. However, experimental studies of correlated states in rhombohedral graphene are sparse due to the necessity of excellent sample quality and homogeneity of the highly fragile rhombohedral stacking order[31,114]. Although recent studies provide strong evidence of the insulating layer antiferromagnetic (LAF) and quantum valley Hall (QVH) states in rhombohedral multilayer graphene[26,72,103,105], the presence of the remaining proposed spontaneous quantum Hall states still remains elusive. In this study, quantum transport in suspended dual-gated rhombohedral trilayer graphene (r-TLG) is investigated. The transport signatures of four of the five proposed spontaneous quantum Hall states are identified and light is shed onto the rich phase diagram at low electric and magnetic fields. Specifically, the presence of both the QAH and the "All" state are probed by tracking down their signatures to exceptionally low magnetic fields of less than 50 mT and revealing their intrinsic orbital magnetism.

5.2 Fabrication and Methods

The samples presented within this chapter have been prepared and identified as described in chapter 3. In brief, r-TLG flakes are exfoliated onto a Si wafer with a 300 nm SiO_2 layer and identified by optical microscopy, Raman spectroscopy and atomic force microscopy (AFM). Additionally, scattering scanning near-field optical microscopy (s-SNOM) is employed to ensure stacking order homogeneity down to nanometer scale and confirm the absence of any domain walls. Suspended dual-gated structures have been fabricated as follows: First, regions with homogenous stacking order were cut out using standard electron-beam lithography together with reactive-ion etching. Electrical contacts (5/100 nm Cr/Au), a spacer for the top gate (140 nm SiO_2) and the top gate (5/160 nm Cr/Au) were fabricated consecutively using electron-beam lithography. To decrease the contact resistance, contacts have been treated in a UV/Ozone environment for 1 min prior to metal evaporation. Subsequently, samples were submersed in buffered hydrofluoric acid to remove the SiO_2 spacer and 150 nm of the SiO_2 of the substrate. The devices were transferred to ethanol and dried in a critical point dryer to prevent collapse of the graphene devices. All measurements are performed in a dilution refrigerator system at temperatures below 10 mK (unless specified otherwise) using a standard lock-in measurement technique at an AC frequency of 78 Hz and currents of < 5 nA. Prior to any measurements, the devices were cleaned in-situ via current annealing. By adjusting the voltages V_B and V_T of the silicon back gate and the gold top gate respectively, both the charge carrier density $n = C_\mathrm{B}(\alpha \mathrm{V_T} + \mathrm{V_B})/e$ and the electric field $D = C_\mathrm{B}(\alpha \mathrm{V_T} - \mathrm{V_B})/2\varepsilon_0$ could be tuned independently[17]. Here, C_B is the capacitance per unit area of the bottom gate, α the ratio of top and bottom gate capacitances $\alpha = C_\mathrm{T}/C_\mathrm{B}$, e the electron charge and ε_0 the permittivity of vacuum. The calibration procedure is outlined in more detail in the appendix in

	$K\uparrow$	$K\downarrow$	$K'\uparrow$	$K'\downarrow$	*Orbital Moment*	*Charge Hall Conductivity*	*Net Layer Polarization*
QVH	T	T	T	T	No	0	Full
QAH	T	T	B	B	Yes	$6\ e^2/h$	No
LAF	T	B	T	B	No	0	No
QSH	T	B	B	T	No	0	No
ALL	T	T	T	B	Yes	$3\ e^2/h$	Partial

Table 5.1 Spontaneous Quantum Hall States in r-TLG: *Spin-valley layer polarization (T for top layer and B for bottom layer) together with further properties of the five proposed quantum Hall states, namely the quantum valley Hall (QVH) state, quantum anomalous Hall (QAH) states, layer-antiferromagnetic (LAF) state, quantum spin Hall (QSH) state and the "All" state that combines charge, valley and spin Hall effects. Adapted from Ref [18].*

section 5.5. The contact resistance R_C and the bottom gate capacitance were extracted from the quantum Hall plateaus at B = 3 T.

5.3 Experimental Results

In r-TLG, interlayer hopping dimerizes neighboring bulk sublattices sites driving them away from the Fermi energy and leaving only two sublattice sites on the outermost layers at low energies[15,64,72,73]. Thus, quasi-particles in r-TLG can be described by two-component spinors associated with the two low-energy sublattice sites (often referred to as pseudo-spin) leading to an effective two-band Hamiltonian[14,18,62]

$$H = \frac{(v_F p)^3}{\gamma_1^2}\left[\cos(3\xi\phi)\,\sigma_x + \sin(3\xi\phi)\,\sigma_y\right]. \tag{5.1}$$

Here, v_F is the Fermi velocity in graphene, γ_1 is the nearest-neighbor interlayer hopping energy, p is the momentum with $\phi = \tan^{-1} p_y/p_x$, $\xi = \pm 1$ labels the K and K' valleys and σ_i are the Pauli matrices acting on the pseudo-spin. Quasi-particles governed by this Hamiltonian have a pseudo-spin chirality of $J = 3$ and acquire a Berry phase of $\pm 3\pi$ when encircling the K or K' valley respectively[15,18,75]. This chiral symmetry is very robust with respect to higher order hopping terms, but can be broken explicitly by applying a perpendicular electric field or spontaneously by electron-electron interactions[18]. Indeed, due to the diverging density of states at charge neutrality, both perturbative renormalization group analysis[18,19,78] and previous experiments[26–28] suggest that rhombohedral graphene is very susceptible towards spontaneous chiral symmetry breaking. As a result, a gap opens in the electronic spectrum giving rise to a giant Berry curvature at the valley

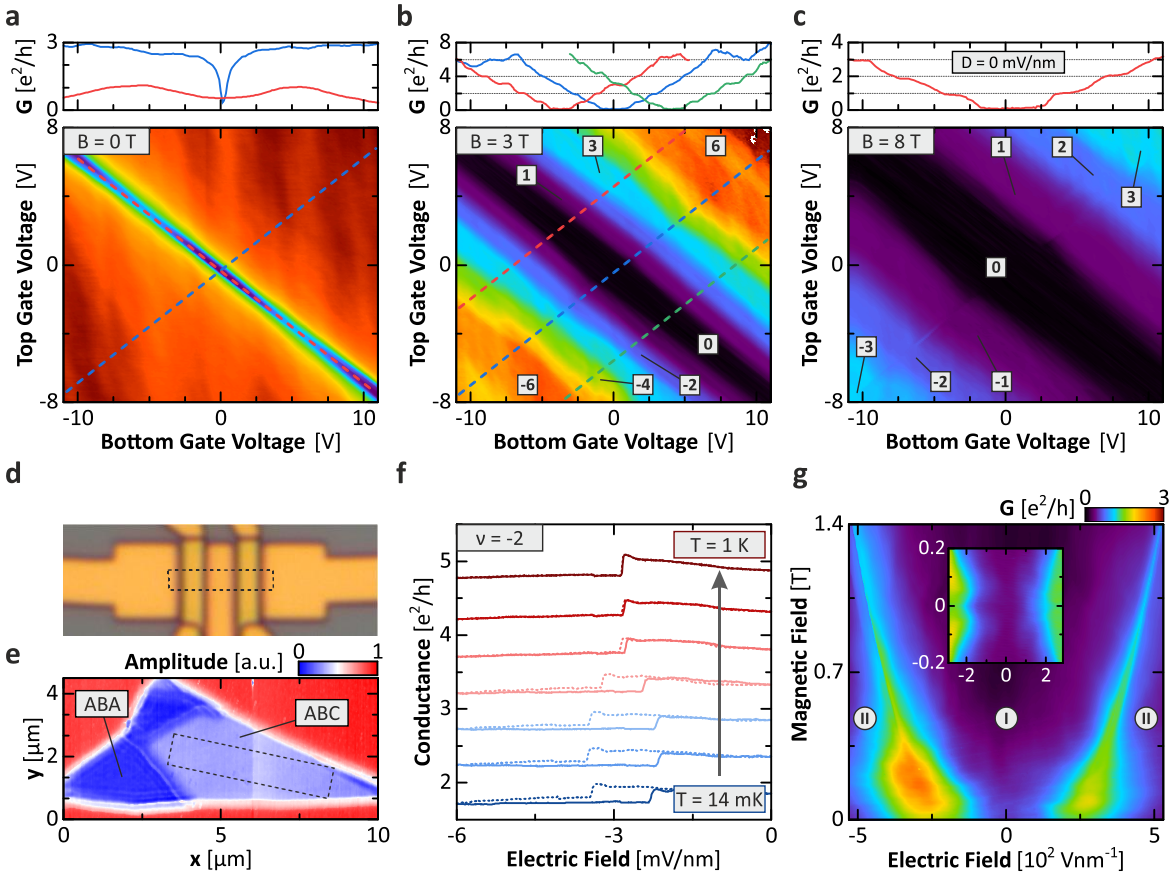

Figure 5.1 Microscopy and Magnetotransport: *(a-c) Differential conductance as a function of top gate voltage and bottom gate voltage at magnetic fields B = 0 T (a), B = 3 T (b) and B = 8 T (c). In (a), line cuts show the conductance at vanishing electric field (blue) and vanishing charge carrier density (red). In (b), line cuts show the conductance at constant electric fields of D = -20 mV nm^{-1} (green), D = 0 mV nm^{-1} (blue) and D = 20 mV nm^{-1} (red). In (c), the line cut shows the conductance at vanishing electric field. Landau levels (filling factors) are indicated by numerals. (d,e) Optical microscopy image (d) of a suspended dual-gated r-TLG sample (black contour) together with the corresponding s-SNOM image (e). The vertical line in the ABC region is a measurement artifact. (f) Temperature dependence of the forward and backward sweep in electric field across the line feature visible in (c). The lines are offset by 0.5 e^2/h with respect to each other for clarity and the temperatures are (from blue to red) 14 mK, 25 mK, 50 mK, 100 mK, 200 mK, 400mK and 1 K. (g) Differential conductance as a function of electric and magnetic fields at charge neutrality. The inset shows a zoom-in on zero magnetic and electric fields. The low conductance regions can be indentified with the LAF/CAF phase (I) and the QVH phase (II).*

centers[18,19]. Theoretically, this can be modelled by introducing an additional mass term in the Hamiltonian $H_{\text{int}} = H + m\sigma_z$[18,19,151]. Depending on its sign with respect to the spin-valley flavor, a family of five competing broken-symmetry states as summarized in Table 5.1 have been predicted:

The quantum valley Hall (QVH) state, the quantum anomalous Hall state (QAH), the layer antiferromagnetic state (LAF), the quantum spin Hall state (QSH) and the "All" state[18,19]. They can be distinguished by their respective Hall conductivities and orbital magnetic moments, a consequence of the non-trivial Berry curvature, as well as their layer polarization. Although these competing states are expected to be close in energy, their relative energies can be tuned by electric and magnetic fields. For instance, states exhibiting a layer polarization are favored in electric fields, while magnetic fields favor states with non-zero orbital moment.

First, Figure 5.1a-c shows the two-terminal differential conductance G as a function of the bottom and top gate voltage at magnetic fields of B = 0, 3, 8 T. Figure 5.1d,e shows an image of the device geometry and the corresponding scattering scanning near-field optical microscopy image that confirms the stacking order homogeneity of the sample (see also Figure 5.4 in the appendix). First, unexpected from single-particle simulation, the 12-fold degeneracy of the zeroth Landau level is already fully broken at B = 3 T and all plateaus at integer filling factors -6 ≤ ν ≤ 6 are well-resolved. This underscores the excellent device quality and hints towards the strong influence of interactions within the system. Surprisingly, a discontinuity along the zero electric field line is visible faintly at B = 3 T and very prominently at B = 8 T. The discontinuity is exceptionally sharp as revealed by additional high-resolution measurements close to zero electric field (see Figure 5.6 in the appendix). Since top and bottom layer are expected to exhibit different effective couplings to the electric contacts, this discontinuous jump in conductivity strongly hints towards the presence of layer-polarization in the integer quantum Hall states that reverses at zero electric field. The sharp transition is also in stark contrast to measurements in BLG, where the layer inversion extends over a broad layer-balanced transition region[17,27]. On the one hand, this indicates that layer-polarized states in r-TLG are favored at substantially lower electric fields than in BLG. On the other hand, the sharp transition also suggests that only a single domain is present within the sample in agreement with the s-SNOM data. To investigate the transition in more detail, several measurements sweeping across the transition line at different temperatures and constant charge carrier density are shown in Figure 5.1e. Notably, the transition displays a pronounced hysteresis that vanishes at temperatures above 400 mK. The reason for this behavior, however, remains unclear and will be investigated in further studies.

At zero magnetic field and high electric fields, in agreement with single-particle theory and previous experiments, the opening of a substantial band gap is apparent from the decrease in conductance (see line trace in Figure 5.1a). This also confirms the rhombohedral stacking order, as the opening of a band gap requires bulk states to be completely gaped out inconsistent with Bernal stacking[14,68,72]. However, unexpected from a single-particle picture, instead of monotonously increasing, the conductance drops again for small electric fields indicating the opening of a spontaneous gap. This is consistent with transport spectroscopy measurements on r-TLG that demonstrated to opening of a band gap at vanishing electric fields[26]. To examine this in more detail,

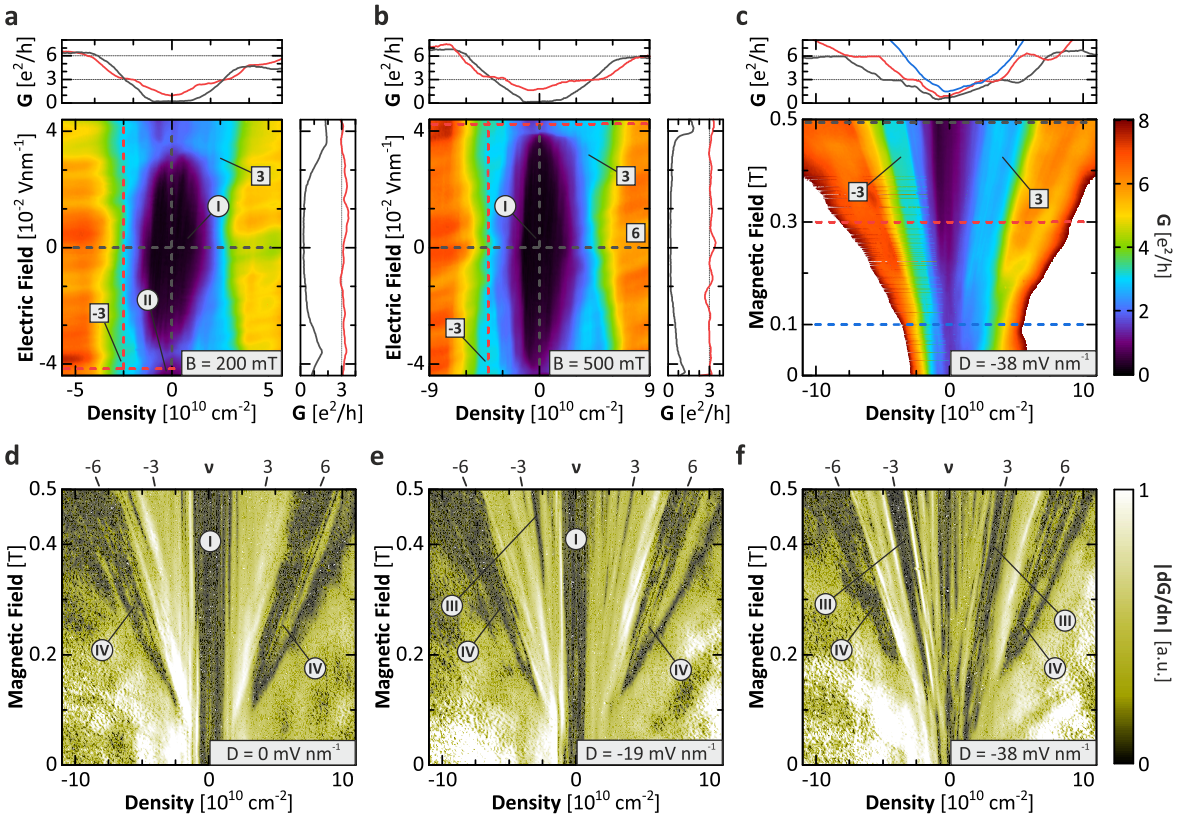

Figure 5.2 Magnetotransport at Low Magnetic Fields: *(a,b) Differential conductance as a function of charge carrier density and electric field at B = 200 mT (a) and B = 500 mT (b). (c) Fan diagram of the differential conductance at constant electric field D = -38 mV nm^{-1}. (d-f) Fan diagrams of the derivative of the conductance with respect to the charge carrier density at electric fields D = 0 mV nm^{-1} (d), D = -19 mV nm^{-1} (e) and D = -38 mV nm^{-1} (f). The filling factors and their corresponding slopes are indicated in the top row. The roman numerals indicate the associated spontaneous quantum Hall states, namely the LAF/CAF state (I), the QVH state (II), the "All" state (III) and the QAH state (IV).*

Figure 5.1g shows the conductance G as a function of perpendicular electric and magnetic fields at charge neutrality. It is apparent that the spontaneous phase is suppressed by electric fields, but stabilizes in high magnetic fields. This observation agrees very well with previous measurements[26,72,103,105] as well as theory[18,19,152] and allows identifying the insulating phase at vanishing electric fields with the spin-polarized LAF (I) phase (or canted anti-ferromagnetic phase (CAF) when considering the tilting of quasi-particle spins in an external magnetic field[18,26]). With increasing electric field, the layer-balanced CAF phase becomes increasingly unfavorable and the system transitions into the fully layer-polarized QVH phase (II). The crossover line between the CAF and QVH phases is marked by an increase in conductance and becomes linear for high magnetic fields. This observation is in excellent agreement with theoretical predictions[152–154] and previous measurements on BLG[17,28,104]. It is also worth noting, that the crossover line is very sharp, strongly

hinting towards the absence of an additional intermediate phase as proposed elsewhere[155]. Although there is strong evidence that the CAF phase extends down to zero magnetic field in BLG[28,156,157], other experiments suggest the presence of a third phase at low magnetic and electric fields[17,106]. Indeed, at low fields (see inset of Figure 5.1g), faint indication of a local conductance minimum at lines of constant electric field can be observed in all devices. Thus, it is worth examining the remaining spontaneous phases in more detail to shed light onto the yet unknown ground state a vanishing fields and charge carrier density.

Figure 5.2a,b shows the differential conductance as a function of charge carrier density and electric field at magnetic fields of 200 mT and 500 mT. Notably, distinct quantum Hall plateaus at ν = 0, ±3, ±6 together with several fainter plateaus at integer levels at ν = -1, -2, -4, -5 are readily identifiable even at these weak magnetic fields. The insulating ν = 0 plateau can again be identified with the CAF phase (I) that crosses over to the QVH phase (II) at high electric fields. In agreement with the previous observations, the crossover field shifts towards higher electric fields with increasing magnetic field. The observation of prominent plateaus at ν = ±6 and especially ν = ±3 at these low magnetic fields, however, is surprising. Remarkably, while the ν = ±6 state seems to be insensitive to the electric field, the ν = ±3 state stabilizes at finite electric fields only. To explore the behavior of these states with respect to the magnetic field more closely, fan diagrams down to zero magnetic have been recorded at various electric fields. Figure 5.2c shows the conductance as a function of charge carrier density and magnetic field (fan diagram) for a non-zero electric field. To enhance the visibility of the plateaus and the examine the electric field dependence, Figure 5.2d-f show fan diagrams of the derivative of the conductance with respect to the charge carrier density. Fan diagrams of an additional device are shown in the appendix in Figure 5.7. At vanishing electric field, the ν = ±3 states are absent and the ν = ±6 persists down to fields of approximately 100 mT. When increasing the electric field, the plateau at ν = ±3 becomes more and more distinct and reaches down to exceptionally low fields of less than 50 mT. It is also worth noting that in the vicinity of these states, several distinct lines with the same slope are visible. These conductance fluctuations originate from localized states and are indicative of the presence of an energy gap[106,158]. Overall, this is very suggestive of the presence of gapped broken-symmetry states with non-zero Hall conductivity. Comparing to theory, the observations align very well with the QAH (IV) and the “All” state (III) that are predicted to exhibit a charge Hall conductivity of 6 e^2/h and 3 e^2/h respectively (cf. Table 5.1). Since they are predicted to have a non-zero orbital momentum[18,19], both states are expected to be favored in external magnetic fields. It is also worth noting, that the “All” state is partially spin-, valley- and, in particular, layer-polarized[18,19]. Consequently, the ν = ±3 state is expected to be favored in electric fields consistent with the measurements.

In order to get more insight into the nature of the spontaneous Hall states and to examine their role in the competition for the ground state, the two-terminal conductance at various filling factors is tracked while sweeping the magnetic field through zero. Since both the QAH state and the “All”

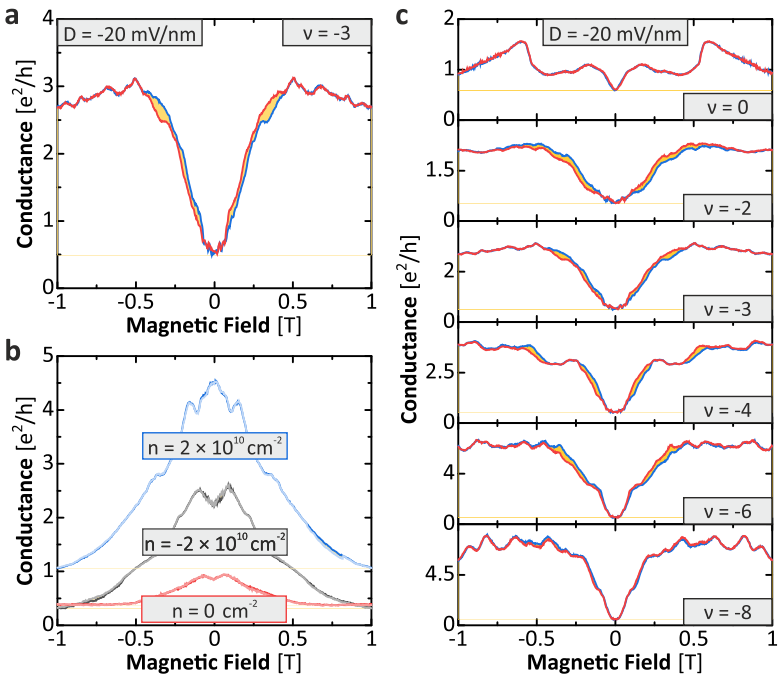

Figure 5.3 Hysteresis and Orbital Magnetic Moment: *(a) Conductance as a function of the magnetic field at constant electric field D = -20 mV nm^{-1} and filling factor ν = -3. The difference between forward (blue) and backward (red) sweep is indicated in yellow. (b) Conductance as a function of the magnetic field at constant electric field D = -20 mV nm^{-1} and charge carrier densities n = -2 × 10^{10} cm^{-2} (black), n = 0 cm^{-2} (red) and n = 2 × 10^{10} cm^{-2} (blue). Forward and backward sweeps are indicated in dark and bright colors respectively. (c). Sequence of hysteresis measurements at different filling factors ranging from ν = 0 to ν = -8 at constant electric field D = -20 mV nm^{-1}. The difference between forward (blue) and backward (red) sweep is indicated in yellow.*

state exhibit an orbital magnetic momentum, they are expected to display a hysteretic behavior of the longitudinal and Hall conductance when sweeping the magnetic field through zero[159–161]. The same is true for the two-terminal conduction that contains contributions from both conductances. It is also worth noting that while first indications of magnetic ordering in rhombohedral multilayer graphene have been observed previously, their connection to spontaneous Hall phases has not be explored so far[72,105]. Figure 5.3a,c shows the conductance as a function of magnetic field for both forward and backward sweeps at constant filling factors and finite electric field. For comparison, Figure 5.3b shows the conductance at constant charge carrier density and, thus, varying filling factor. It is also worth noting that in all cases, forward and reverse sweeps are mirror symmetric with respect to zero magnetic field. First, a noticeable hysteresis is apparent for filling factors close to the ν = -3 and the ν = -6 state, while it is absent for filling factors far away (for instance ν = 0 and ν = -8). Additionally, no hysteresis is noticeable when sweeping the charge carrier density and, thus, traversing through various filling factors. The hysteresis is very indicative of an orbital momentum

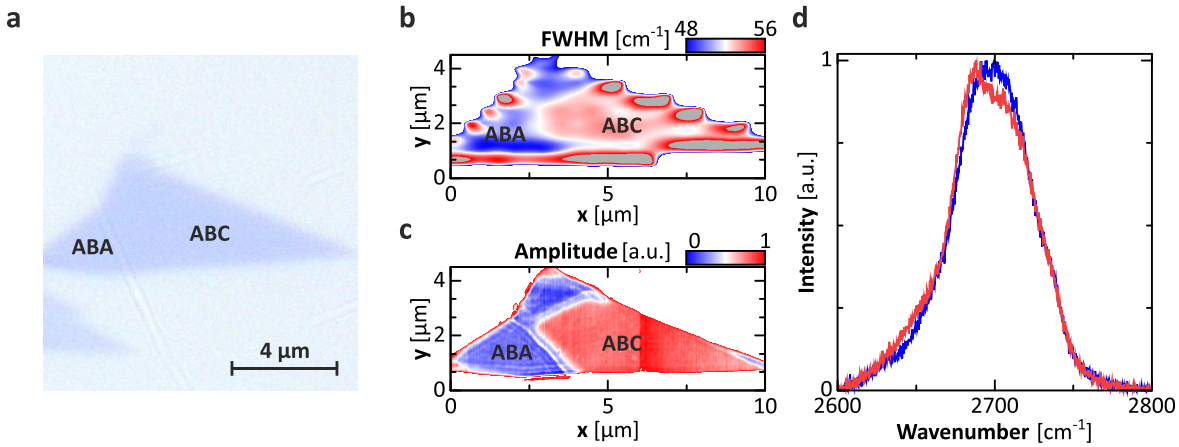

Figure 5.4 Trilayer Graphene Characterization: *(a) Optical microscope image of the graphene flake presented in the main text. (b,c) Raman spectroscopy map (b) and scattering scanning near-field optical microscopy (s-SNOM) map (c) of the trilayer graphene flake shown in (a). Two regions with different FWHM and s-SNOM amplitudes are readily visible and can be identified with ABA (blue) and ABC (red) stacking order. (d) Single Raman spectra of spots inside the ABA (blue) and ABC (red) regions as shown in (b,c).*

consistent with the presence of both QAH state and "All" state. However, the conductance drop at zero magnetic field strongly indicates that neither the QAH nor the "All" state provide percolating conductive edge states at zero magnetic field. This implies that both states lose the competition against the CAF or QVH state at vanishing magnetic fields. Yet, it has also been pointed out that current annealing induced disorder close to the contacts could prevent edge channels to couple to the electrical contacts obscuring the observation of a zero-field conductance[157]. Indeed, as we do observes a distinct hysteresis, it seems at least likely that the QAH state (at low electric fields) and "All" state (at high electric field) actually persist down to zero magnetic field, but cannot be accessed via two-terminal transport measurements. Thus, in order to definitely determine the ground state at vanishing fields and charge carrier density, further measurements that are able to directly probe the edge channels are necessary.

5.4 Conclusion

To conclude, in this study, transport measurements on suspended dual-gated r-TLG devices have been conducted to probe the phase diagram of spontaneous broken-symmetry quantum Hall states. At charge neutrality, transport measurements demonstrate the presence of the insulating LAF/CAF phase at low electric fields and the QVH phase at high electric fields. Furthermore, at filling factors of ν = ±3 and ν = ±6 and low magnetic fields, distinct quantum Hall plateaus indicate the presence of further spontaneous quantum Hall states with non-zero charge Hall conductivity. Together with

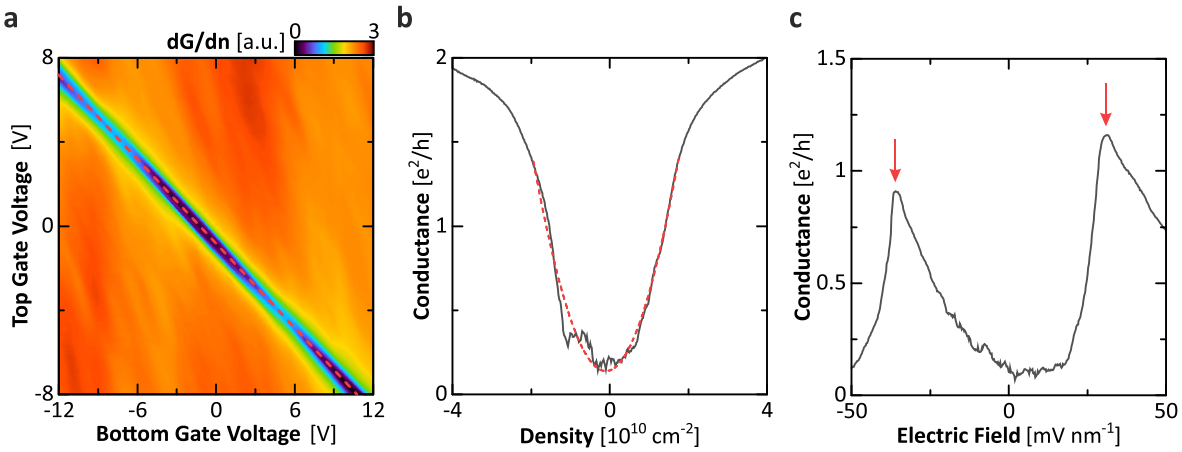

Figure 5.5 Calibration of Charge Carrier Density and Electric Field: *(a) Conductance as a function of the bottom gate and the top gate voltage. On every column of the plot, the resistance peak position is extracted by performing a Gaussian fit. Connecting all peak positions and fitting a line yields the charge neutrality line (dotted red). The top gate and bottom gate offset voltages can be extracted by correcting the center of Gaussian fit (dotted red) at the zero electric field line (b) and by correcting the mean position of the conductance peaks (red arrows) along the charge neutrality line (c).*

the hysteresis measurements that confirm the presence of an intrinsic orbital magnetic moment, the results are consistent with the QAH state at low electric fields and the "AII" state a high electric fields. At vanishing magnetic fields, however, signature of these states is lost and the LAF/CAF and QVH state seem to dominate depending on the electric field. This study is the first experimental demonstration of orbital magnetism in pure trilayer graphene and opens up possible applications in topological quantum computing applications[162].

5.5 Appendix and Supporting Information

In this section, further measurement and calibration data not shown within the discussion in section 5.3 is presented. The additional data supports the presented results and is shown for completeness and reference.

Identification and Characterization

In a first step, r-TLG is located and identified via optical microscopy. Figure 5.4a shows a microscope image of the sample presented in the main text. In order to reveal the stacking order as well as stacking faults and domain walls, a combination of Raman spectroscopy and scattering scanning near-field optical microscopy (s-SNOM) has been employed. Figure 5.4b,c shows as map of the FWHM of the 2D Raman peak and the s-SNOM amplitude respectively. Both maps exhibit two distinct regions with low and high FWHM as well as s-SNOM amplitude, with Figure 5.4d displaying

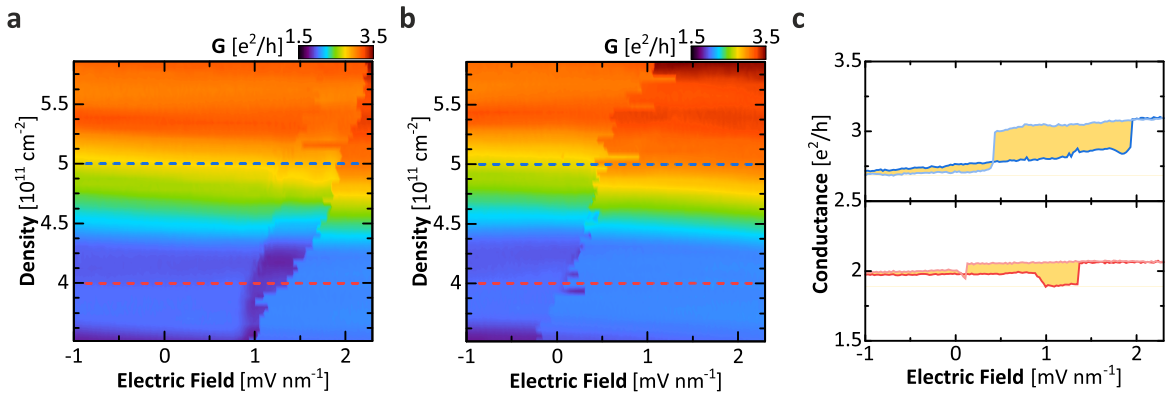

Figure 5.6 Inversions of the Layer Polarization: *Conductance as a function of electric field and charge carrier density for forward (a) and reverse (b) sweep of the electric field. The map was recorded at a magnetic field of 8 T. (c) Conductance along lines of constant density $n = 4 \times 10^{10}$ cm^{-2} ($\nu \approx 2.1$, red) and $n = 5 \times 10^{10}$ cm^{-2} ($\nu \approx 2.5$, blue) as indicated in (a,b). The forward and backward sweeps are indicated in dark and bright color respectively.*

the Raman spectra corresponding to these regions. Comparing the Raman spectra to previous calibration data and literature allows to identify the regions with Bernal (ABA) and rhombohedral (ABC) stacking order[114,127]. By matching the low-resolution Raman map to the regions of different amplitude in the s-SNOM image allows for resolving the stacking domains down to nanometer resolution and confirming the absence of stacking faults and domain walls[114]. In order to prevent transformation of stacking order, ribbons with homogeneous ABC stacking order have been etched out using reactive ion etching prior to defining electrical contacts[114].

Calibration of Dual Gate Transport

In order to transform the top gate voltage V_{T} and the bottom gate voltages V_{B} to electric field D and charge carrier density n (see section 4.2 and section 2.4.2), the conductance is mapped as a function of the bottom gate voltage and top gate voltage at zero magnetic field as shown in Figure 5.5a. In every line of constant top gate voltage, the center of the conductance dip is determined via a Gaussian fit. Collecting all peak positions and performing a linear fit directly yields a value for α as the inverse slope. This line fit is essentially the charge neutrality line, and moving along this line translates to changing the electric field only. To determine the offsets $V_{B,0}$ and $V_{T,0}$ (cf. section 2.4.2), the conductance is measured as a function of charge carrier density while setting the electric field and magnetic field to zero (see Figure 5.5b). The offsets $V_{B,0}$ and $V_{T,0}$ are selected in order to correct for the displacement of the Gaussian fit from zero charge carrier density. Consecutively, the conductance is measured as a function of electric field at charge neutrality and B = 0.4 T (see Figure 5.5c). Here, the offsets $V_{B,0}$ and $V_{T,0}$ are set such that the mean of the two peak positions is at zero field. This alignment has shown to yield the most reliable results and relates to the presence of two

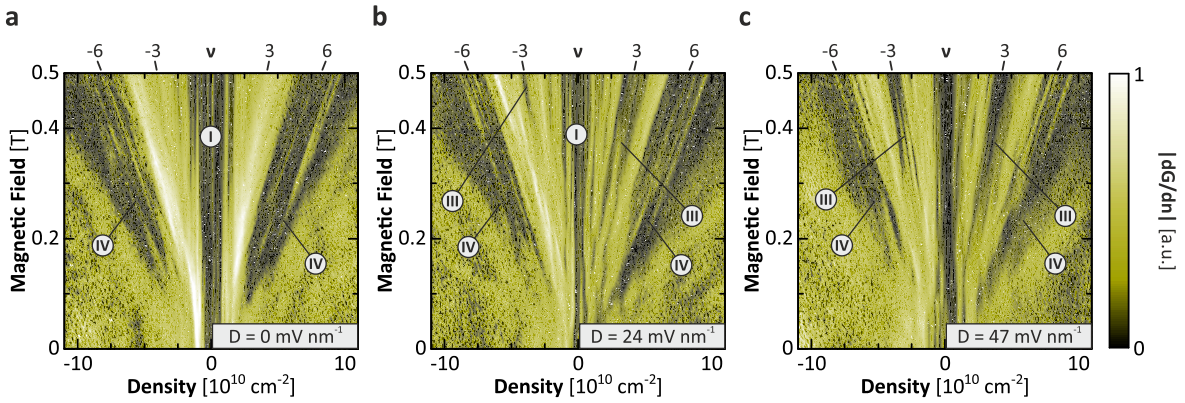

Figure 5.7 Fan Diagrams at Different Electric Fields: *(a-c) Fan diagrams of the conductance derivative with respect to the charge carrier density at D = 0 mV nm^{-1} (a), D = 24 mV nm^{-1} (b) and D = 47 mV nm^{-1} (c) for an additional device. The filling factors and their corresponding slope are indicated in the top row. The roman numerals indicate the associated spontaneous quantum Hall states, namely the LAF/CAF state (I), the "All" state (III) and the QAH state (IV).*

distinctive symmetric conductance peaks at non-zero magnetic and electric fields (see Figure 5.1g). This procedure is repeated with alternating sweeps of the charge carrier density and the electric field until $V_{B,0}$ and $V_{T,0}$ converge.

Inversion of the Layer Polarization

In order to further elucidate the nature of sudden jump in conductance close to the layer inversion, Figure 5.6 shows high-resolution measurements close to zero electric field. In agreement with the measurements shown in the main text, the discontinuity displays a hysteretic behavior. In addition, the jump in conductance is very sharp and happens within an electric field range of 50 µV nm^{-1} only. Surprisingly, the exact position of the transitions seem to vary stochastically between individual lines of constant charge carrier density. It is also worth noting, that the shift of the transition line with respect to zero electric field lies within the error margin of the electric field calibration.

Additional Magnetotransport Data

Figure 5.7 shows further fan diagrams of an additional device confirming the emergence of strong a conductance plateaus at ν = ±6 at vanishing electric field and ν = ±3 at high electric field.

6 Charge Traps in Perovskite Nanowire Field-Effect Transistors

All-inorganic halide perovskites have recently emerged as outstanding materials for optoelectronic applications. However, although critical for developing novel technologies, the charge transport mechanisms and the influence of charge traps in all-inorganic systems still remain elusive. In this chapter, the charge transport properties of $CsPbBr_3$ nanowire films are probed by employing a field-effect transistor geometry. Field effect mobilities of μ_{FET} = 0.004 cm^{-2} V^{-1} s^{-1} and photoresponsivities in the range of R = 31 A W^{-1} are demonstrated. Furthermore, to explore defect states in more detail, charge transport both with and without illumination is investigated down to cryogenic temperatures. Without illumination, the measurements reveal that deep traps dominate transport and the mobility freezes out completely at low temperatures. Despite the presence of deep traps, the field effect mobility increases by several orders of magnitude when illuminating the sample and phonon-limited transport characteristics are visible. This property can be seen as an extension to the notion of "defect tolerance" of perovskite materials that has solely been associated with shallow traps so far. Furthermore, the findings provide further insights into charge transport in perovskite materials and underline that managing deep traps can open up a route to optimizing optoelectronic devices such as solar cells or phototransistors operable also at low light intensities.

The results presented in this chapter have been submitted as "Charge Traps in All-Inorganic $CsPbBr_3$ Perovskite Nanowire Field-Effect Phototransistors" by F. Winterer, L. S. Walter, J. Lenz, S. Seebauer, Y. Tong, L. Polavarapu and R. T. Weitz. The perovskite nanowire films were synthesized, prepared and spectroscopically characterized by Y. Tong and L. Polavarapu. All electrical measurements as well as data analysis were done as part of this thesis.

6.1 Introduction

Halide perovskite materials are a promising new class of semiconductor materials for optoelectronic applications owing to their attractive optical and electronic properties such as high absorption coefficients[36,37] and long charge carrier lifetime[38], together with ease of fabrication, solution processability and low cost[39]. They have shown great promise and potential in various applications such as solar cells[38,163], photodetectors[46,164,165], field effect transistors (FETs)[166–169] and lasers[45].

However, the performance of halide perovskite devices is often limited by insufficient stability and moderate crystallinity. In the last years, significant advance has been achieved by the extension of perovskite materials into (all-inorganic) colloidal nanocrystals (NCs)[39]. The shape and composition of perovskite NCs are easily controllable and a wide range of morphologies have been synthesized[39–43]. Among all, especially perovskite nanowires (NWs) show great promise for high performance optoelectronic devices such as lasers and photodetectors[44–46]. However, to exploit the full potential of halide perovskite materials, profound understanding of the microscopic transport mechanisms is prerequisite. For example, a better understanding of the influence of charge traps and the often cited "defect tolerance"[47–51] of perovskite materials can provide crucial information for optimizing charge generation and transfer in perovskite solar cells[49]. Here, FETs are a versatile platform to investigate charge transport in semiconductor materials. Unlike in solar cells, the FET geometry allows to explore the influence of traps on charge carrier mobility both with and without illumination. Starting from the pioneering work on layered hybrid tin halide perovskites[170] to experiments on methylamonium lead halide perovskites (MALHs)[166–168,171,172] to all-inorganic perovskite FETs[169,173–175], several studies aiming to unveil transport mechanisms in perovskite materials have been conducted. Yet, especially for inorganic or NC-based materials, thorough studies of transport mechanisms and the influence of traps are still lacking.

In this work, CsPbBr3 nanowire phototransistors are fabricated and their temperature dependent transport properties both in the dark and under illumination are investigated down to cryogenic temperatures. Field effect mobilities of μ_{FET} = 0.004 cm^{-2} V^{-1} s^{-1} and photocurrent responsivities R = 31 A W^{-1} at a power density of 3.9 mW cm^{-2} are demonstrated at room temperature. Furthermore, temperature dependent measurements enabled the determination of both depth and density of deep and shallow traps in the system. Surprisingly, investigating the gate-dependent photoconductivity revealed metal-like transport characteristics even in the presence of an appreciable density of deep traps. This intriguing observation again underlines the notion of "defect tolerance" in perovskite systems and even extends it to deep traps.

6.2 Fabrication and Methods

Synthesis of $CsPbBr_3$ Nanowires: The synthesis was carried out following the previously reported ultrasonication approach[41]. In a typical synthesis, 1-octadecene (10 mL), oleylamine (0.5 mL), and oleic acid (0.5 mL) were sequentially added to a mixture of Cs_2CO_3 (0.1 mmol) and $PbBr_2$ (0.3 mmol) precursor powders and then subjected to tip-sonication (Sonoplus HD 3100, Bandelin) at a power of 30 W for 60 min. The color of the reaction medium gradually turns into yellow during the course of the reaction. The resultant colloidal solution was centrifuged at a speed of 5000 rpm for 10 min. Then, the obtained sediment was dispersed in hexane (10 mL) under mild sonication. The centrifugation process was repeated thrice at a speed of 3000 rpm for 10 min. During this

centrifugation process, the nanocubes present in the product separate from the NWs. At last, the sediment containing $CsPbBr_3$ NWs was dispersed in hexane (5 mL), which was used for the fabrication of devices. The optical properties of the as prepared colloidal solutions were characterized by UV-VIS absorption (Cary60, Agilent Technologies) and photoluminescence (Varian Cary Eclipse, Agilent Technologies). The morphology of the obtained nanocrystals was characterized using a transmission electron microscope (TEM) operating at an accelerating voltage of 80 – 100 kV (JEM-1011, JEOL). The high-resolution high-angle annular dark field images (HAADF-STEM) were acquired using a scanning transmission electron microscope (Titan, FEI) operating at 300 kV.

Device Fabrication: For FET device fabrication, p-doped Si wafers with a 100 nm SiO_2 layer were used as substrates. First, the substrates were immersed in Acetone and put into a sonicator for 3 mins. After that, the substrates were plasma cleaned in O_2 plasma for 3 min (PICO Plasma Cleaner, Diener). The colloidal solution of $CsPbBr_3$ nanowires was spin coated onto the substrates at 1500 rpm for 1 min. Then, contact pads with a 0.3 nm titanium adhesion layer and a gold layer of 70 nm were evaporated on top of the perovskite film using a standard electron beam evaporation technique together with a shadow mask. The gold pads functioned as drain and source contacts, while the silicon substrate was used as a back gate. Topography measurements were taken with an atomic force microscope (Dimension 3100, Bruker) in tapping mode. The thickness of the perovskite film was determined by measuring the step height of a scratch through the film.

Electrical Measurements: All electrical measurements were performed in a vacuum setup (CRX-VF Probe Station, Lakeshore) at $p < 5 \times 10^{-7}$ mbar (see also section 3.3.2). Furthermore, the sample stage was thermally coupled to a helium pulse-tube refrigerator enabling measurements at a variable temperature in the range between 8 K and 300 K. Two source-measure units (2450 SourceMeter, Keithley) were used to apply drain and gate voltages as well as to measure the respective currents. To investigate the photoresponse, a halogen lamp (Model 21AC, Techniquip) attached to the microscope of the probe station was employed. Wavelength dependent measurements were conducted using two different laserdiods with a wavelength of 650 nm (532 nm) and a total power of 650 µW (548 µW).

6.3 Experimental Results

The colloidal CsPbBr3 NWs were prepared by a ligand-assisted ultrasonication approach (see section 6.2). The UV-visible absorption and photoluminescence (PL) spectra of $CsPbBr_3$ NWs are depicted in Figure 6.1a. The prepared CsPbBr3 NWs exhibit an excitonic absorption peak at 513 nm and PL peak at 525 nm. The colloidal solution of NWs emits intense green emission under UV illumination (inset of Figure 6.1a). Transmission electron microscope (TEM) analysis of the NWs shows that they have a diameter of 12 nm and length ranging from 0.5 µm to 2 µm (Figure 6.1b). The NWs are single crystalline as revealed by high-angle annular dark-field scanning transmission electron microscopy

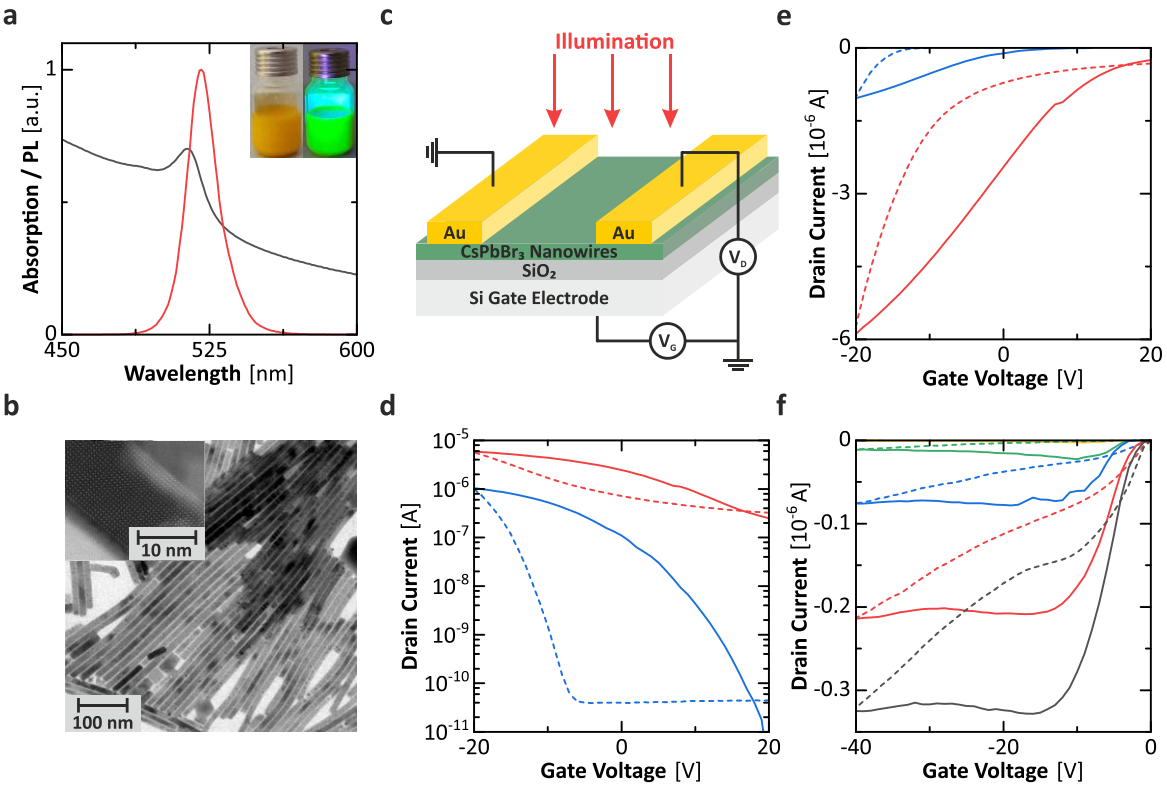

Figure 6.1 Spectroscopy and Field-Effect Transistor Characteristics: *(a) UV-visible extinction (black) and photoluminescence (red) spectra of the colloidal $CsPbBr_3$ NWs. The inset shows images of the colloidal solutions of $CsPbBr_3$ NWs under white light (left) and UV illumination (right).(b) Bright-field TEM image and HAADF-STEM image (inset) of the $CsPbBr_3$ NWs. (c) Schematic of the device architecture. The p-doped Si substrate acts as a back gate, while the two gold pads serve as drain and source electrodes. The perovskite and the gate are separated by a SiO_2 dielectric. (d,e) Transfer curves at V_D = -20 V with illumination (red) and without (blue) in logarithmic (d) and linear (e) scaling. The solid lines show the forward sweep and the dotted lines the backward sweep. (f) Output curves without illumination. Gate voltages range from V_G = 0 V (yellow) to V_G = -40 V (black) in increments of 10 V. The solid lines represent the forward sweeps and the dotted lines the backward sweeps.*

(HAADF-STEM) analysis (inset of Figure 6.1b). To analyze electrical transport properties of the $CsPbBr_3$ nanowire thin films, the perovskite nanowire solution was spin coated onto a Si/SiO2 substrate and bottom gate top-contact FET devices were fabricated (see section 6.2 for fabrication details). Figure 6.1c shows the schematic illustration of the device architecture. In the following, the data of three devices on one exemplary sample (sample A) is presented. Data of further devices and samples is shown in the appendix (see Table 6.1 for a sample overview). The layer thickness of the nanowire film was measured to be 530 nm thick with an RMS roughness of about 60 nm (see Figure 6.4 for more details on the topology of the sample). Thus, the electrical measurements can be seen as an ensemble average over many nanowires. All electrical measurements were taken in vacuum

below 5 × 10^{-7} mbar. Measurements in bright illumination conditions were done by illuminating the sample with a broadband halogen lamp with a power density of 3.9 mW cm^{-2}. First, transfer curves for several FET devices with a constant drain voltage of V_D = -20 V and gate voltages V_G ranging from -20 V to +20 V in both dark and bright illumination conditions were recorded. Figure 6.1d,e show the transfer curves of one exemplary device both with and without illumination. Other devices qualitatively show the same behavior (see Figure 6.5). Additionally, Figure 1f shows the output curves of the device for drain voltages up to V_D = -40 V. Without illumination, transfer and output curves show a clearly visible field-effect with a current modulation over several orders of magnitude. The devices show a distinct p-type semiconducting behavior, where only hole conduction is present and can be modulated with the gate voltage. Electron transport, on the other hand, is completely suppressed throughout the entire accessible gate range. The absence of electron transport has already been seen in other $CsPbBr_3$ samples[173–175], whereas in some $CsPbBr_3$ devices ambipolar transport was observed[169]. These inconsistent observations can be explained by varying trap concentrations in the respective samples caused by different growth conditions[47,176,177]. A high density of traps close to the valence band, for example, can lead to a shift of the electron conductivity onset to high positive voltages exceeding the accessible gate range. Such traps can be associated with vacancies of Cs and Pb that have particularly low formation energies in Br-rich growth conditions[47,49]. Beside the p-type conductivity, both output and transfer curves display a pronounced “clockwise” hysteresis between forward and reverse sweeps. This strong hysteresis is very common for perovskite materials and has been broadly reported for perovskite FETs and solar cells, even for single crystal samples[166–169,171–174,178]. Possible explanations for the hysteresis include ion migration, ferroelectricity, trap states in the material and surface traps at the interface to the dielectric[167–169,171–174]. Although there is still much debate on the microscopic cause of hysteresis, screening of the gate potential due to mobile ions has been widely regarded as the dominant mechanism at room temperature[168,169,171,174,179]. However, also traps at the dielectric interface can give rise to substantial hysteresis[180]. Ferroelectricity, on the other hand, showed only minor influence on electrical transport[168,179,181]. At low temperatures, ion migration is expected to be suppressed due to high activation energies[168,169,171,174,179,182–184] and interface traps are widely believed to become the dominant mechanism leading to hysteresis[168,169,171,179]. As temperature dependent measurement can help to shed more light onto the causes of hysteresis, this discussion will be revisited later. Based on the output and transfer curves, the FET mobility in the saturation regime can be calculated to be μ_{FET}^{Dark} = 0.004 $cm^2\ V^{-1}\ s^{-1}$ at room temperature for the best device (see section 6.5 and Figure 6.6 for more details). In this calculation, only the forward sweep was used, as the reverse sweep tends to yield unreliable results due to the strong hysteresis effect[168]. In other $CsPbBr_3$ systems, higher FET mobilities with record values of up to 2.2 $cm^2\ V^{-1}\ s^{-1}$ at room temperature have been reported[169,174,175,185]. However, even these record mobilities are still well below what has been expected from time-resolved photoluminescence measurements[165,186],

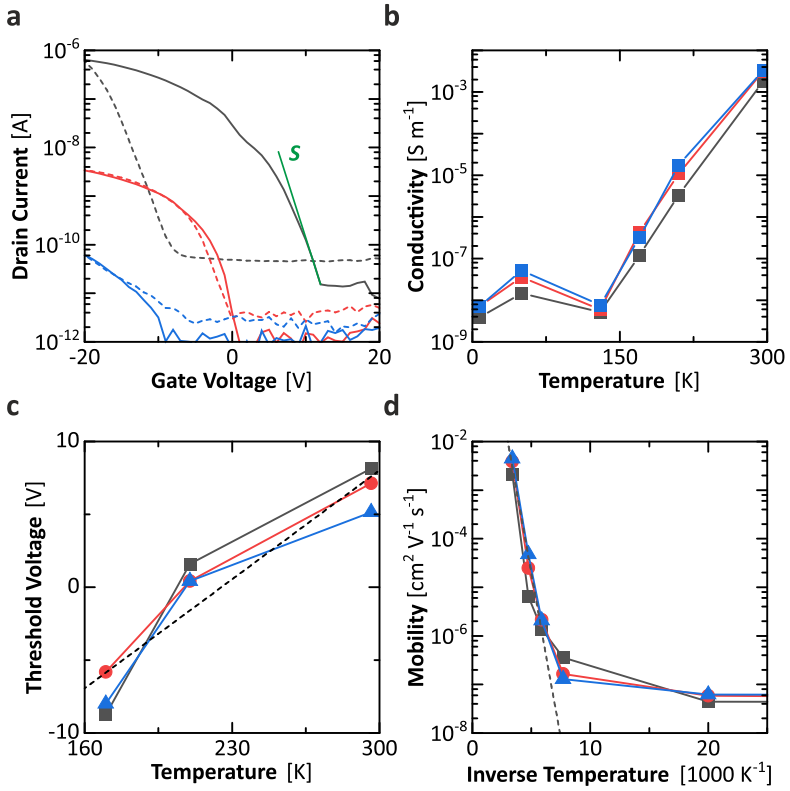

Figure 6.2 Temperature Dependent Transport Without Illumination: *(a) Transfer curves at temperatures T = 296 K (black), T = 210 K (red) and T = 170 K (blue) at a drain voltage of V_D = -20 V. The solid lines show the forward, and the dotted lines the backward sweep. The determination of the subthreshold swing S is indicated by a green line. (b) Maximum conductivity of three different devices (black, red and blue) as a function of temperature. (c) Threshold voltage of three different devices (black, red and blue) as a function of temperature. The linear fit to the data points is represented by the black dotted line. (d) Arrhenius plot of the mobility of three different devices (black, red and blue) with respect to the inverse temperature. The exponential fit to the first data points is shown as a black dotted line. The lower limit of the mobility at lower temperatures is due to limitations of the measurement system.*

acousto-optoelectronic spectroscopy[187], Hall-effect measurements[182,188] and THz spectroscopy[189]. Thus, a better understanding of the underlying transport mechanisms bears great potential for optimizing mobilities of all-inorganic perovskite devices.

A distinctly different behavior can be observed when illuminating the sample with a halogen lamp. As shown in Figure 6.1d, when switching on the illumination, the drain current increases significantly by up to four orders of magnitude. Since there is still a field effect present, the charge carrier mobility can be obtained similarly to the dark case. For our best device, the mobility of the illuminated device is $\mu_{FET}^{Bright} = 0.018\ cm^2\ V^{-1}\ s^{-1}$. The increase of mobility during illumination is consistent with observations on other perovskite devices[169,174]. In general, the strong

photoconductivity is directly connected to the combination of excellent optical absorption characteristics and efficient charge transport properties of perovskite materials[37,38,48]. Due to the high absorption coefficient, photo-excited charge carriers are generated very efficiently[38]. At the same time, fast exciton dissociation[36,37,190] as a result of the low exciton binding energies[36,48,190] leads to a high population of free charge carriers[36,37,191]. These free carriers can then contribute to the transport through the material and enhance the conductivity irrespective of the gate voltage[164,169,192]. This phenomenon is known as the photoconductive effect and leads to a vertical shift of the transfer curves to higher drain currents[164,169,192]. The quasi-additive behavior of a constant photocurrent onto a gate-tunable current[192] agrees very well with the measurement. Notably, the emergence of the photoconductive effect also implies that both mobile holes and mobile electrons are present in the system. This is very surprising, as electrons were completely immobilized in local trap states in the dark and only holes were mobile. Furthermore, photocurrent is suppressed by more than one order of magnitude when illuminating the sample with light at excitation energies below the band gap (1.91 eV) compared to above the band gap (2.33 eV). Thus, charge carriers are indeed photoexcited within the material rather than at the contacts or nanowire interfaces. The transfer curves also allow for calculating the photoresponsivity R (drain current increase per illumination power) of the devices[164,192]. For the best device, photoresponsivities of R = 31 A W^{-1} upon broadband white light illumination with a power density of 3.9 mW cm^{-2} were achieved. This compares very well even to single crystal $CsPbBr_3$ samples with responsivities of up to several hundred A W^{-1} at comparable power densities[46,165,169,193].

In order to investigate the influence of traps in more detail, the electrical transport properties of the $CsPbBr_3$ nanowires were measured as a function of temperature. At multiple temperature steps between 296 K and 8 K, transfer curves for both dark and bright illumination conditions were obtained. Figure 6.2 and Figure 6.3 show the transport characteristics at various temperatures without and with illumination respectively. First, it can readily be seen that without illumination, both conductivity and mobility decrease substantially with decreasing temperature. This mobility freeze-out indicates a thermally activated behavior originating from charge traps in the material[109,113,194,195] or Schottky barriers at the electrode-perovskite interface.[194–196] In general, Schottky barriers emerge due to the energy mismatch of valence and conduction band to the work function of the electrodes. Although the theoretical mismatch between the valence band of $CsPbBr_3$ and the work function of gold is in the range of 0.65 eV[169,197,198], efficient injection of electrons and holes with gold electrodes has been demonstrated in previous experiments[169]. Additionally, the weak dependence of the conductivity on temperature in illuminated samples indicates that charge transport is dominated by charge traps rather than barrier physics. At this point, it is also worth discussing further mechanisms that could potentially influence temperature dependent transport properties, namely ion migration and perovskite phase transitions. First, as mentioned earlier, mobile ions can effectively screen the gate potential and, thus, lead to hysteresis[168,169,171,174,179].

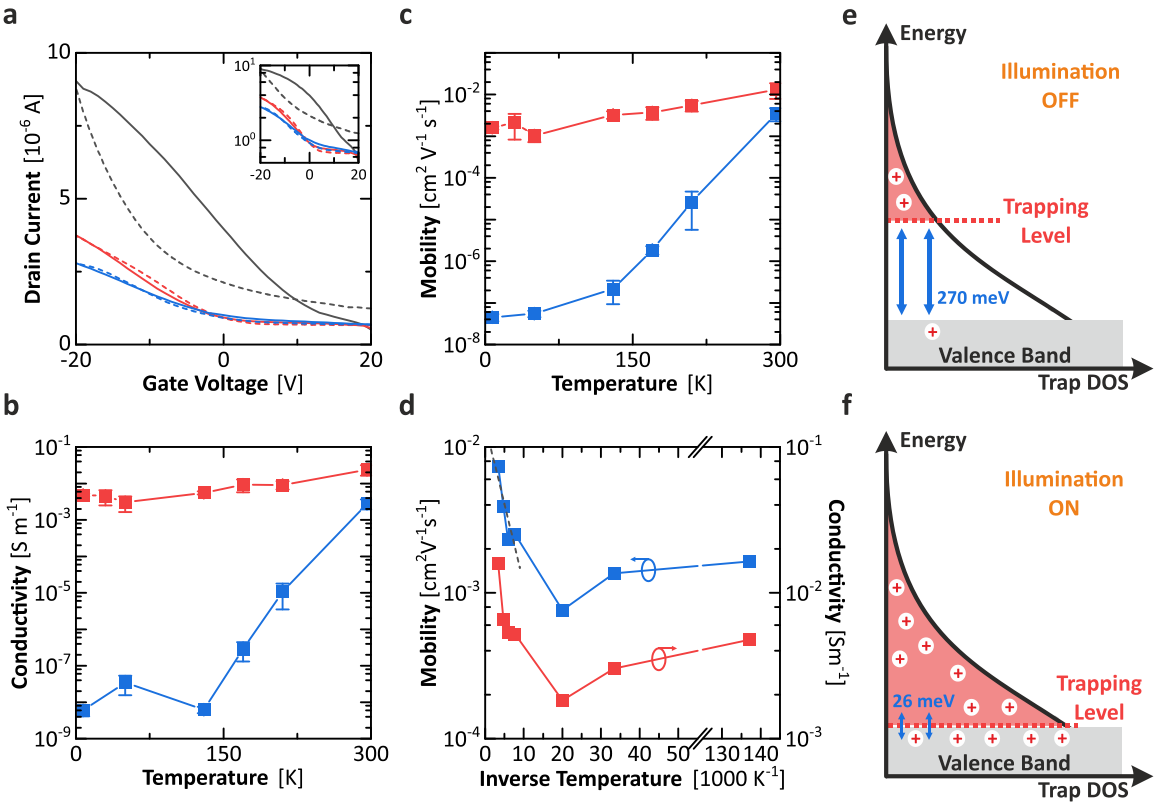

Figure 6.3 Temperature Dependent Transport in Illuminated Devices: *(a) Transfer curve in linear and logarithmic (inset) scaling for temperatures T = 296 K (black), T = 210 K (red) and T = 8 K (blue). The solid lines represent the forward, and the dotted lines the backward sweep. (b) Comparison of the conductivity with illumination (red) and without (blue) with respect to the temperature averaged over three different devices. The gate voltage was set to V_G = -20 V. (c) Comparison of the mobility with illumination (red) and without (blue) with respect to the temperature averaged over three different devices. (d) Comparison of mobility and conductivity with illumination with respect to the inverse temperature. The fit of the Arrhenius relation to the mobility is shown as a black dotted line. (e,f) Schematic trap density of states with the trap filling level (red) for dark (e) and illuminated (f) samples. In the dark, only deep traps are filled and transport is dominated by thermally activated behaviour with a high activation energy. In illuminated samples, almost all traps are filled and only shallow traps influence charge transport.*

When decreasing the temperature, ion migration is expected to freeze out and the hysteresis is suppressed[168,174]. In our devices, almost no hysteresis is visible in the transfer curves at 210 K (see Figure 6.2a). Thus, ion migration cannot explain the observed mobility suppression and can be neglected for temperatures $T \leq 210$ K[168,174,182]. The same is true for interfacial traps at the dielectric, that would lead to a similar hysteretic behavior[180]. Second, MALH systems are subject to a structural phase transition from orthorhombic to tetragonal crystal structure at around T_C = 160 K that can significantly alter electronic properties of the system[167,171]. However, the phase transition

temperature of $CsPbBr_3$ is well above room temperature, namely at T = 361 K from orthorhombic to tetragonal and at T = 404 K to cubic crystal structure[199,200]. Therefore, a phase transition is not present in the investigated temperature range.

In the following, properties of the charge traps are investigated in more detail and light is shed onto the often cited "defect tolerance" of perovskites[47,49]. In this context, it is very instructive to distinguish between shallow traps close to the band edge ($\Delta E \approx k_B T$) and deep traps far away from the band edge ($\Delta E \gg k_B T$)[49,113]. First, the trap density of deep traps can be estimated from the subthreshold swing S of the transfer curves using the formulas[113,169,201]

$$S = \frac{\mathrm{d}V_{GS}}{\mathrm{d}(\log I_{SD})} \qquad \text{and} \qquad N_{DT} = \left(\frac{C}{e}\right)\left(\frac{eS}{k_B T \ln 10} - 1\right) \tag{6.1}$$

where e is the elementary charge, k_B the Boltzmann constant, T the temperature and C the gate dielectric capacitance per unit area. An illustration of the subthreshold swing determination is shown in Figure 6.2a. This yields an average deep trap density of N_{DT} = 7 × 10^{12} cm^{-2} eV^{-1} at room temperature. This trap density is smaller than trap densities reported in literature even for single crystal samples[50,169]. As the Fermi level is still far away from the band edge in the subthreshold regime, the density N_{DT} can be associated with deep trap states (DT)[113]. The density N_{ST} of shallow trap states (ST) closer to the band edge can be estimated from the dependence of the threshold voltage on the temperature using[113,201]

$$N_{ST} = \left(\frac{C}{e k_B}\right)\frac{\mathrm{d}V_{th}}{\mathrm{d}T}. \tag{6.2}$$

This gives a trap density of N_{ST} = 3 × 10^{14} cm^{-2} eV^{-1} in our system. Figure 6.2c shows the calculated threshold voltages with respect to the temperature together with the line fit used to determine N_{ST}. With the gate voltage, a maximum charge carrier density of n_{Gate} = 4 × 10^{12} cm^{-2} can be induced. Thus, the gate is very likely not sufficient to fill even the deep traps in the system and transport is expected to be trap dominated. This is consistent with the distinct thermally activated behavior of the mobility as shown in Figure 6.2d and Figure 6.3d. Fitting an Arrhenius relation $\mu \approx \exp(-E_A/k_B T)$ to the temperature dependence of the mobility yields an approximate measure of the trap depth[109,113,195,201]. In the dark and for temperatures above T ≥ 170 K, the fit reveals a surprisingly deep trap depth (activation energy) of E_A = 270 ± 16 meV. This is in good agreement with other measurements[50] and fits well to the theoretically expected trap depth of Cs and Pb vacancies inside the crystal lattice in the range of 200 meV[47,49]. Measurements on an additional sample are qualitatively consistent with these results, but yield larger trap depths hinting towards the presence of further point defects (see section 6.5 and Figure 6.7). It is also worth noting, that these traps could also be located at the grain boundary between individual nanowires. Within the scope of these

measurements, it is not possible to pinpoint neither the origin nor the location of these traps. Yet, measurements on single crystal samples show comparable or even higher values for N_{DT}, which could hint towards an intrinsic origin of the traps[169].

However, even in the presence of these substantial trap densities, the conductivity of the devices increase several orders of magnitude when illuminating the sample even at cryogenic temperatures (cf. Figure 6.3a,b). Notably, at low temperatures the conductivity even increases slowly with decreasing temperature. This peculiar behavior has also been seen in MALH system[202–204] and has led to an ongoing debate on its underlying mechanisms. Here, it is worth noting, that this change in the slope of the temperature dependence is not related to a phase transition temperature, even in MALH systems[203,204] In general, the photoconductivity depends on the absorption of the material, the mobility and the charge carrier recombination rate[203,204]. However, some authors have argued, that charge carrier mobility variations are most probably the dominating parameter in this relation, although they were not able to measure the mobility directly[203,204]. The FET geometry employed within this study, however, allows for directly accessing the mobility in addition to the conductance. Figure 6.3c shows the mobility and Figure 6.3d shows a comparison of conductivity and mobility with respect to the (inverse) temperature. Additional data of further devices is shown in Figure 6.7 and Figure 6.8. As proposed by several authors[203,204], the mobility indeed nicely mimics the photoconductivity behavior. In the low temperature regime, similar to the conductivity, the mobility increases with decreasing temperature. Such a behavior is a sign of charge carriers travelling in delocalized metal-like band states, where the mobility is limited by phonon scattering[203,204]. This transition from "semiconducting" to "metal-like" behavior is very surprising, especially given the existence of a high density of deep traps at that completely hindered transport in the dark. At higher temperatures, the mobility shows thermally activated behavior. By again using an Arrhenius relation for modelling the mobility $\mu \approx \exp(-E_A/k_B T)$, the activation energy can be calculated to be E_A = 26 ± 5 meV. The activation energy of the illuminated sample is significantly lower than in the dark. Thus, at high temperatures, only shallow traps with a low activation energy influence charge transport. Besides, also excitons could be responsible for the thermally activated transport behavior. Their theoretically expected and measured binding energy of E_B = 47 meV[48,205,206] is in fair agreement with the thermal activation energy.

Figure 6.7e,f combines these results and shows an illustration of proposed transport mechanisms and energy landscape of the charge traps. Although the exact shape of the trap density of state (DOS) remains unknown, the measurements indicate that it is composed of a high density of shallow traps together with a medium density of deep traps. In the dark (Figure 6.7e), a low density of charge carriers are induced by the gate. Since only a fraction of traps are filled, thermal activation of deep traps dominates transport. In illuminated samples (Figure 3f), however, a high density of photo-excited charge carriers are generated and deep traps are completely filled. In this case, at high temperatures only shallow traps influence charge transport. At low temperatures, also shallow traps

Sample	*Device*	*Ch. Length*	*Ch. Width*	*Figures*
A	*A1*	10 µm	500 µm	6.1d,e,f; 6.2a,b,c,d; 6.3a,b,c,d; 6.4; 6.6;
	A2	20 µm	500 µm	6.2b,c,d; 6.3b,c,d; 6.4; 6.5; 6.8
	A3	30 µm	500 µm	6.2b,c,d; 6.3b,c,d; 6.4; 6.5; 6.8
B	*B1*	10 µm	500 µm	6.4; 6.7
	B2	20 µm	500 µm	6.4; 6.7

Table 6.1 Sample Overview: *Each sample contains several devices with different channel lengths or widths and has been prepared individually according to the steps given in the methods section. The last column lists all Figures, the data from a particular device has been used for.*

freeze out enabling phonon-limited transport. This tolerance of charge transport in the bright state with respect to deep traps is remarkable. The suppressed influence of deep traps can also be seen as an extension to the notion of "defect tolerance" in perovskite materials that has only been connected to the presence of shallow traps so far[47–51].

6.4 Conclusion

In summary, $CsPbBr_3$ nanowire FET devices have been successfully fabricated. Without illumination, a field-effect with an on/off ratio of more than 10^4 and saturation mobilities reaching up 0.004 $cm^2\ V^{-1}\ s^{-1}$ at room temperature are demonstrated. At the same time, photoconductivity with mobilities of up to 0.018 $cm^2\ V^{-1}\ s^{-1}$ and responsivities of up to 31 $A\ W^{-1}$ illustrate the promising phototransistor properties of $CsPbBr_3$ devices. Furthermore, transport properties down to cryogenic temperatures were investigated in detail. It is shown that transport in the dark is dominated by deep traps and freezes out at low temperatures. Surprisingly, when switching on the illumination, excellent photoconductivity even exhibiting phonon-limited characteristics can be observed. This intriguing observation highlights and further extends the notion of the so-called "defect tolerance" of perovskite materials, since not only the influence of shallow traps but also of deep traps on the charge carrier mobility is completely suppressed in illuminated samples. These findings provide further insight into defect states and enable a deeper understanding of charge transport in all-inorganic perovskite systems. They underline the superior optoelectronic properties of perovskite systems and indicate the importance of managing the density of deep traps in advancing the development of efficient optoelectronic devices especially for their use under low-light intensities.

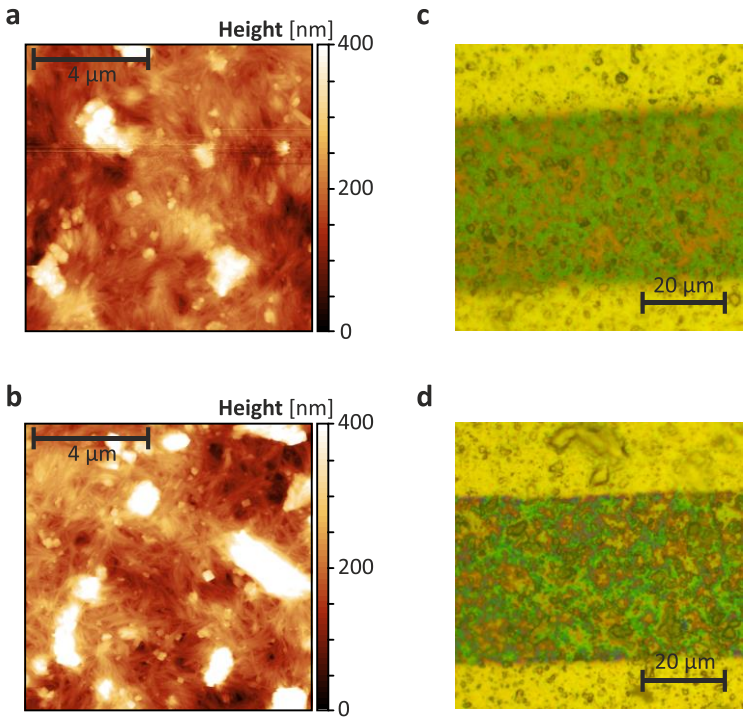

Figure 6.4 Film Topology: *(a,b) AFM image of the perovskite film between source and drain contacts of an exemplary device on sample A (a) and sample B (b). (c,d) Optical microscope image of an exemplary device on Sample A (c) and Sample B (d). The yellow areas are the evaporated gold pads that act as drain and source electrodes.*

6.5 Appendix and Supporting Information

In this section, further measurement and calibration data not shown within the previous sections are presented. The additional data supports the presented results and is shown for completeness and reference. An overview of all samples analyzed within this study is shown in Table 6.1.

Film Topology

Figure 6.4 shows atomic force microscopy (AFM) and optical microscopy images of the perovskite film between source and drain contacts. The film consists of individual nanowires, that cluster together to form a film of several hundred nanometers. The RMS roughness of the film calculated from the AFM image is in the range of 60 nm and 97 nm for sample A and B respectively. By scratching in the perovskite film and measuring the mean step height by atomic force microscopy, a film thickness of 530 nm and 190 nm are obtained for sample A and B respectively.

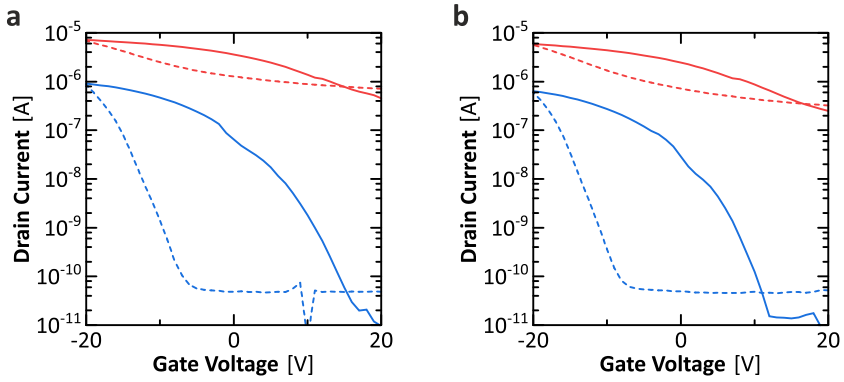

Figure 6.5 Room Temperature Transfer Curves: *Transfer curves of devices A2 (a) and A3 (b) with (red) and without (blue) illumination. The solid lines represent the forward, and the dotted lines the backward sweep.*

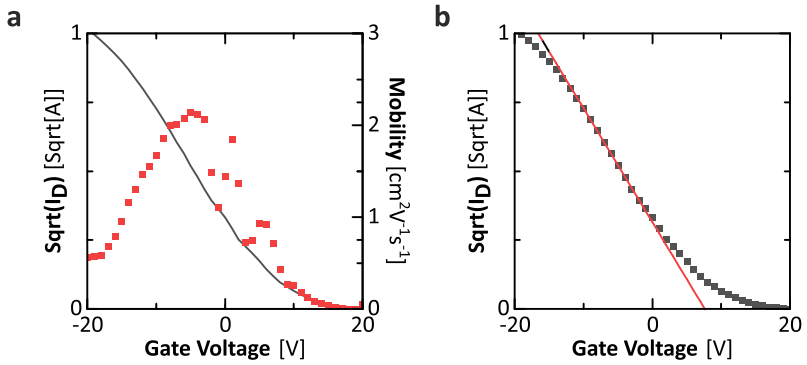

Figure 6.6 Determination of Mobility and Threshold Voltage: *(a) Square root of the drain current (black) together with the calculated mobility (red) using equation (6.4). The data shown here corresponds to the device A1. (b) Square root of the drain current (black) as a function of the gate voltage. The red line represents the linear fit to the drain current data points. The threshold voltage can be extracted by extrapolating the linear fit to zero current. The data shown here corresponds to device A1.*

Additional Room Temperature Transfer Curves

Further transfer curves of two additional devices on sample A are shown in Figure 6.5.

Calculation of the Field Effect Mobility and Threshold Voltage

The field-effect mobility in the saturation regime can be estimated by using the relation of the drain current I_D on the gate voltage V_G (see section 2.4.1 for more details)[109,111,112]

$$I_D = \frac{W}{2L}\mu_{FET}C(V_G - V_{th})^2, \tag{6.3}$$

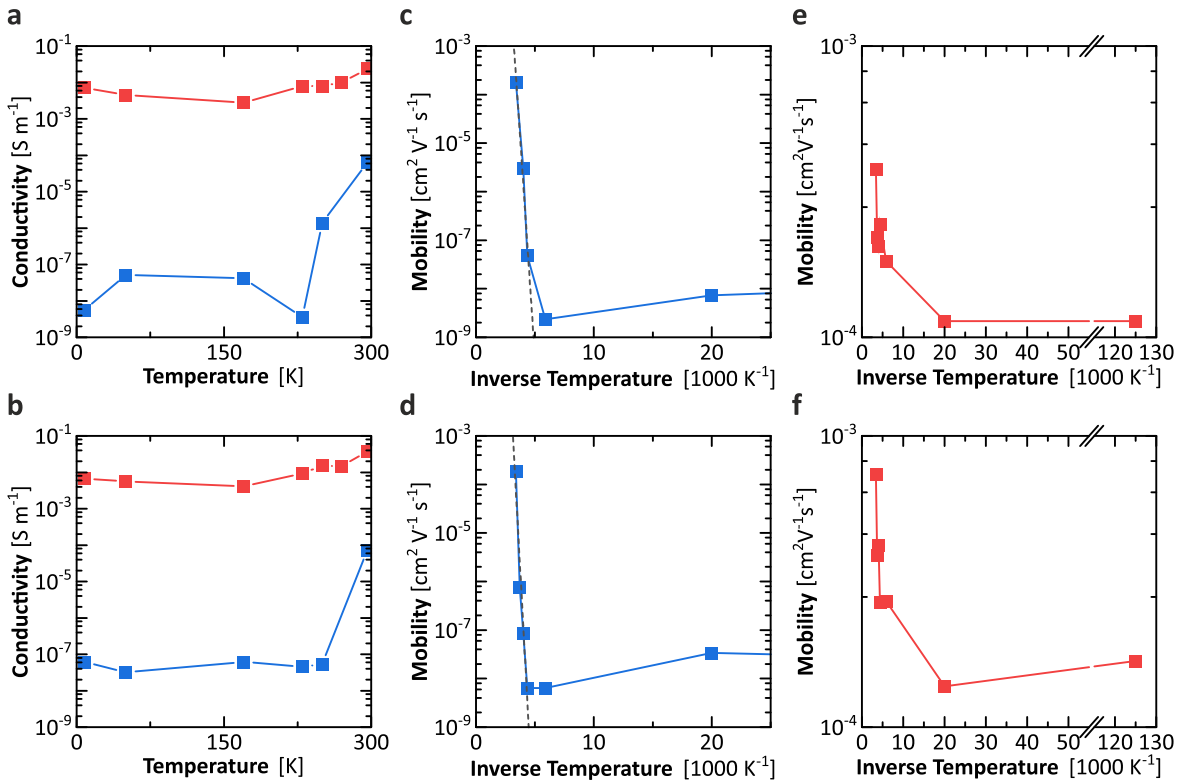

Figure 6.7 Temperature Dependence of Mobility and Conductivity in Sample B: *(a,b) Temperature dependence of the conductivity for devices B1 (a) and B2 (d). (c,d) Temperature dependence of the mobility without illumination of devices B1 (b) and B2 (e). (c,f) Temperature dependence of the mobility with illumination of devices B1 (c) and B2 (f)*

where W is the channel width, L is the channel length, C is the capacitance of the gate dielectric per unit area, V_{th} the threshold voltage and μ_{FET} the field effect mobility. Taking the derivative with respect to the gate voltage V_{G} yields the field-effect mobility in the saturation regime[111]

$$\mu_{\mathrm{FET}} = \frac{2L}{CW}\left(\frac{\partial\sqrt{I_{\mathrm{D}}}}{\partial V_{\mathrm{G}}}\right)^2 \tag{6.4}$$

An example of the determination of the gate dependent mobility is shown in Figure 6.6a. For further calculation or reference, only the maximum mobility is used. The threshold voltage V_{th} is calculated by fitting a linear function to $\sqrt{I_{\mathrm{D}}}$ at the mobility maximum[111,112]. The threshold voltage V_{th} is then given by the extrapolation of linear fit to zero drain current[111,112]. This is shown in exemplarily in Figure 6.6b.

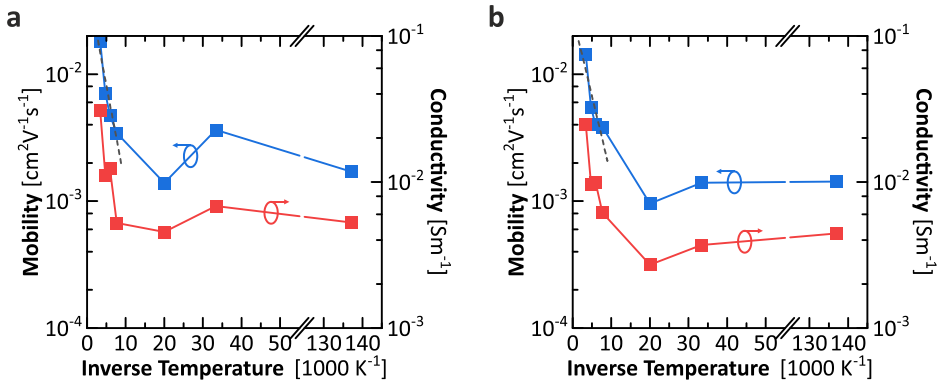

Figure 6.8 Temperature Dependence of Mobility and Conductivity in Sample A: *The Plots show data from device A2 (a) and A3 (b).*

Temperature Dependent Mobility and Conductivity of Sample B

In order to confirm the observations described in the main text, the measurements were repeated for another set of devices (device B1 and B2) on an additional sample. The temperature dependent conductivity and mobility are shown in Figure 6.7. The behavior is qualitatively the same as for the devices that have been discussed in the main text. However, the activation energies in the dark state of 712 meV for device B1 and 887 meV for device B2 are much lower. In bright illumination conditions, the activation energies of 17 meV for device B1 and 27 meV for device B2 are very comparable to the values calculated in the main text.

Temperature Dependent Mobility and Conductivity of Sample A

Additional measurements of the temperature dependent mobility and conductivity of further devices on sample A are shown in Figure 6.8.

7 Conclusion

Within the first part of this thesis, magnetotransport characteristics of correlated states in high-quality trilayer graphene with ABA and ABC stacking order have been investigated. First, ABA trilayer graphene was encapsulated in hBN and fitted with dual graphite gates and graphite contacts. The dual gate structure allowed for independent tuning of charge carrier density and perpendicular electric field. At vanishing electric fields, the band structure of ABA trilayer graphene consists of a linear monolayer-like and a parabolic bilayer-like band. Applying a perpendicular electric field hybridizes these bands and leads to the formation of two sets of three off-center Dirac gullies for both holes and electrons that are interconnected via C_3 symmetry. The Lifshitz transitions that are necessitated by the band structure transformation have been observed in transport measurements that map the conductance as a function of charge carrier density and electric field. In the quantum Hall regime, in addition to the spin degeneracy, the emergence of Dirac gullies leads to the formation of quasi-degenerate triplet states that inherit the C_3 symmetry. The magnetotransport data exhibits strong plateaus at filling factors that are multiples of three consistent with the three-fold triplet state degeneracy but broken spin degeneracy. However, unexpected from single-particle simulations, the triplet state degeneracy is also broken at high electric fields and several integer plateaus are clearly discernable. Indeed, theory shows that increasing the electric field quenches the triplet state energy and interactions become dominant. The experimental results are consistent with Hartree-Fock simulations indicating that C_3 symmetry is spontaneously broken above a critical electric field giving rise to a spontaneous gully-polarized nematic ground state.

Second, dual-gated ABC trilayer graphene was fabricated and subsequently suspended between the gate electrodes via wet etching. The band structure of ABC trilayer graphene host chiral quasiparticles that exhibit a Berry phase of ± 3π when encircling the K or K' valley respectively. Due to the flat low-energy dispersion, ABC trilayer graphene has been predicted to be very susceptible towards spontaneous chiral symmetry breaking at charge neutrality. As a consequence of the giant Berry curvature, a family of five competing spontaneous quantum Hall state with a unique set of spin, valley and charge Hall conductivities each have been postulated: The insulating quantum valley Hall (QVH) state, the (canted) layer antiferromagnetic (CAF/LAF) and the quantum spin Hall (QSH) state as well as the conductive quantum anomalous Hall (QAH) state and the “All” state. At charge neutrality, maps of the conductance with respect to electric field and magnetic field reveal the

presence of two insulating phases separated by a transition region of increased conductance. In agreement with theory and previous studies on ABC trilayer graphene, these two phases could be identified with the LAF/CAF phase at vanishing electric field and the QVH phase at high electric fields. This identification was further ascertained by noting that the transition line is linear in magnetic field in agreement with theoretical predictions. Although the LAF/CAF seems to survive down to vanishing magnetic fields, the non-monotonous dependence of the conductance close to zero magnetic field is suggestive of the presence of a third phase. In the quantum Hall regime, strong plateaus at filling factors ν = ±6 emerge that are accompanied by pronounced ν = ±3 plateaus at high electric fields. These plateaus persist down to exceptionally low magnetic fields of less than 50 mT and are very indicative of the presence of spontaneous quantum Hall states with non-zero charge Hall conductivity. Indeed, the measurements agree very well with the spontaneous QAH and the "All" state that are predicted to exhibit Hall conductivities of ν = ±6 and ν = ±3 respectively even in the absence of magnetic fields. Furthermore, the increase in stability of the ν = ±3 state with electric field is consistent with the predicted layer-polarization of the "All" state. Besides their Hall conductivity at vanishing magnetic fields, these two states are also predicted to exhibit a peculiar non-zero orbital magnetic moment that is purely driven by the non-trivial Berry curvature. In order to provide additional proof of the presence of the "All" state and the QAH state, the orbital magnetic moment was probed by magnetic hysteresis measurements. The hysteresis curves reveal a substantial hysteresis close to filling factors ν = ±6 and ν = ±3, while it is absent for filling factors far away. Although these states could be stabilized in magnetic fields, they seem to lose the competition to the LAF/CAF and the QVH state at charge neutrality.

In summary, the findings of this thesis provide new insights into the physics of correlated states in ABC and ABA trilayer graphene. It was shown, that electron-electron interactions in trilayer graphene can be readily tuned via electrostatic gating and magnetic fields revealing several interaction-induced many-body ground states that break one or more symmetries of the system. While transport measurements in ABA multilayer graphene demonstrate the emergence of an interaction-induced ground state that breaks the rotational symmetry of the system, ABC trilayer graphene displays several exotic quantum Hall states that spontaneously break chiral symmetry. Together, these results highlight the great potential of multilayer graphene as a highly-tunable platform to investigate fundamental many-body phenomena and facilitate the development of novel technologies exploiting correlated states for quantum computing and low-power electronics. However, further studies using four-terminal geometries are needed to understand the nature of edge channels in the spontaneous Hall phases as well as to probe transport anisotropies associated with the rotational symmetry breaking.

In the second part of the thesis, charge traps in perovskite nanowire field-effect transistor devices have been investigated. In order to access information about the transport characteristics of all-

inorganic $CsPbBr_3$ nanowire ensembles, thin nanowire films have been fabricated and equipped with top-contact gold electrodes. The devices show a distinct field-effect with saturation mobilities of 4×10^{-3} cm^2 V^{-1} s^{-1} at room temperature in the absence of illumination and photoresponsivities of up to 31 A W^{-1} upon white light illumination. In the dark, transport is dominated by deep traps and freezes out completely at low temperatures. Surprisingly, when switching on the illumination, excellent photoconductivity is recovered and the mobility even shows signs of phonon-limited transport at low temperatures. This highlights the excellent optoelectronic properties of all-inorganic perovskite materials and underlines their exceptional “defect tolerance”.

The results presented in this thesis facilitate deeper understanding of defect states and charge transport in all-inorganic perovskite systems. They highlight the exceptional optoelectronic properties of perovskites and provide guidelines for improving the performance of perovskite based solar cells and phototransistors.

References

1. A. K. Geim and K. S. Novoselov. The rise of graphene. *Nat. Mater.* **6,** 183–191 (2007).
2. P. R. Wallace. The Band Theory of Graphite. *Phys. Rev.* **71,** 622–634 (1947).
3. H. S. Lipson and A. R. Stokes. The structure of graphite. *Proc. R. Soc. Lond. A* **181,** 101–105 (1942).
4. K. S. Novoselov, A. K. Geim, S. V. Morozov, D. Jiang, Y. Zhang, S. V. Dubonos, I. V. Grigorieva and A. A. Firsov. Electric field effect in atomically thin carbon films. *Science* **306,** 666–669 (2004).
5. K. S. Novoselov, V. I. Fal'ko, L. Colombo, P. R. Gellert, M. G. Schwab and K. Kim. A roadmap for graphene. *Nature* **490,** 192–200 (2012).
6. D. Costanzo, S. Jo, H. Berger and A. F. Morpurgo. Gate-induced superconductivity in atomically thin MoS2 crystals. *Nat. Nanotech.* **11,** 339–344 (2016).
7. Q. H. Wang, K. Kalantar-Zadeh, A. Kis, J. N. Coleman and M. S. Strano. Electronics and optoelectronics of two-dimensional transition metal dichalcogenides. *Nat. Nanotech.* **7,** 699–712 (2012).
8. B. Huang, G. Clark, D. R. Klein, D. MacNeill, E. Navarro-Moratalla, K. L. Seyler, N. Wilson, M. A. McGuire, D. H. Cobden, Di Xiao, W. Yao, P. Jarillo-Herrero and X. Xu. Electrical control of 2D magnetism in bilayer CrI3. *Nat. Nanotech.* **13,** 544–548 (2018).
9. B. Huang, G. Clark, E. Navarro-Moratalla, D. R. Klein, R. Cheng, K. L. Seyler, D. Zhong, E. Schmidgall, M. A. McGuire, D. H. Cobden, W. Yao, Di Xiao, P. Jarillo-Herrero and X. Xu. Layer-dependent ferromagnetism in a van der Waals crystal down to the monolayer limit. *Nature* **546,** 270–273 (2017).
10. K. S. Novoselov and A. H. Castro Neto. Two-dimensional crystals-based heterostructures. Materials with tailored properties. *Phys. Scr.* **T146,** 14006 (2012).
11. N. Ubrig, E. Ponomarev, J. Zultak, D. Domaretskiy, V. Zólyomi, D. Terry, J. Howarth, I. Gutiérrez-Lezama, A. Zhukov, Z. R. Kudrynskyi, Z. D. Kovalyuk, A. Patané, T. Taniguchi, K.

Watanabe, R. V. Gorbachev, V. I. Fal'ko and A. F. Morpurgo. Design of van der Waals interfaces for broad-spectrum optoelectronics. *Nat. Mater.* **19,** 299–304 (2020).

12. W. Bao, L. Jing, J. Velasco, Y. Lee, G. Liu, D. Tran, B. Standley, M. Aykol, S. B. Cronin, D. Smirnov, M. Koshino, E. McCann, M. Bockrath and C. N. Lau. Stacking-dependent band gap and quantum transport in trilayer graphene. *Nat. Phys.* **7,** 948–952 (2011).
13. S. H. Jhang, M. F. Craciun, S. Schmidmeier, S. Tokumitsu, S. Russo, M. Yamamoto, Y. Skourski, J. Wosnitza, S. Tarucha, J. Eroms and C. Strunk. Stacking-order dependent transport properties of trilayer graphene. *Phys. Rev. B* **84,** 161408 (2011).
14. M. Koshino. Interlayer screening effect in graphene multilayers with ABA and ABC stacking. *Phys. Rev. B* **81,** 125304 (2010).
15. M. Koshino and E. McCann. Trigonal warping and Berry's phase Nπ in ABC-stacked multilayer graphene. *Phys. Rev. B* **80,** 165409 (2009).
16. M. Koshino and E. McCann. Landau level spectra and the quantum Hall effect of multilayer graphene. *Phys. Rev. B* **83,** 165443 (2011).
17. R. T. Weitz, M. T. Allen, B. E. Feldman, J. Martin and A. Yacoby. Broken-symmetry states in doubly gated suspended bilayer graphene. *Science* **330,** 812–816 (2010).
18. F. Zhang. Spontaneous chiral symmetry breaking in bilayer graphene. *Synth. Met.* **210,** 9–18 (2015).
19. F. Zhang, J. Jung, G. A. Fiete, Q. Niu and A. H. MacDonald. Spontaneous quantum Hall states in chirally stacked few-layer graphene systems. *Phys. Rev. Lett.* **106,** 156801 (2011).
20. P. Rao and M. Serbyn. Gully quantum Hall ferromagnetism in biased trilayer graphene. *Phys. Rev. B* **101,** 245411 (2020).
21. N. B. Kopnin, M. Ijäs, A. Harju and T. T. Heikkilä. High-temperature surface superconductivity in rhombohedral graphite. *Phys. Rev. B* **87,** 140503 (2013).
22. N. B. Kopnin, T. T. Heikkilä and G. E. Volovik. High-temperature surface superconductivity in topological flat-band systems. *Phys. Rev. B* **83,** 220503 (2011).
23. O. Vafek and K. Yang. Many-body instability of Coulomb interacting bilayer graphene. Renormalization group approach. *Phys. Rev. B* **81,** 41401 (2010).
24. V. N. Kotov, B. Uchoa, V. M. Pereira, F. Guinea and A. H. Castro Neto. Electron-Electron Interactions in Graphene. Current Status and Perspectives. *Rev. Mod. Phys.* **84,** 1067–1125 (2012).

25. G. Giuliani and G. Vignale. *Quantum theory of the electron liquid* (Cambridge Univ. Press, Cambridge, 2012)

26. Y. Lee, D. Tran, K. Myhro, J. Velasco, N. Gillgren, C. N. Lau, Y. Barlas, J. M. Poumirol, D. Smirnov and F. Guinea. Competition between spontaneous symmetry breaking and single-particle gaps in trilayer graphene. *Nat. Commun.* **5,** 5656 (2014).

27. J. Velasco, Y. Lee, F. Zhang, K. Myhro, D. Tran, M. Deo, D. Smirnov, A. H. MacDonald and C. N. Lau. Competing ordered states with filling factor two in bilayer graphene. *Nat. Commun.* **5,** 4550 (2014).

28. J. Velasco, L. Jing, W. Bao, Y. Lee, P. Kratz, V. Aji, M. Bockrath, C. N. Lau, C. Varma, R. Stillwell, D. Smirnov, F. Zhang, J. Jung and A. H. MacDonald. Transport spectroscopy of symmetry-broken insulating states in bilayer graphene. *Nat. Nanotech.* **7,** 156–160 (2012).

29. M. Serbyn and D. A. Abanin. New Dirac points and multiple Landau level crossings in biased trilayer graphene. *Phys. Rev. B* **87,** 115422 (2013).

30. T. Morimoto and M. Koshino. Gate-induced Dirac cones in multilayer graphenes. *Phys. Rev. B* **87,** 85424 (2013).

31. J. Jung, F. Zhang and A. H. MacDonald. Lattice theory of pseudospin ferromagnetism in bilayer graphene. Competing interaction-induced quantum Hall states. *Phys. Rev. B* **83,** 115408 (2011).

32. K. I. Bolotin, K. J. Sikes, Z. Jiang, M. Klima, G. Fudenberg, J. Hone, P. Kim and H. L. Stormer. Ultrahigh electron mobility in suspended graphene. *Solid State Commun.* **146,** 351–355 (2008).

33. C. R. Dean, A. F. Young, I. Meric, C. Lee, L. Wang, S. Sorgenfrei, K. Watanabe, T. Taniguchi, P. Kim, K. L. Shepard and J. Hone. Boron nitride substrates for high-quality graphene electronics. *Nat. Nanotech.* **5,** 722–726 (2010).

34. L. Wang, I. Meric, P. Y. Huang, Q. Gao, Y. Gao, H. Tran, T. Taniguchi, K. Watanabe, L. M. Campos, D. A. Muller, J. Guo, P. Kim, J. Hone, K. L. Shepard and C. R. Dean. One-dimensional electrical contact to a two-dimensional material. *Science* **342,** 614–617 (2013).

35. M. Yankowitz, Q. Ma, P. Jarillo-Herrero and B. J. LeRoy. van der Waals heterostructures combining graphene and hexagonal boron nitride. *Nat. Rev. Phys.* **1,** 112–125 (2019).

36. D. A. Valverde-Chávez, C. S. Ponseca, C. C. Stoumpos, A. Yartsev, M. G. Kanatzidis, V. Sundström and D. G. Cooke. Intrinsic femtosecond charge generation dynamics in single crystal CH3NH3PbI3. *Energy Environ. Sci.* **8,** 3700–3707 (2015).

37. J. S. Manser and P. V. Kamat. Band filling with free charge carriers in organometal halide perovskites. *Nat. Photonics* **8,** 737–743 (2014).

38. S. D. Stranks, G. E. Eperon, G. Grancini, C. Menelaou, M. J. P. Alcocer, T. Leijtens, L. M. Herz, A. Petrozza and H. J. Snaith. Electron-hole diffusion lengths exceeding 1 micrometer in an organometal trihalide perovskite absorber. *Science* **342,** 341–344 (2013).

39. L. Polavarapu, B. Nickel, J. Feldmann and A. S. Urban. Advances in Quantum-Confined Perovskite Nanocrystals for Optoelectronics. *Adv. Energy Mater.* **7,** 1700267 (2017).

40. Y. Tong, M. Fu, E. Bladt, H. Huang, A. F. Richter, K. Wang, P. Müller-Buschbaum, S. Bals, P. Tamarat, B. Lounis, J. Feldmann and L. Polavarapu. Chemical Cutting of Perovskite Nanowires into Single-Photon Emissive Low-Aspect-Ratio CsPbX3 (X=Cl, Br, I) Nanorods. *Angew. Chem., Int. Ed. Engl.* **57,** 16094–16098 (2018).

41. Y. Tong, B. J. Bohn, E. Bladt, K. Wang, P. Müller-Buschbaum, S. Bals, A. S. Urban, L. Polavarapu and J. Feldmann. From Precursor Powders to CsPbX3 Perovskite Nanowires. One-Pot Synthesis, Growth Mechanism, and Oriented Self-Assembly. *Angew. Chem., Int. Ed. Engl.* **56,** 13887–13892 (2017).

42. Y. Tong, E. Bladt, M. F. Aygüler, A. Manzi, K. Z. Milowska, V. A. Hintermayr, P. Docampo, S. Bals, A. S. Urban, L. Polavarapu and J. Feldmann. Highly Luminescent Cesium Lead Halide Perovskite Nanocrystals with Tunable Composition and Thickness by Ultrasonication. *Angew. Chem., Int. Ed. Engl.* **55,** 13887–13892 (2016).

43. H. Huang, Y. Li, Y. Tong, E.-P. Yao, M. W. Feil, A. F. Richter, M. Döblinger, A. L. Rogach, J. Feldmann and L. Polavarapu. Spontaneous Crystallization of Perovskite Nanocrystals in Nonpolar Organic Solvents. A Versatile Approach for their Shape-Controlled Synthesis. *Angew. Chem., Int. Ed. Engl.* **58,** 16558–16562 (2019).

44. X. Zhang, S. Chen, X. Wang and A. Pan. Controlled Synthesis and Photonics Applications of Metal Halide Perovskite Nanowires. *Small Methods* **3,** 1800294 (2019).

45. H. Zhu, Y. Fu, F. Meng, X. Wu, Z. Gong, Q. Ding, M. V. Gustafsson, M. T. Trinh, S. Jin and X.-Y. Zhu. Lead halide perovskite nanowire lasers with low lasing thresholds and high quality factors. *Nat. Mater.* **14,** 636–642 (2015).

46. M. Shoaib, X. Zhang, X. Wang, H. Zhou, T. Xu, X. Wang, X. Hu, H. Liu, X. Fan, W. Zheng, T. Yang, S. Yang, Q. Zhang, X. Zhu, L. Sun and A. Pan. Directional Growth of Ultralong CsPbBr3 Perovskite Nanowires for High-Performance Photodetectors. *J. Am. Chem. Soc.* **139,** 15592–15595 (2017).

47. J. Kang and L.-W. Wang. High Defect Tolerance in Lead Halide Perovskite CsPbBr3. *J. Phys. Chem. Lett.* **8,** 489–493 (2017).

48. Y. Jiang, X. Wang and A. Pan. Properties of Excitons and Photogenerated Charge Carriers in Metal Halide Perovskites. *Adv. Mater.* **31,** 1806671 (2019).

49. H. Jin, E. Debroye, M. Keshavarz, I. G. Scheblykin, M. B. J. Roeffaers, J. Hofkens and J. A. Steele. It's a trap! On the nature of localised states and charge trapping in lead halide perovskites. *Mater. Horiz.* **7,** 397–410 (2020).

50. M. Bruzzi, F. Gabelloni, N. Calisi, S. Caporali and A. Vinattieri. Defective States in Micro-Crystalline $CsPbBr_3$ and Their Role on Photoconductivity. *Nanomaterials* **9,** 177 (2019).

51. A. Zakutayev, C. M. Caskey, A. N. Fioretti, D. S. Ginley, J. Vidal, V. Stevanovic, E. Tea and S. Lany. Defect Tolerant Semiconductors for Solar Energy Conversion. *J. Phys. Chem. Lett.* **5,** 1117–1125 (2014).

52. C. Lee, X. Wei, J. W. Kysar and J. Hone. Measurement of the Elastic Properties and Intrinsic Strength of Monolayer Graphene. *Science* **321,** 385–388 (2008).

53. A. H. Castro Neto, F. Guinea, N. M. R. Peres, K. S. Novoselov and A. K. Geim. The electronic properties of graphene. *Rev. Mod. Phys.* **81,** 109–162 (2009).

54. M. I. Katsnelson. *Graphene: Carbon in two dimensions* (Cambridge University Press, Cambridge, 2012)

55. E. McCann and V. I. Fal'ko. Landau-level degeneracy and quantum Hall effect in a graphite bilayer. *Phys. Rev. Lett.* **96,** 86805 (2006).

56. K. S. Novoselov, E. McCann, S. V. Morozov, V. I. Fal'ko, M. I. Katsnelson, U. Zeitler, D. Jiang, F. Schedin and A. K. Geim. Unconventional quantum Hall effect and Berry's phase of 2π in bilayer graphene. *Nat. Phys.* **2,** 177–180 (2006).

57. M. I. Katsnelson, K. S. Novoselov and A. K. Geim. Chiral tunnelling and the Klein paradox in graphene. *Nat. Phys.* **2,** 620–625 (2006).

58. K. S. Novoselov, A. K. Geim, S. V. Morozov, D. Jiang, M. I. Katsnelson, I. V. Grigorieva, S. V. Dubonos and A. A. Firsov. Two-dimensional gas of massless Dirac fermions in graphene. *Nature* **438,** 197–200 (2005).

59. M. V. Berry. Quantal phase factors accompanying adiabatic changes. *Proc. R. Soc. Lond. A* **392,** 45–57 (1984).

60. Y. Zhang, Y.-W. Tan, H. L. Stormer and P. Kim. Experimental observation of the quantum Hall effect and Berry's phase in graphene. *Nature* **438,** 201–204 (2005).

61. Di Xiao, M.-C. Chang and Q. Niu. Berry phase effects on electronic properties. *Rev. Mod. Phys.* **82,** 1959–2007 (2010).

62. F. Zhang, B. Sahu, H. Min and A. H. MacDonald. Band structure of ABC -stacked graphene trilayers. *Phys. Rev. B* **82,** 35409 (2010).

63. M. S. Dresselhaus and G. Dresselhaus. Intercalation compounds of graphite. *Adv. Phys.* **51,** 1–186 (2002).

64. J. W. McClure. Electron energy band structure and electronic properties of rhombohedral graphite. *Carbon* **7,** 425–432 (1969).

65. J. C. Slonczewski and P. R. Weiss. Band Structure of Graphite. *Phys. Rev.* **109,** 272–279 (1958).

66. E. McCann, D. S.L. Abergel and V. I. Fal'ko. Electrons in bilayer graphene. *Solid State Commun.* **143,** 110–115 (2007).

67. F. Guinea, A. H. Castro Neto and N. M. R. Peres. Electronic states and Landau levels in graphene stacks. *Phys. Rev. B* **73,** 245426 (2006).

68. M. Aoki and H. Amawashi. Dependence of band structures on stacking and field in layered graphene. *Solid State Commun.* **142,** 123–127 (2007).

69. Y. Nam, D.-K. Ki, D. Soler-Delgado and A. F. Morpurgo. A family of finite-temperature electronic phase transitions in graphene multilayers. *Science* **362,** 324–328 (2018).

70. A. L. Grushina, D.-K. Ki, M. Koshino, A. A. L. Nicolet, C. Faugeras, E. McCann, M. Potemski and A. F. Morpurgo. Insulating state in tetralayers reveals an even-odd interaction effect in multilayer graphene. *Nat. Commun.* **6,** 6419 (2015).

71. T. Taychatanapat, K. Watanabe, T. Taniguchi and P. Jarillo-Herrero. Quantum Hall effect and Landau-level crossing of Dirac fermions in trilayer graphene. *Nat. Phys.* **7,** 621–625 (2011).

72. Y. Shi, S. Xu, Y. Yang, S. Slizovskiy, S. V. Morozov, S.-K. Son, S. Ozdemir, C. Mullan, J. Barrier, J. Yin, A. I. Berdyugin, B. A. Piot, T. Taniguchi, K. Watanabe, V. I. Fal'ko, K. S. Novoselov, A. K. Geim and A. Mishchenko. Electronic phase separation in multilayer rhombohedral graphite. *Nature* **584,** 210–214 (2020).

73. R. R. Haering. Band Structure of Rhombohedral Graphite. *Can. J. Phys.* **36,** 352–362 (1958).

74. S. Slizovskiy, E. McCann, M. Koshino and V. I. Fal'ko. Films of rhombohedral graphite as two-dimensional topological semimetals. *Commun. Phys.* **2,** 45 (2019).

75. L. Zhang, Y. Zhang, J. Camacho, M. Khodas and I. Zaliznyak. The experimental observation of quantum Hall effect of l=3 chiral quasiparticles in trilayer graphene. *Nat. Phys.* **7,** 953–957 (2011).

76. H. Henck, J. Avila, Z. Ben Aziza, D. Pierucci, J. Baima, B. Pamuk, J. Chaste, D. Utt, M. Bartos, K. Nogajewski, B. A. Piot, M. Orlita, M. Potemski, M. Calandra, M. C. Asensio, F. Mauri, C. Faugeras and A. Ouerghi. Flat electronic bands in long sequences of rhombohedral-stacked graphene. *Phys. Rev. B* **97,** 245421 (2018).

77. W. Wang, Y. Shi, A. A. Zakharov, M. Syväjärvi, R. Yakimova, R. I. G. Uhrberg and J. Sun. Flat-Band Electronic Structure and Interlayer Spacing Influence in Rhombohedral Four-Layer Graphene. *Nano Lett.* **18,** 5862–5866 (2018).

78. F. Zhang, H. Min and A. H. MacDonald. Competing ordered states in bilayer graphene. *Phys. Rev. B* **86,** 155128 (2012).

79. Y. Nam, D.-K. Ki, M. Koshino, E. McCann and A. F. Morpurgo. Interaction-induced insulating state in thick multilayer graphene. *2D Mater.* **3,** 45014 (2016).

80. H. Min and A. H. MacDonald. Chiral decomposition in the electronic structure of graphene multilayers. *Phys. Rev. B* **77,** 155416 (2008).

81. I. M. Lifshitz. Anomalies of Electron Characteristics of a Metal in the High Pressure Region. *Soviet Physics JEPT* **11,** 1130 (1960).

82. J. Xue, J. Sanchez-Yamagishi, D. Bulmash, P. Jacquod, A. Deshpande, K. Watanabe, T. Taniguchi, P. Jarillo-Herrero and B. J. LeRoy. Scanning tunnelling microscopy and spectroscopy of ultra-flat graphene on hexagonal boron nitride. *Nat. Mater.* **10,** 282–285 (2011).

83. C.-H. Ho, C.-P. Chang and M.-F. Lin. Evolution and dimensional crossover from the bulk subbands in ABC-stacked graphene to a three-dimensional Dirac cone structure in rhombohedral graphite. *Phys. Rev. B* **93,** 75437 (2016).

84. B. Partoens and F. M. Peeters. From graphene to graphite. Electronic structure around the K point. *Phys. Rev. B* **74,** 75404 (2006).

85. T. Chari, R. Ribeiro-Palau, C. R. Dean and K. Shepard. Resistivity of Rotated Graphite-Graphene Contacts. *Nano Lett.* **16,** 4477–4482 (2016).

86. L. Landau. Diamagnetismus der Metalle. *Z. Physik* **64,** 629–637 (1930).

87. K. von Klitzing. The quantized Hall effect. *Rev. Mod. Phys.* **58,** 519–531 (1986).

88. K. v. Klitzing, G. Dorda and M. Pepper. New Method for High-Accuracy Determination of the Fine-Structure Constant Based on Quantized Hall Resistance. *Phys. Rev. Lett.* **45,** 494–497 (1980).

89. V. P. Gusynin and S. G. Sharapov. Unconventional integer quantum Hall effect in graphene. *Phys. Rev. Lett.* **95,** 146801 (2005).

References

90. E. H. Hall. On a New Action of the Magnet on Electric Currents. *Am. J. Math.* **2,** 287 (1879).

91. H. Ibach and H. Lüth. *Solid state physics.* 4th ed. (Springer, Heidelberg, 2009)

92. D. A. Abanin and L. S. Levitov. Conformal invariance and shape-dependent conductance of graphene samples. *Phys. Rev. B* **78,** 035416 (2008).

93. J. R. Williams, D. A. Abanin, L. DiCarlo, L. S. Levitov and C. M. Marcus. Quantum Hall conductance of two-terminal graphene devices. *Phys. Rev. B* **80,** 45408 (2009).

94. J. W. McClure. Diamagnetism of Graphite. *Phys. Rev.* **104,** 666–671 (1956).

95. E. McCann. in *Graphene nanoelectronics,* edited by H. Raza (Springer, Heidelberg, 2012), pp. 237–275

96. G. M. Rutter, S. Jung, N. N. Klimov, D. B. Newell, N. B. Zhitenev and J. A. Stroscio. Microscopic polarization in bilayer graphene. *Nat. Phys.* **7,** 649–655 (2011).

97. Y. Lee, J. Velasco, D. Tran, F. Zhang, W. Bao, L. Jing, K. Myhro, D. Smirnov and C. N. Lau. Broken symmetry quantum Hall states in dual-gated ABA trilayer graphene. *Nano Lett.* **13,** 1627–1631 (2013).

98. B. Datta, S. Dey, A. Samanta, H. Agarwal, A. Borah, K. Watanabe, T. Taniguchi, R. Sensarma and M. M. Deshmukh. Strong electronic interaction and multiple quantum Hall ferromagnetic phases in trilayer graphene. *Nat. Commun.* **8,** 14518 (2017).

99. E. A. Henriksen, D. Nandi and J. P. Eisenstein. Quantum Hall Effect and Semimetallic Behavior of Dual-Gated ABA-Stacked Trilayer Graphene. *Phys. Rev. X* **2,** 11004 (2012).

100. Y. Shi, S. Che, K. Zhou, S. Ge, Z. Pi, T. Espiritu, T. Taniguchi, K. Watanabe, Y. Barlas, R. Lake and C. N. Lau. Tunable Lifshitz Transitions and Multiband Transport in Tetralayer Graphene. *Phys. Rev. Lett.* **120,** 96802 (2018).

101. A. A. Zibrov, P. Rao, C. Kometter, E. M. Spanton, J. I. A. Li, C. R. Dean, T. Taniguchi, K. Watanabe, M. Serbyn and A. F. Young. Emergent Dirac Gullies and Gully-Symmetry-Breaking Quantum Hall States in ABA Trilayer Graphene. *Phys. Rev. Lett.* **121,** 167601 (2018).

102. H. Min, G. Borghi, M. Polini and A. H. MacDonald. Pseudospin magnetism in graphene. *Phys. Rev. B* **77,** 41407 (2008).

103. K. Myhro, S. Che, Y. Shi, Y. Lee, K. Thilahar, K. Bleich, D. Smirnov and C. N. Lau. Large tunable intrinsic gap in rhombohedral-stacked tetralayer graphene at half filling. *2D Mater.* **5,** 45013 (2018).

104. F. Freitag, M. Weiss, R. Maurand, J. Trbovic and C. Schönenberger. Spin symmetry of the bilayer graphene ground state. *Phys. Rev. B* **87,** 161402 (2013).

105. Y. Lee, S. Che, J. Valesco Jr., D. Tran, J. Baima, F. Mauri, M. Calandra, M. Bockrath and C. N. Lau. Gate Tunable Magnetism and Giant Magnetoresistance in ABC-stacked Few-Layer Graphene. *arXiv:1911.04450* (2019).

106. J. Martin, B. E. Feldman, R. T. Weitz, M. T. Allen and A. Yacoby. Local compressibility measurements of correlated states in suspended bilayer graphene. *Phys. Rev. Lett.* **105,** 256806 (2010).

107. D. C. Elias, R. V. Gorbachev, A. S. Mayorov, S. V. Morozov, A. A. Zhukov, P. Blake, L. A. Ponomarenko, I. V. Grigorieva, K. S. Novoselov, F. Guinea and A. K. Geim. Dirac cones reshaped by interaction effects in suspended graphene. *Nat. Phys.* **7,** 701–704 (2011).

108. W. Shockley and G. L. Pearson. Modulation of Conductance of Thin Films of Semi-Conductors by Surface Charges. *Phys. Rev.* **74,** 232–233 (1948).

109. P. Stallinga. *Electrical Characterization of Organic Electronic Materials and Devices* (John Wiley & Sons Ltd, Chichester, UK, 2009)

110. D. Kahng. A historical perspective on the development of MOS transistors and related devices. *IEEE Trans. Electron Devices* **23,** 655–657 (1976).

111. Z. A. Lamport, H. F. Haneef, S. Anand, M. Waldrip and O. D. Jurchescu. Tutorial. Organic field-effect transistors: Materials, structure and operation. *J. Appl. Phys.* **124,** 71101 (2018).

112. J. Zaumseil and H. Sirringhaus. Electron and ambipolar transport in organic field-effect transistors. *Chem. Rev.* **107,** 1296–1323 (2007).

113. H. F. Haneef, A. M. Zeidell and O. D. Jurchescu. Charge carrier traps in organic semiconductors. A review on the underlying physics and impact on electronic devices. *J. Mater. Chem. C* **8,** 759–787 (2020).

114. F. R. Geisenhof, F. Winterer, S. Wakolbinger, T. D. Gokus, Y. C. Durmaz, D. Priesack, J. Lenz, F. Keilmann, K. Watanabe, T. Taniguchi, R. Guerrero-Avilés, M. Pelc, A. Ayuela and R. T. Weitz. Anisotropic Strain-Induced Soliton Movement Changes Stacking Order and Band Structure of Graphene Multilayers. Implications for Charge Transport. *ACS Appl. Nano Mater.* **2,** 6067–6075 (2019).

115. H. Li, Z. Ying, B. Lyu, A. Deng, L. Wang, T. Taniguchi, K. Watanabe and Z. Shi. Electrode-Free Anodic Oxidation Nanolithography of Low-Dimensional Materials. *Nano Lett.* **18,** 8011–8015 (2018).

116. P. J. Zomer, M. H. D. Guimarães, J. C. Brant, N. Tombros and B. J. van Wees. Fast pick up technique for high quality heterostructures of bilayer graphene and hexagonal boron nitride. *Appl. Phys. Lett.* **105,** 13101 (2014).

117. D. G. Purdie, N. M. Pugno, T. Taniguchi, K. Watanabe, A. C. Ferrari and A. Lombardo. Cleaning interfaces in layered materials heterostructures. *Nat. Commun.* **9,** 5387 (2018).

118. C. F. Fan, T. Çagin, W. Shi and K. A. Smith. Local chain dynamics of a model polycarbonate near glass transition temperature. A molecular dynamics simulation. *Macromol. Theory Simul.* **6,** 83–102 (1997).

119. W. Li, Y. Liang, D. Yu, L. Peng, K. P. Pernstich, T. Shen, A. R. Hight Walker, G. Cheng, C. A. Hacker, C. A. Richter, Q. Li, D. J. Gundlach and X. Liang. Ultraviolet/ozone treatment to reduce metal-graphene contact resistance. *Appl. Phys. Lett.* **102,** 183110 (2013).

120. C. Wei Chen, F. Ren, G.-C. Chi, S.-C. Hung, Y. P. Huang, J. Kim, I. I. Kravchenko and S. J. Pearton. UV ozone treatment for improving contact resistance on graphene. *J. Vac. Sci. Technol. B Nanotechnol. Microelectron.* **30,** 60604 (2012).

121. J. A. Robinson, M. LaBella, M. Zhu, M. Hollander, R. Kasarda, Z. Hughes, K. Trumbull, R. Cavalero and D. Snyder. Contacting graphene. *Appl. Phys. Lett.* **98,** 53103 (2011).

122. J. Moser, A. Barreiro and A. Bachtold. Current-induced cleaning of graphene. *Appl. Phys. Lett.* **91,** 163513 (2007).

123. F. Schedin, A. Geim, S. V. Morozov, E. W. Hill, P. Blake, M. I. Katsnelson and K. S. Novoselov. Detection of individual gas molecules adsorbed on graphene. *Nat. Mater.* **6,** 652–655 (2007).

124. R. R. Nair, P. Blake, A. N. Grigorenko, K. S. Novoselov, T. J. Booth, T. Stauber, N. M. R. Peres and A. K. Geim. Fine Structure Constant Defines Visual Transparency of Graphene. *Science* **320,** 1308 (2008).

125. P. Blake, E. W. Hill, A. H. Castro Neto, K. S. Novoselov, D. Jiang, R. Yang, T. J. Booth and A. K. Geim. Making graphene visible. *Appl. Phys. Lett.* **91,** 63124 (2007).

126. H. Li, J. Wu, X. Huang, G. Lu, J. Yang, X. Lu, Q. Xiong and H. Zhang. Rapid and reliable thickness identification of two-dimensional nanosheets using optical microscopy. *ACS Nano* **7,** 10344–10353 (2013).

127. T. A. Nguyen, J.-U. Lee, D. Yoon and H. Cheong. Excitation Energy Dependent Raman Signatures of ABA- and ABC-stacked Few-layer Graphene. *Sci. Rep.* **4,** 4630 (2015).

128. L. M. Malard, M. A. Pimenta, G. Dresselhaus and M. S. Dresselhaus. Raman spectroscopy in graphene. *Phys. Rep.* **473,** 51–87 (2009).

129. A. C. Ferrari and D. M. Basko. Raman spectroscopy as a versatile tool for studying the properties of graphene. *Nat. Nanotech.* **8,** 235–246 (2013).

130. C. H. Lui, Z. Li, Z. Chen, P. V. Klimov, L. E. Brus and T. F. Heinz. Imaging stacking order in few-layer graphene. *Nano Lett.* **11,** 164–169 (2011).

131. A. Das, S. Pisana, B. Chakraborty, S. Piscanec, S. K. Saha, U. V. Waghmare, K. S. Novoselov, H. R. Krishnamurthy, A. K. Geim, A. C. Ferrari and A. K. Sood. Monitoring dopants by Raman scattering in an electrochemically top-gated graphene transistor. *Nat. Nanotech.* **3,** 210–215 (2008).

132. D. M. Basko, S. Piscanec and A. C. Ferrari. Electron-electron interactions and doping dependence of the two-phonon Raman intensity in graphene. *Phys. Rev. B* **80,** 165413 (2009).

133. T. M. G. Mohiuddin, A. Lombardo, R. R. Nair, A. Bonetti, G. Savini, R. Jalil, N. Bonini, D. M. Basko, C. Galiotis, N. Marzari, K. S. Novoselov, A. K. Geim and A. C. Ferrari. Uniaxial strain in graphene by Raman spectroscopy. G peak splitting, Grüneisen parameters, and sample orientation. *Phys. Rev. B* **79,** 205433 (2009).

134. I. Stenger, L. Schué, M. Boukhicha, B. Berini, B. Plaçais, A. Loiseau and J. Barjon. Low frequency Raman spectroscopy of few-atomic-layer thick hBN crystals. *2D Mater.* **4,** 31003 (2017).

135. C. J. Shearer, A. D. Slattery, A. J. Stapleton, J. G. Shapter and C. T. Gibson. Accurate thickness measurement of graphene. *Nanotechnology* **27,** 125704 (2016).

136. G. Jeong, B. Choi, D.-S. Kim, S. Ahn, B. Park, J. H. Kang, H. Min, B. H. Hong and Z. H. Kim. Mapping of Bernal and Non-Bernal Stacking Domains in Bilayer Graphene Using Infrared Nanoscopy. *Nanoscale* **9,** 4191–4195 (2017).

137. D. S. Kim, H. Kwon, A. Y. Nikitin, S. Ahn, L. Martín-Moreno, F. J. García-Vidal, S. Ryu, H. Min and Z. H. Kim. Stacking Structures of Few-Layer Graphene Revealed by Phase-Sensitive Infrared Nanoscopy. *ACS Nano* **9,** 6765–6773 (2015).

138. F. Keilmann and R. Hillenbrand. in *Nano-optics and near-field optical microscopy,* edited by A. V. Zayats & D. Richards (Artech House, Boston, London, 2009), pp. 235–265

139. L. Jiang, Z. Shi, B. Zeng, S. Wang, J.-H. Kang, T. Joshi, C. Jin, L. Ju, J. Kim, T. Lyu, Y.-R. Shen, M. Crommie, H.-J. Gao and F. Wang. Soliton-Dependent Plasmon Reflection at Bilayer Graphene Domain Walls. *Nat. Mater.* **15,** 840–844 (2016).

140. B.-Y. Jiang, G.-X. Ni, Z. Addison, J. K. Shi, X. Liu, S. Y. F. Zhao, P. Kim, E. J. Mele, D. N. Basov and M. M. Fogler. Plasmon Reflections by Topological Electronic Boundaries in Bilayer Graphene. *Nano Lett.* **17,** 7080–7085 (2017).

141. F. Pobell. *Matter and methods at low temperatures.* 3rd ed. (Springer, Berlin, New York, 2007)

142. R. Thevamaran, O. Lawal, S. Yazdi, S.-J. Jeon, J.-H. Lee and E. L. Thomas. Dynamic creation and evolution of gradient nanostructure in single-crystal metallic microcubes. *Science* **354,** 312–316 (2016).

143. X. Li, F. Zhang and A. H. MacDonald. SU(3) Quantum Hall Ferromagnetism in SnTe. *Phys. Rev. Lett.* **116,** 26803 (2016).

144. C. Liu, T. Kondo, R. M. Fernandes, A. D. Palczewski, E. D. Mun, N. Ni, A. N. Thaler, A. Bostwick, E. Rotenberg, J. Schmalian, S. L. Bud'ko, P. C. Canfield and A. Kaminski. Evidence for a Lifshitz transition in electron-doped iron arsenic superconductors at the onset of superconductivity. *Nat. Phys.* **6,** 419–423 (2010).

145. X. Shi, Z.-Q. Han, X.-L. Peng, P. Richard, T. Qian, X.-X. Wu, M.-W. Qiu, S. C. Wang, J. P. Hu, Y.-J. Sun and H. Ding. Enhanced superconductivity accompanying a Lifshitz transition in electron-doped FeSe monolayer. *Nat. Commun.* **8,** 14988 (2017).

146. A. A. Avetisyan, B. Partoens and F. M. Peeters. Electric-field control of the band gap and Fermi energy in graphene multilayers by top and back gates. *Phys. Rev. B* **80,** 195401 (2009).

147. A. Laturia, M. L. van de Put and W. G. Vandenberghe. Dielectric properties of hexagonal boron nitride and transition metal dichalcogenides. From monolayer to bulk. *NPJ 2D Mater. Appl.* **2,** 4106 (2018).

148. W. Bao, J. Velasco, F. Zhang, L. Jing, B. Standley, D. Smirnov, M. Bockrath, A. H. MacDonald and C. N. Lau. Evidence for a spontaneous gapped state in ultraclean bilayer graphene. *Proc. Natl. Acad. Sci. USA* **109,** 10802–10805 (2012).

149. A. S. Mayorov, D. C. Elias, M. Mucha-Kruczynski, R. V. Gorbachev, T. Tudorovskiy, A. Zhukov, S. V. Morozov, M. I. Katsnelson, V. I. Fal'ko, A. K. Geim and K. S. Novoselov. Interaction-driven spectrum reconstruction in bilayer graphene. *Science* **333,** 860–863 (2011).

150. F. Zhang and A. H. MacDonald. Distinguishing spontaneous quantum Hall states in bilayer graphene. *Phys. Rev. Lett.* **108,** 186804 (2012).

151. R. Nandkishore and L. Levitov. Dynamical screening and excitonic instability in bilayer graphene. *Phys. Rev. Lett.* **104,** 156803 (2010).

152. R. Nandkishore and L. Levitov. Flavor Symmetry and Competing Orders in Bilayer Graphene. *arXiv:1002.1966* (2010).

153. M. Kharitonov. Canted antiferromagnetic phase of the ν=0 quantum Hall state in bilayer graphene. *Phys. Rev. Lett.* **109,** 46803 (2012).

154. M. Kharitonov. Antiferromagnetic state in bilayer graphene. *Phys. Rev. B* **86,** 195435 (2012).

155. J. Li, H. Fu, Z. Yin, K. Watanabe, T. Taniguchi and J. Zhu. Metallic Phase and Temperature Dependence of the ν=0 Quantum Hall State in Bilayer Graphene. *Phys. Rev. Lett.* **122,** 97701 (2019).

156. F. Freitag, J. Trbovic, M. Weiss and C. Schönenberger. Spontaneously gapped ground state in suspended bilayer graphene. *Phys. Rev. Lett.* **108,** 76602 (2012).

157. F. Freitag, M. Weiss, R. Maurand, J. Trbovic and C. Schönenberger. Homogeneity of bilayer graphene. *Solid State Commun.* **152,** 2053–2057 (2012).

158. D. S. Lee, V. Skákalová, R. T. Weitz, K. von Klitzing and J. H. Smet. Transconductance fluctuations as a probe for interaction-induced quantum Hall states in graphene. *Phys. Rev. Lett.* **109,** 56602 (2012).

159. H. Polshyn, J. Zhu, M. A. Kumar, Y. Zhang, F. Yang, C. L. Tschirhart, M. Serlin, K. Watanabe, T. Taniguchi, A. H. MacDonald and A. F. Young. Electrical switching of magnetic order in an orbital Chern insulator. *Nature* **588,** 66–70 (2020).

160. M. Serlin, C. L. Tschirhart, H. Polshyn, Y. Zhang, J. Zhu, K. Watanabe, T. Taniguchi, L. Balents and A. F. Young. Intrinsic quantized anomalous Hall effect in a moiré heterostructure. *Science* **367,** 900–903 (2020).

161. A. L. Sharpe, E. J. Fox, A. W. Barnard, J. Finney, K. Watanabe, T. Taniguchi, M. A. Kastner and D. Goldhaber-Gordon. Emergent ferromagnetism near three-quarters filling in twisted bilayer graphene. *Science* **365,** 605–608 (2019).

162. B. Lian, X.-Q. Sun, A. Vaezi, X.-L. Qi and S.-C. Zhang. Topological quantum computation based on chiral Majorana fermions. *Proc. Natl. Acad. Sci. USA* **115,** 10938–10942 (2018).

163. Michael M. Lee, Joël Teuscher, Tsutomu Miyasaka, Takurou N. Murakami and Henry J. Snaith. Efficient Hybrid Solar Cells Based on Meso-Superstructured Organometal Halide Perovskites. *Science* **338,** 643–647 (2012).

164. C. Xie, C.-K. Liu, H.-L. Loi and F. Yan. Perovskite-Based Phototransistors and Hybrid Photodetectors. *Adv. Funct. Mater.* **9,** 1903907 (2019).

165. B. Yang, F. Zhang, J. Chen, S. Yang, X. Xia, T. Pullerits, W. Deng and K. Han. Ultrasensitive and Fast All-Inorganic Perovskite-Based Photodetector via Fast Carrier Diffusion. *Adv. Mater.* **29,** 1703758 (2017).

166. F. Li, C. Ma, H. Wang, W. Hu, W. Yu, A. D. Sheikh and T. Wu. Ambipolar solution-processed hybrid perovskite phototransistors. *Nat. Commun.* **6,** 8238 (2015).

167. X. Y. Chin, D. Cortecchia, J. Yin, A. Bruno and C. Soci. Lead iodide perovskite light-emitting field-effect transistor. *Nat. Commun.* **6,** 7383 (2015).

168. S. P. Senanayak, B. Yang, T. H. Thomas, N. Giesbrecht, W. Huang, E. Gann, B. Nair, K. Goedel, S. Guha, X. Moya, C. R. McNeill, P. Docampo, A. Sadhanala, R. H. Friend and H. Sirringhaus. Understanding charge transport in lead iodide perovskite thin-film field-effect transistors. *Sci. Adv.* **3,** 1601935 (2017).

169. Y. Zou, F. Li, C. Zhao, J. Xing, Z. Yu, W. Yu and C. Guo. Anomalous Ambipolar Phototransistors Based on All-Inorganic CsPbBr 3 Perovskite at Room Temperature. *Adv. Opt. Mater.* **7,** 1900676 (2019).

170. Kagan, Mitzi and Dimitrakopoulos. Organic-inorganic hybrid materials as semiconducting channels in thin-film field-effect transistors. *Science* **286,** 945–947 (1999).

171. D. Li, G. Wang, H.-C. Cheng, C.-Y. Chen, H. Wu, Y. Liu, Y. Huang and X. Duan. Size-dependent phase transition in methylammonium lead iodide perovskite microplate crystals. *Nat. Commun.* **7,** 11330 (2016).

172. W. Yu, F. Li, L. Yu, M. R. Niazi, Y. Zou, D. Corzo, A. Basu, C. Ma, S. Dey, M. L. Tietze, U. Buttner, X. Wang, Z. Wang, M. N. Hedhili, C. Guo, T. Wu and A. Amassian. Single crystal hybrid perovskite field-effect transistors. *Nat. Commun.* **9,** 5354 (2018).

173. E. Oksenberg, E. Sanders, R. Popovitz-Biro, L. Houben and E. Joselevich. Surface-Guided CsPbBr3 Perovskite Nanowires on Flat and Faceted Sapphire with Size-Dependent Photoluminescence and Fast Photoconductive Response. *Nano Lett.* **18,** 424–433 (2018).

174. C. Huo, X. Liu, X. Song, Z. Wang and H. Zeng. Field-Effect Transistors Based on van-der-Waals-Grown and Dry-Transferred All-Inorganic Perovskite Ultrathin Platelets. *J. Phys. Chem. Lett.* **8,** 4785–4792 (2017).

175. X. Hu, H. Zhou, Z. Jiang, X. Wang, S. Yuan, J. Lan, Y. Fu, X. Zhang, W. Zheng, X. Wang, X. Zhu, L. Liao, G. Xu, S. Jin and A. Pan. Direct Vapor Growth of Perovskite CsPbBr3 Nanoplate Electroluminescence Devices. *ACS Nano* **11,** 9869–9876 (2017).

176. J. Kim, S.-H. Lee, J. H. Lee and K.-H. Hong. The Role of Intrinsic Defects in Methylammonium Lead Iodide Perovskite. *J. Phys. Chem. Lett.* **5,** 1312–1317 (2014).

177. Q. Wang, Y. Shao, H. Xie, L. Lyu, X. Liu, Y. Gao and J. Huang. Qualifying composition dependent p and n self-doping in CH3NH3PbI3. *Appl. Phys. Lett.* **105,** 163508 (2014).

178. W. L. Leong, Z.-E. Ooi, D. Sabba, C. Yi, S. M. Zakeeruddin, M. Graetzel, J. M. Gordon, E. A. Katz and N. Mathews. Identifying Fundamental Limitations in Halide Perovskite Solar Cells. *Adv. Mater.* **28,** 2439–2445 (2016).

179. T. Zhang, C. Hu and S. Yang. Ion Migration. A “Double-Edged Sword” for Halide-Perovskite-Based Electronic Devices. *Small Methods* **4,** 1900552 (2019).

180. R. T. Weitz, U. Zschieschang, F. Effenberger, H. Klauk, M. Burghard and K. Kern. High-performance carbon nanotube field effect transistors with a thin gate dielectric based on a self-assembled monolayer. *Nano Lett.* **7,** 22–27 (2007).

181. Z. Xiao, Y. Yuan, Y. Shao, Q. Wang, Q. Dong, C. Bi, P. Sharma, A. Gruverman and J. Huang. Giant switchable photovoltaic effect in organometal trihalide perovskite devices. *Nat. Mater.* **14,** 193–198 (2015).

182. B.-B. Zhang, F. Wang, H. Zhang, B. Xiao, Q. Sun, J. Guo, A. B. Hafsia, A. Shao, Y. Xu and J. Zhou. Defect proliferation in CsPbBr3 crystal induced by ion migration. *Appl. Phys. Lett.* **116,** 63505 (2020).

183. Cheng Chen, Qiuyun Fu, Pengju Guo, Hualin Chen, Mei Wang, Wei Luo and Zhiping Zheng. Ionic transport characteristics of large-size CsPbBr3 single crystals. *Mater. Res. Express* **6,** 115808 (2019).

184. C. Eames, J. M. Frost, P. R. F. Barnes, B. C. O'Regan, A. Walsh and M. S. Islam. Ionic transport in hybrid lead iodide perovskite solar cells. *Nat. Commun.* **6,** 7497 (2015).

185. Y. Meng, C. Lan, F. Li, S. Yip, R. Wei, X. Kang, X. Bu, R. Dong, H. Zhang and J. C. Ho. Direct Vapor-Liquid-Solid Synthesis of All-Inorganic Perovskite Nanowires for High-Performance Electronics and Optoelectronics. *ACS Nano* **13,** 6060–6070 (2019).

186. X. Hu, X. Wang, P. Fan, Y. Li, X. Zhang, Q. Liu, W. Zheng, G. Xu, X. Wang, X. Zhu and A. Pan. Visualizing Carrier Transport in Metal Halide Perovskite Nanoplates via Electric Field Modulated Photoluminescence Imaging. *Nano Lett.* **18,** 3024–3031 (2018).

187. L. Janker, Y. Tong, L. Polavarapu, J. Feldmann, A. S. Urban and H. J. Krenner. Real-Time Electron and Hole Transport Dynamics in Halide Perovskite Nanowires. *Nano Lett.* **19,** 8701–8707 (2019).

188. H. Zhang, X. Liu, J. Dong, H. Yu, C. Zhou, B. Zhang, Y. Xu and W. Jie. Centimeter-Sized Inorganic Lead Halide Perovskite CsPbBr3 Crystals Grown by an Improved Solution Method. *Cryst. Growth Des.* **17,** 6426–6431 (2017).

189. G. R. Yettapu, D. Talukdar, S. Sarkar, A. Swarnkar, A. Nag, P. Ghosh and P. Mandal. Terahertz Conductivity within Colloidal CsPbBr3 Perovskite Nanocrystals. Remarkably High Carrier Mobilities and Large Diffusion Lengths. *Nano Lett.* **16,** 4838–4848 (2016).

190. A. Jha, H.-G. Duan, V. Tiwari, P. K. Nayak, H. J. Snaith, M. Thorwart and R. J. D. Miller. Direct Observation of Ultrafast Exciton Dissociation in Lead Iodide Perovskite by 2D Electronic Spectroscopy. *ACS Photonics* **5,** 852–860 (2017).

191. Y. Chen, H. T. Yi, X. Wu, R. Haroldson, Y. N. Gartstein, Y. I. Rodionov, K. S. Tikhonov, A. Zakhidov, X.-Y. Zhu and V. Podzorov. Extended carrier lifetimes and diffusion in hybrid perovskites revealed by Hall effect and photoconductivity measurements. *Nat. Commun.* **7,** 12253 (2016).

192. M. Buscema, J. O. Island, D. J. Groenendijk, S. I. Blanter, G. A. Steele, H. S. J. van der Zant and A. Castellanos-Gomez. Photocurrent generation with two-dimensional van der Waals semiconductors. *Chem. Soc. Rev.* **44,** 3691–3718 (2015).

193. J. Feng, X. Yan, Y. Liu, H. Gao, Y. Wu, B. Su and L. Jiang. Crystallographically Aligned Perovskite Structures for High-Performance Polarization-Sensitive Photodetectors. *Adv. Mater.* **29,** 1605993 (2017).

194. M. Waldrip, O. D. Jurchescu, D. J. Gundlach and E. G. Bittle. Contact Resistance in Organic Field-Effect Transistors. Conquering the Barrier. *Adv. Funct. Mater.* **39,** 1904576 (2019).

195. Y. Xu, H. Sun, W. Li, Y.-F. Lin, F. Balestra, G. Ghibaudo and Y.-Y. Noh. Exploring the Charge Transport in Conjugated Polymers. *Adv. Mater.* **29,** 1702729 (2017).

196. L. Bürgi, T. J. Richards, R. H. Friend and H. Sirringhaus. Close look at charge carrier injection in polymer field-effect transistors. *J. Appl. Phys.* **94,** 6129–6137 (2003).

197. V. K. Ravi, G. B. Markad and A. Nag. Band Edge Energies and Excitonic Transition Probabilities of Colloidal CsPbX 3 (X = Cl, Br, I) Perovskite Nanocrystals. *ACS Energy Lett.* **1,** 665–671 (2016).

198. M. Kulbak, S. Gupta, N. Kedem, I. Levine, T. Bendikov, G. Hodes and D. Cahen. Cesium Enhances Long-Term Stability of Lead Bromide Perovskite-Based Solar Cells. *J. Phys. Chem. Lett.* **7,** 167–172 (2016).

199. C. C. Stoumpos, C. D. Malliakas, J. A. Peters, Z. Liu, M. Sebastian, J. Im, T. C. Chasapis, A. C. Wibowo, D. Y. Chung, A. J. Freeman, B. W. Wessels and M. G. Kanatzidis. Crystal Growth of the Perovskite Semiconductor CsPbBr 3. A New Material for High-Energy Radiation Detection. *Cryst. Growth Des.* **13,** 2722–2727 (2013).

200. S. Hirotsu, J. Harada, M. Iizumi and K. Gesi. Structural Phase Transitions in CsPbBr 3. *J. Phys. Soc. Jpn.* **37,** 1393–1398 (1974).

201. V. Podzorov, E. Menard, A. Borissov, V. Kiryukhin, J. A. Rogers and M. E. Gershenson. Intrinsic charge transport on the surface of organic semiconductors. *Phys. Rev. Lett.* **93,** 86602 (2004).

202. D. V. Amasev, A. R. Tameev and A. G. Kazanskii. Features of the Temperature Dependences of the Photoconductivity of Organometallic CH3NH3PbI3 Perovskite Films. *Semiconductors* **53,** 1597–1602 (2019).

203. A. Pisoni, J. Jacimovic, B. Náfrádi, P. Szirmai, M. Spina, R. Gaál, K. Holczer, E. Tutis, L. Forró and E. Horváth. Metallicity and conductivity crossover in white light illuminated CH3NH3PbI3 perovskite. *arXiv:1604.05637* (2016).

204. M. V. Khenkin, D. V. Amasev, S. A. Kozyukhin, A. V. Sadovnikov, E. A. Katz and A. G. Kazanskii. Temperature and spectral dependence of CH 3 NH 3 PbI 3 films photoconductivity. *Appl. Phys. Lett.* **110,** 222107 (2017).

205. B. T. Diroll, H. Zhou and R. D. Schaller. Low-Temperature Absorption, Photoluminescence, and Lifetime of CsPbX 3 (X = Cl, Br, I) Nanocrystals. *Adv. Funct. Mater.* **28,** 1800945 (2018).

206. Q. Zhang, R. Su, X. Liu, J. Xing, T. C. Sum and Q. Xiong. High-Quality Whispering-Gallery-Mode Lasing from Cesium Lead Halide Perovskite Nanoplatelets. *Adv. Funct. Mater.* **26,** 6238–6245 (2016).

References

Abbreviations

Term	*Description*
2D	Two dimensions, two-dimensional
ABA	Bernal (ABA) stacking order
ABC	Rhombohedral (ABC) stacking order
AFM	Atomic force microscopy
ALL	“All” state
BOE	Buffered oxide etch
b-TLG	Bernal-stacked trilayer graphene
CAF	Canted antiferromagnet
DOS	Density of states
FET	Field-effect transistor
HAADF-STEM	High-angle annular dark-field scanning transmission electron microscopy
hBN	Hexagonal boron nitride
HF	Hydrofluoric acid
ICP-RIE	Inductively coupled plasma reactive-ion etching
LAF	Layer antiferromagnet
NW	Nanowire
PL	Photoluminescence
PVD	Physical vapor deposition
QAH	Quantum anomalous Hall effect
QHE	Quantum Hall effect
QSH	Quantum spin Hall effect
QVH	Quantum valley Hall effect
r-TLG	Rhombohedral trilayer graphene
s-SNOM	Scattering scanning near-field optical microscopy
TEM	Transmission electron microscopy
TLG	Trilayer graphene
UV	Ultraviolet

Danksagungen

An dieser Stelle möchte ich noch all denjenigen Personen danken, die mich während der Promotion begleitet und unterstützt haben, und ohne die diese Arbeit nicht möglich gewesen wäre:
Zunächst möchte ich Thomas Weitz ausdrücklich für die Betreuung und immerwährende Unterstützung während der Promotion danken. Herzlichen Dank für deinen vertrauensvollen Umgang und die viele Zeit, die du dir sowohl für Diskussionen als auch für meine Fragen und Anliegen genommen hast. Danke, dass du mir im Lauf der Promotion immer die Möglichkeit gegeben hast, eigenen Ideen und Projekte zu verfolgen, und mir stets mit neuen Anstößen und Ratschlägen weitergeholfen hast.
Mein besonderer Dank gilt auch meinen Kollegen, insbesondere Jakob Lenz, Fabian Geisenhof, Lisa Walter, Anna Seiler, Lucca Kühner, Fabio del Guidice, Lilian Schaffroth und Noelia Fernández. Ihr habt die letzten Jahre zu einer großartigen Zeit gemacht und mir durch so manchen Tiefpunkt geholfen. Ob im Labor, beim Mittagessen oder bei einem Feierabendbier, ich werde die Zeit mit euch sehr vermissen. Danke Jakob, für die unzähligen Gespräche über Gott und die Welt, ohne dich wäre vieles nicht möglich gewesen; Fabian, für die tiefschürfenden Diskussionen über Graphen in allen Farben und Formen sowie das Teilen deiner kulinarischen Expertise (bis auf das Kaiserschmarrn-Rezept natürlich); Herzlichen Dank auch an Lisa, du warst die beste Schreibtischnachbarin, die man sich nur vorstellen kann; Anna, dass du uns immer wieder zu leckeren und hart verdienten Kuchen verholfen hast. Lucca, für deine gute Laune die auch über die Institutsgrenzen ansteckt. Fabio, für deine unendliche Begeisterung für Physik und Politik, die die ersten Jahre unvergesslich gemacht hat. Lily, für deine völlig absurden aber vermutlich dennoch wahren Geschichten, und schlussendlich Noelia für die unzähligen Diskussionen die zu so mancher neuen Ideen geführt haben.
Mein besonderer Dank gilt ebenso den vielen Studenten, die meine (zumindest anteilige) Betreuung über sich haben ergehen lassen müssen, insbesondere Samuel Palmer, Rayner Schelwald, Stefan Wakolbinger, Lucas Hille und Anna Seiler. Obwohl ihr mich immer auf Trab gehalten habt, habe ich die Zusammenarbeit mit euch immer genossen und vieles wäre ohne euren Einsatz nicht möglich gewesen.
Ebenso gilt mein Dank allen gegenwärtigen und ehemaligen Mitglieder der Gruppe, die bisher noch unerwähnt geblieben sind, insbesondere Marco Dembecki, Xin Huang, Maximilian Kögl, Maurice

Larsson, Jakob Riedel, Daniel Vitroler, Jakob Braun, Michael Hirler, Philipp Maier, Jonas Biechteler, Daniela Priesack, Gilles Rodway-Gant, Stefan Seebauer, Florin Walter, Francesca Falorsi, Christian Eckel, Lukas Renn und Theresa Kammerbauer.

Diese Arbeit wäre nicht möglich gewesen ohne die tatkräftige Unterstützung vieler helfender Hände im Hintergrund. Zunächst ein herzliches Dankeschön an Bert Lorenz, der für den reibungslosen Ablauf des Laborbetriebs gesorgt hat und bei vielen weiteren Herausforderungen immer eine Lösung parat hatte. Ebenso meinen herzlichsten Dank an Martina Edenhofer, die dafür gesorgt hat, dass alles in geregelten Bahnen ablief. Ganz besonders möchte ich Stefan Manus danken, ohne dessen bereitwillige Hilfe und die vielen Stunden Diskussion über Elektrotechnik ich bis heute wohl nur Rauschen gemessen hätte. Weiterhin möchte ich Reinhold Rath und Anton Heindl für ihre tatkräftige Hilfe in vielerlei technischen Angelegenheiten sowie beim Aufbau der Labore danken. Dasselbe gilt für das Team der Werkstatt, das ich des Öfteren mit einer Vielzahl an Problemen, Fragen und Aufträgen beschäftigt gehalten habe. Als letztes möchte ich ausdrücklich Philipp „Reinraum-Gott“ Altpeter und Christian Obermayer danken, die mir bei der schier unendlichen Anzahl an Problemen und Problemchen der Nanofabrikation weitergeholfen haben und die bei technischen Defekten immer sofort zur Stelle waren.

Auch außerhalb der Universität haben verschiedenste Leute zum Gelingen dieser Arbeit beigetragen. Besonders hervorheben möchte ich Maksym Serbyn und Areg Ghazaryan sowie Fan Zhang, die die theoretischen Grundlagen zu den experimentellen Ergebnissen erarbeitet haben und von denen ich in diversen Diskussionen viel über Graphen gelernt habe. Des Weiteren möchte ich mich bei Lakshminarayana Polavarapu und Yu Tong bedanken, die uns mit der Synthese der Perovskite tatkräftig unterstützt haben.

Schlussendlich möchte ich noch meiner Familie und all meinen Freunden danken, die mich auf meinem Weg immer unterstützt haben und ohne die all das nicht möglich gewesen wäre. Mein ganz besonderer Dank geht hierbei an Christian, der mir immer den Rücken freigehalten hat und während aller Strapazen an meiner Seite war. Danke, dass ihr zu jeder Zeit für mich da wart!